Doctorate of National Interest

on

Space Science and Technology

INVESTIGATING INTERSTELLAR DUST IN THE MILKY WAY THROUGH X-RAY SCATTERING AND ABSORPTION

Beatrice Vaia

Supervisor
Prof. Paolo Esposito

Scuola Universitaria Superiore IUSS Pavia

Co-Supervisor
Prof. Andrea Tiengo

Scuola Universitaria Superiore IUSS Pavia

Dedicated to interstellar dust –
for being less scattered than my thoughts.

Abstract

Interstellar dust strongly affects astronomical observations across the entire electromagnetic spectrum. In the optical and ultraviolet bands, it produces extinction and reddening that must be corrected for both Galactic and extragalactic sources. At longer wavelengths, its thermal emission contaminates observations, particularly those related to studies of the cosmic microwave background. In X-ray astronomy, dust impacts observations by both absorbing and scattering photons.

Despite extensive studies at multiple wavelengths, several fundamental aspects of interstellar dust—its composition, size distribution, and large-scale spatial distribution within the Milky Way—remain uncertain. The aim of this thesis is to use X-ray absorption and scattering as complementary probes to investigate the nature of interstellar dust and derive accurate geometry-based distances to Galactic structures.

The first part of this work (Chapters 1 and 2) provides an overview of the interstellar medium (ISM) and of the physical principles governing X-ray absorption and scattering by dust grains. In the third chapter, we analyze the twenty-one X-ray dust-scattering rings generated by GRB 221009A, the brightest gamma-ray burst ever recorded. Using observations from *XMM-Newton* and *The Neil Gehrels Swift Observatory*, we mapped the ISM along the burst direction with higher resolution than existing optical and infrared three-dimensional dust maps—both in the plane of the sky (a few arcminutes) and along the line of sight (from $\simeq$ 1 pc for nearby dust clouds up to $\simeq$ 100 pc for distant structures). This analysis allowed us to revise previous estimates of the GRB soft X-ray fluence and to constrain the absorption within its host galaxy.

The fourth chapter focuses on the smallest X-ray rings produced by GRB 221009A, originating from the most distant interstellar dust layers. Using *Chandra* and late-time *XMM-Newton* observations, we accurately constrained the distance of the Perseus, Outer, and Outer Scutum–Centaurus arms towards the GRB direction. This analysis was further extended to the other two gamma-ray bursts where X-ray rings associated with dust beyond 5 kpc had previously been detected. Through a detailed re-analysis of *XMM-Newton* and *Chandra* archival data, we obtained the most precise geometric distance measurements to these Galactic spiral arms to date. These results provide independent constraints on the Milky Way's large-scale structure, derived without relying on kinematic models and assumptions about the Galactic rotation curve.

The final part of the thesis investigates the composition and size distribution of interstellar dust along the line of sight to the bright low-mass X-ray binary GX 13+1, using high-resolution *Chandra*/HETG spectroscopy. By simultaneously modeling

the Mg K and Si K absorption edges with different dust size distributions, we ruled out scenarios of both very diffuse and very dense ISM, favoring grain populations typical of average Galactic conditions, in this direction. Along this sightline, the dust composition is found to be dominated by amorphous olivine, with a minor crystalline fraction of about 2%.

In conclusion, this thesis shows that X-ray scattering and absorption provide powerful tools to constrain both the physical properties of interstellar dust and the large-scale structure of the Milky Way, offering a perspective complementary to that obtained from radio, optical, and infrared observations.

List of publications

- Tiengo, A., Pintore, F., **Vaia, B.**, Filippi, S., Sacchi, A., Esposito P., Rigoselli, M., Mereghetti, S., Salvaterra, R., Šiljeg, B., Bracco, A., Bošnjak, Z., Jelić, V., and Campana, S., "The Power of the Rings: The GRB 221009A Soft X-Ray Emission from Its Dust-scattering Halo", 2023, ApJ, 946, L30.

- **Vaia, B.**, Ursini, F., Matt, G., Ballantyne, D.R., Bianchi, S., De Rosa, A., Middei, R., Petrucci, P.O., Piconcelli, E., Tortosa, A., "The origin of the soft excess in the luminous quasar HE 1029-1401", 2024, A&A, 688, A189.

- **Vaia, B.**, Bošnjak, Z., Bracco, A., Campana, S., Esposito, P., Jelić, V., Sacchi, A., and Tiengo, A., "Probing the interstellar medium toward GRB 221009A through X-ray dust scattering", 2025, A&A, 696, A9.

- **Vaia, B.**, Fornasiero, I., Tiengo, A., Bracco, A., Jelić, V., Bošnjak, Z., Pintore, F., Esposito, P., "Accurate distances of the Galactic spiral arms from dust-scattered X-ray emission of gamma-ray bursts", submitted to A&A.

- **Vaia, B.**, Zeegers, S., Abril-Cabezas, I., Costantini, E., "Investigating interstellar dust along the line of sight of GX 13+1 using different dust size distributions", submitted to A&A.

Contents

Chapter 1

The Interstellar Medium of the Milky Way

1.1 Gas in the ISM

The interstellar medium (ISM) refers to the matter occupying the space between stellar systems within a galaxy. In the Milky Way, it accounts for roughly 10% of the galaxy's visible mass. Its composition is dominated by hydrogen ($\sim$ 70%), followed by helium ($\sim$ 28%), and all other elements collectively contribute only about 2%. The ISM is conventionally described in three primary phases, distinguished by the chemical state of hydrogen: ionized (H II), neutral (H I), and molecular (H_2).

Neutral hydrogen (H I), with temperatures ranging from 100 to 5000 K, constitutes about 60% of the ISM. A colder, denser phase associated with molecular clouds accounts for roughly 17%, while regions exceeding 10^4 K are dominated by ionized hydrogen (H II).

H I is primarily observed via the 21-cm hyperfine transition line (see Sect. 1.1.1). Key surveys such as HIPASS (Barnes et al., 2001), GALFA-HI (Peek et al., 2011), GASS (McClure-Griffiths et al., 2009; Kalberla et al., 2010; Kalberla and Haud, 2015), and EBHIS (Winkel, B. et al., 2016) have been instrumental in mapping the distribution of the neutral ISM. For molecular hydrogen (H_2), which is difficult to detect directly due to its lack of a permanent dipole moment, carbon monoxide (CO) is commonly used as a tracer. CO is the second most abundant molecule in the ISM and serves as a key proxy in the identification of molecular clouds. Our understanding of the Milky Way's structure (see Sect. 4.7) is, indeed, largely shaped by CO surveys; including the CfA-Chile survey (Dame et al., 2001; Dame and Thaddeus, 2022), the FCRAO Galactic Ring and Outer Galaxy Surveys (Heyer et al., 2001; Roman-Duval et al., 2010), and SEDIGISM (Schuller et al., 2021).

1.1.1 Gas absorption

In the quantum-mechanical description of the atom, electrons occupy orbitals whose wavefunctions and energy eigenvalues are obtained from the Schrödinger equation. Each orbital is uniquely identified by the four quantum numbers: principal (n), orbital angular momentum (l), magnetic (m), and spin (s); and according to the

Aufbau principle, electrons fill the lowest available orbitals first.

Electronic transitions occur when an electron moves from one orbital state to another, involving the absorption or emission of a photon with energy:

$$\Delta E = E_f - E_i, \tag{1.1}$$

where E_i and E_f are the energies of the initial and final orbitals, respectively.

If a photon excites an electron from a bound orbital to another higher bound state, the photon energy must exactly match the difference between two discrete energy levels. This produces a narrow, well-defined absorption feature in the spectrum, known as absorption line. Such lines are characteristic signatures of bound–bound electronic transitions.

In contrast, a photon whose energy does not match any bound–bound transition will pass through the atom without interaction, unless its energy is high enough to ionize it. In that case, the photon ejects the electron completely, in a process known as a bound–free transition or photoelectric absorption.

Hydrogen in the ISM can be ionized by photons with energies above 13.6 eV, i.e., by ultraviolet or X-ray photons (Sect. 2.2). In the case of neutral hydrogen, the photoelectric cross section is zero for photon energies below the ionization threshold of 13.6 eV. At this threshold, corresponding to the binding energy of the ground-state electron (K shell, $n = 1$), the cross section suddenly increases to a finite value. This jump is called the K edge (see Fig. 1.1).

For photon energies exceeding 13.6 eV, neutral hydrogen atoms can still absorb photons. In this regime, the excess photon energy above the ionization threshold is transferred to the liberated electron as kinetic energy. As the photon energy increases further, the photoelectric absorption cross section decreases approximately as a power law with frequency:

$$\sigma \propto \nu^{-8/3}. \tag{1.2}$$

Heavier elements, e.g. oxygen, have electrons in higher energy levels, e.g., n = 2 (L shell), as well as in the K shell. The cross sections for these elements will show not only a K edge, but also L edges at the energies where the n = 2 electrons can be ejected.

In addition to electronic transitions and photoionization edges, neutral hydrogen exhibits a magnetic–dipole hyperfine transition in its ground state, produced when the proton and electron spins flip from parallel to antiparallel, releasing a photon at a 21 cm wavelength, which is, therefore, used to map the distribution of the neutral gas.

A useful quantity to describe the amount of absorbing material along the line of sight (LOS) is the hydrogen column density, N_H. It is defined as the integral of the hydrogen number density n_H along the path s:

$$N_H = \int n_H(s)\, ds. \tag{1.3}$$

This quantity, expressed in units of cm^{-2}, represents the total number of hydrogen atoms per unit area between the observer and the source. Similarly to hydrogen,

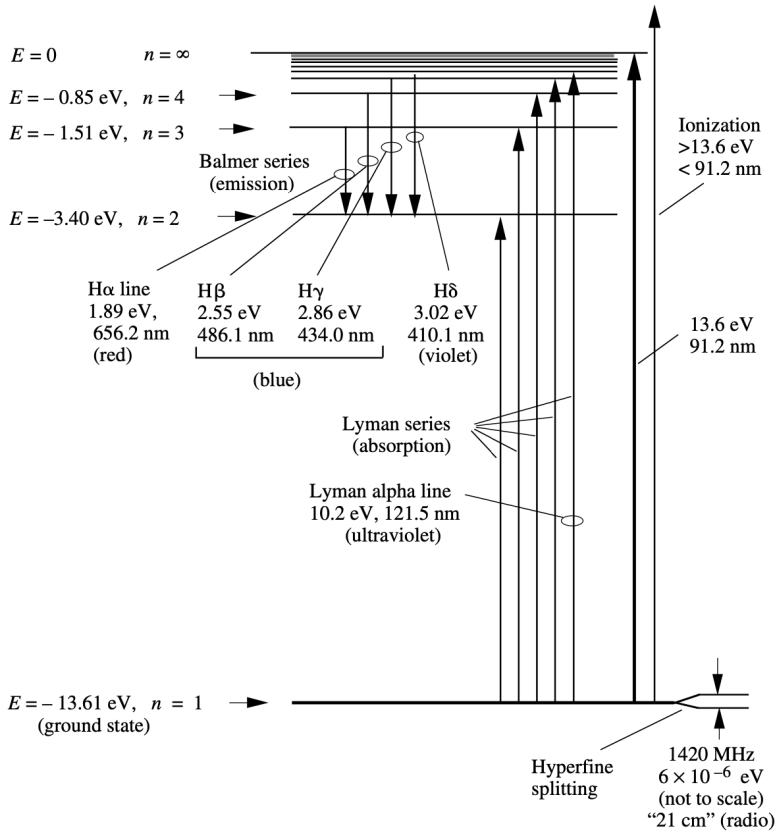

Figure 1.1: Energy levels of the hydrogen atom. Figure from Bradt (2004).

all other elements are parameterized with respect to N_H, by assuming fixed relative abundances (e.g. solar or interstellar), so that the total absorption can be described by a single global parameter.

1.1.2 Interstellar Clouds

Although most of the volume of the ISM is taken up by hot, ionized gas, most of the mass is actually found in the cooler, denser atomic and molecular regions–the clouds. The phase structure of the ISM provides a useful way to classify clouds. We can distinguish between "diffuse" clouds, where the gas at peak density is mainly atomic, and "dense" clouds, where it is primarily molecular. Numerically, they are distinguished by the fractional abundance of hydrogen in molecular form defined as:

$$f(\mathrm{H_2}) = 2n(\mathrm{H_2})/n_{\mathrm{H}}, \tag{1.4}$$

where $n_{\mathrm{H}} = n(\mathrm{H}) + 2\mathrm{n}(\mathrm{H_2})$ is the total number density of H nucleons in atoms and molecules. For a diffuse cloud $f(\mathrm{H_2})$ ranges from 0 to 0.3, in the core of a dense cloud is $\simeq 1$. In terms of n_{H} a dense cloud contains region sufficiently dense ($> 100\mathrm{cm}^{-3}$) in which all the HI is converted to $\mathrm{H_2}$.

1.2 Dust in the ISM

In the Milky Way, dust comprises only about 1% of the ISM total mass (Bohlin et al., 1978), while the majority is gas, found in both atomic and molecular forms (see Section 1). Despite its small mass fraction, dust has a significant impact on astrophysical processes in all galaxies.

The evolution of dust is closely related to that of stars, as stars interact with dust at nearly every stage of their life cycle (Jones, 1997). During the collapse of molecular clouds and the star formation process, dust is partially destroyed and also incorporated into the forming star. As stars evolve and leave the main sequence, they enter the Asymptotic Giant Branch (AGB) phase, during which they become prominent contributors of newly formed dust. Other potential sources of interstellar dust include supernovae , young stellar objects, red supergiants, and Wolf-Rayet stars (Tielens, 2001). However, the exact contribution of each source to the total interstellar dust budget remains uncertain, and the role of core-collapse supernovae is still actively debated (Slavin et al., 2020). Once released into the interstellar medium, dust undergoes both growth and destruction processes. Growth mechanisms (nucleation, condensation, accretion, and coagulation) occur both in the diffuse ISM and in denser regions, such as diffuse clouds (Draine, 2009). In contrast, destruction processes - including sputtering by gas particles, shattering, and high energy grain-grain collisions - typically occur in low density regions, driven by supernova shocks and stellar winds (Jones and Nuth, 2011).

Dust has a strong impact on many astronomical observations. First, it causes the extinction of radiation, mainly in the optical and UV wavebands, which, for extragalactic objects, requires a correction accounting for dust both in our Galaxy and in the host galaxy (see Section 1.2.1). Second, the thermal emission of interstellar

dust (see Section 1.2.2) contaminates astronomical observations at long wavelengths, significantly affecting, in particular, the study of the Cosmic Microwave Background (CMB). In X-ray astronomy, dust impacts observations by absorbing and scattering X-ray photons (see Sections 2.2 and 2.1).

1.2.1 Interstellar Extinction

Photometric and spectroscopic observations of stars allow us to measure their distances using the following equation:

$$V - M_V = 5 \log d' - 5, \tag{1.5}$$

where V and M_V are, respectively, the apparent and the absolute magnitudes of the star[1], and d' is the distance to the star in parsecs (pc). This relation assumes that there is no attenuation of the star's light along the LOS. However, if interstellar dust is present, it causes extinction - an effect resulting from both scattering and absorption - which dims the observed optical light of the star. Without accounting for extinction, the distance will be overestimated. To correct for this, Equation 1.5 is modified to:

$$V - M_V - A_V = 5 \log d' - 5, \tag{1.6}$$

where $A_V \geq 0$ represents the visual extinction due to interstellar dust (Johnson, 1968).

Interstellar extinction depends not only on the total column density of dust along the LOS but also on the wavelength of observation. Interstellar dust causes reddening of starlight in the optical band through a process analogous to the reddening of sunlight during sunset: since both absorption and scattering are more efficient at shorter wavelengths, blue light is attenuated more than red light, resulting in a reddened observed spectrum. In the Johnson photometric system, the interstellar reddening is quantified by the color excess:

$$E_{B-V} = (B - V) - (B - V)_0, \tag{1.7}$$

where $(B-V)$ is the observed color index and $(B-V)_0$ is the intrinsic (unreddened) color index of the star[2].

The visual extinction A_V can be related to the color excess through the total-to-selective extinction ratio (R_V):

$$A_V = R_V E_{B-V}. \tag{1.8}$$

The value of R_V is sensitive to the physical properties of interstellar dust, including its composition, grain size distribution, and structure, and thus varies with the local environment. In the Milky Way, a typical average value is $R_V \simeq 3.1$ (Johnson, 1968), which can be used as a reasonable approximation for most LOS. Similar processes of absorption and scattering also affect X-rays passing through the interstellar medium, although at much higher photon energies. These interactions will be discussed in detail in Chapter 2.

[1]These magnitudes are measured in the V (visual) band of the Johnson photometric system, which is centered at approximately 5400 Å.

[2]The B (blue) band in the Johnson photometric system is centered at approximately 4400 Å.

1.2.2 Infrared dust emission

Dust grains absorb UV and visible light and re-emit that as infrared (IR) radiation by thermal emission (van de Hulst, 1946). A steady state is achieved when a dust grain emits a power equal to the amount it absorbs, at a temperature T_d determined by its size and composition. According to models, dust grains with sizes in the range responsible for visible extinction (approximately 0.1 - 0.5 μm) reach thermal equilibrium at temperatures around 5 - 20 K (Whittet, 2022). At these temperatures, their emission spectrum peaks at wavelengths between 100 and 300 μm, corresponding to the far IR region of the electromagnetic spectrum.

Due to the Earth's atmosphere, this part of the spectrum cannot be observed from the ground, so confirmation of this emission was not possible until the early 1970s (Whittet, 2022). Over the years, with the development of infrared space missions, significant discoveries have been made regarding the nature and distribution of dust grains, as described in the next sections.

1.2.3 Elemental abundances of interstellar dust

As already mentioned in Sect. 1.2, the evolution of dust is closely related to that of stars. The Sun, being a normal, single, main-sequence star, is thought to have retained a reliable record of the elemental abundances present in the nebula from which it formed in the Galactic disk about 4.6 Gyr ago. Solar abundances are derived from a combination of laboratory analyses of pristine meteorites and spectroscopic measurements of the solar atmosphere. These studies indicate that the dust present in the ISM at the time and location of the Sun's birth was composed primarily of the refractory elements C, O, Mg, Si, S, and Fe, whose abundances are shown in the right panel of Fig. 1.4.

Of course, galaxies progressively enrich in heavy elements through successive generations of stars. Since the Sun formed when the Milky Way was about two thirds of its current age, differences are expected between its composition and that of much older, metal-poor, or much younger, metal-rich stars. Early-type stars (O and B), formed roughly 100 Myr ago, provide a direct probe of the present-day ISM abundances; however, their measured compositions are typically subsolar, about 63% of the solar value (Savage and Sembach, 1996; Sofia and Meyer, 2001).

The spectra of F and G type stars can be compared in detail with the solar spectrum, allowing precise measurements of elemental abundances. Observations show that the Sun is relatively metal-rich, ranking in the upper quarter of nearby G type stars (Adams, 2010), while the youngest F and G type stars (about 2 Gyr younger) have abundances very similar to solar values (Hensley and Draine, 2021). These results indicate that the abundances of the Sun can be used as a reasonable proxy for the composition of the local ISM.

1.2.4 Grain compositions

Graphite and silicates are the main constituents of most grain models. An important constraint on the composition of dust is given by the abundance of elements

(Sect. 1.2.3). We assume that the abundance is similar to that of the solar environment. However, not all elements are present in the gas phase of the ISM. Several of the most abundant elements are significantly underrepresented (or "depleted") in the gas phase and are therefore inferred to be locked into dust particles. Analysis of elemental abundances together with depletion patterns implies that the main constituents of interstellar dust are C, O, Mg, Si, Fe, and S (Draine, 2011).

Given these elemental constraints, plausible dust materials can be narrowed down to:

- Silicates, with the composition of pyroxene $Mg_xFe_{1-x}SiO_3$ or olivine $Mg_{2x}Fe_{2-2x}SiO_4$, and x between 0 and 1
- Oxides of silicon, magnesium, and iron (e.g. SiO_2, MgO, Fe_3O_4)
- Carbon solids (graphite, amorphous carbon, and diamond)
- Hydrocarbons (e.g., polycyclic aromatic hydrocarbons)
- Metallic iron
- Carbides, particularly silicon carbide (SiC)

In addition to depletion studies, the composition of interstellar dust can be constrained through more direct approaches, such as infrared observations (e.g. Tielens 2008; Gibb et al. 2004) and laboratory analysis of presolar interstellar dust grains extracted from meteorites or interplanetary dust particles. Notably, some meteorites contain grains that predate the Solar System. The abundances of such presolar grains vary among meteorites; however, studies indicate that the dominant carbonaceous phase by mass is carried by extremely small ($\sim 20\,$Å) nanodiamonds (Huss and Draine, 2007).

Silicates are detected in the ISM even in infrared spectra by two characteristic features: 10 μm (stretching of the Si-O bond) and 20 μm (bending of the O-Si-O structure) features (e.g. Knacke and Thomson 1973). Studies of these infrared features of silicates indicate a preference for Mg-rich compositions with stoichiometries between those of olivine and pyroxene (Kemper et al., 2004; Min et al., 2007; Fogerty et al., 2016). Another observed spectral feature is a broad absorption feature at 3.4 μm, which is almost certainly due to the C-H stretching mode in hydrocarbons (Draine, 2011).

Furthermore, infrared observations suggest that less than 2% of interstellar dust in the Galaxy exists in crystalline form (Kemper et al., 2004, 2005; Do-Duy et al., 2020). On the other hand, the Stardust Interstellar Dust Collector (Westphal et al., 2014) showed a large fraction of crystalline material, probably preserved within larger particles.

1.2.5 Size distributions

Interstellar dust is primarily characterized by the composition, shape, and size distribution of its particles. Over time, models of interstellar dust have evolved in

response to increasingly detailed observational data. In 1977, the model proposed by Mathis, Rumpl, and Nordsieck (Mathis et al. 1977, hereafter MRN) successfully reproduced the average interstellar extinction curve (see Sect. 1.2.1 and Fig. 1.3). The MRN model features bare, spherical silicate and graphite grains, with particle radii (a) ranging from 0.005 to 0.25 μm. The size distribution follows a simple power-law of the form:

$$n(a)\,da = A\,a^{-3.5}\,da, \tag{1.9}$$

where $n(a)$ is the number of grains per unit of size and A is a composition-dependent normalization constant.

However, observations from the *Infrared Astronomical Satellite* (IRAS) all-sky survey revealed limitations in the MRN model, particularly an unexpected excess of 12 μm and 25 μm emission from the diffuse ISM, indicating that the MRN distribution alone could not fully account for the observed dust emission. This discrepancy led to the inclusion of polycyclic aromatic hydrocarbon (PAH) molecules as an additional dust component, originally proposed by Allamandola et al. (1985). Observations from the *Cosmic Background Explorer* (COBE) further supported the presence of small carbonaceous grains within interstellar dust, which were subsequently incorporated into models such as those by Weingartner and Draine (2001) and Zubko et al. (2004), and later refined in more recent works such as Hirashita and Murga (2020). These three dust size distribution models, together with the previously discussed MRN, are adopted in the research work reported in this thesis and are therefore examined in more detail in the following.

The Weingartener & Draine Model

The Weingartner & Draine model (Weingartner and Draine, 2001) introduces two key modifications to the basic MRN model. First, as discussed in the previous section, it incorporates very small carbonaceous grains that were absent from the original MRN distribution. In addition, it provides grain size distributions tailored to reproduce the observed extinction curves for various values of R_V. Unlike the simple power-law used by MRN, the functional forms adopted in this model are more complex, allowing for a smooth cutoff and variations in slope. For carbonaceous grains, the model uses the following:

$$\frac{1}{\mathrm{n_H}}\frac{dn_{\mathrm{gr}}}{da} = D(a;b_c)+\frac{C_g}{a}\left(\frac{a}{a_{t,g}}\right)^{\alpha_g} F(a;\beta_g,a_{t,g})\times\begin{cases} 1, & 3.5\,\text{Å} < a < a_{t,g} \\ \exp\left\{-\left[\frac{a-a_{t,g}}{a_{c,g}}\right]^3\right\}, & a > a_{t,g} \end{cases} \tag{1.10}$$

where $D(a;b_c)$ represents the size distribution of PAH grains, modeled as the sum of two log-normal distributions, as described by Li and Draine (2001), and where b_{C} denotes the total carbon abundance per hydrogen nucleus.

And, for silicate dust:

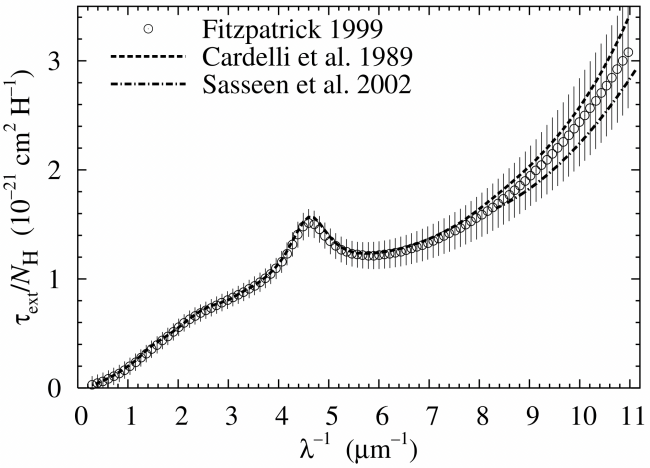

Figure 1.2: Mean extinction curve of the interstellar medium with $R_V = 3.1$. Figure from Zubko et al. (2004).

$$\frac{1}{\mathrm{n_H}}\frac{dn_{\mathrm{gr}}}{da} = \frac{C_s}{a}\left(\frac{a}{a_{t,s}}\right)^{\alpha_s} F(a;\beta_s,a_{t,s}) \times \begin{cases} 1. & 3.5\,\text{Å} < a < a_{t,s} \\ \exp\left\{-\left[\frac{a-a_{t,s}}{a_{c,s}}\right]^3\right\}. & a > a_{t,s} \end{cases} \tag{1.11}$$

In both cases, the function $F(a;\beta,a_t)$ provides the curvature:

$$F(a;\beta,a_t) \equiv \begin{cases} 1 + \beta a/a_t. & \beta \geq 0 \\ (1 - \beta a/a_t)^{-1}. & \beta < 0 \end{cases} \tag{1.12}$$

Using these mathematical expressions and a given set of parameters (R_V, b_c), Li and Draine (2001) aim to achieve the best fit to the observed extinction curve by varying the model parameters. The resulting fit for $R_V = 3.1$ and different values of b_c is shown in Fig. 1.2. The preferred value is $b_c = 6 \times 10^{-5}$.

The Zubko et al. model

In Zubko et al. (2004), the authors investigated a range of dust models designed to simultaneously reproduce not only the average interstellar extinction curve (Figure 1.2), but also the thermal infrared emission (left panel of Figure 1.4) and interstellar abundance constraints (right panel of Figure 1.4). These observational constraints are addressed through variations in dust composition. The dust constituents considered include polycyclic aromatic hydrocarbons (PAHs), graphite, and several forms of amorphous carbon - specifically ACAR (amorphous carbon with a significant aromatic content), ACH2 (hydrogenated amorphous carbon), and BE (Bias-Enhanced amorphous carbon). In addition, silicates with the composition $MgFeSiO_4$ and composite particles made of silicates, organic refractory material ($C_{25}H_{25}O_5N$), water ice, and voids are also used.

Using combinations of these components, the authors constructed five different dust models. The first model replicates the structure proposed by Li and Draine

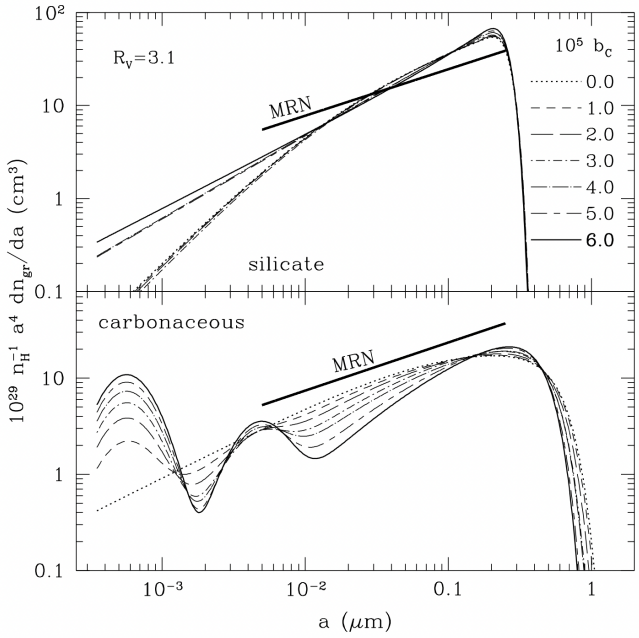

Figure 1.3: Grain size distribution derived from Weingartner and Draine (2001) for different values of b_C and $R_V = 3.1$. According to the authors, the favored distribution corresponds to $b_C = 6 \times 10^{-5}$.

(2001), consisting of PAHs, bare[3] graphite, and bare silicates. The second model extends the first by including composite particles. The third and fourth models are analogous to the first and second, respectively, but replace graphite with amorphous carbon. The fifth model contains no carbonaceous material other than PAHs, and combines them with bare silicates and composite particles.

In Zubko et al. (2004), and consequently throughout this thesis, models containing only PAHs and bare grains are designated as BARE, while those that also include composite particles are labeled COMP. The type of carbon component further modifies these labels: models using graphite are tagged with -GR, those with amorphous carbon with -AC, and those in which PAHs are the only carbon source with -NC. Accordingly, the five models are named BARE-GR, COMP-GR, BARE-AC, COMP-AC, and COMP-NC. Each of these is tested against three different abundance sets: solar, B stars, and F and G stars, denoted, respectively, as -S, -B, and -FG.

Given these dust compositions, the task of simultaneously fitting the three key observational constraints (extinction, infrared emission, and elemental abundances) constitutes an ill-posed inversion problem, in which the size distributions are unknown. This challenge is addressed numerically using a regularization technique, which yields a stable solution for the size distribution. The resulting numerical solution is then analytically approximated by a function $f(a)$ (in $\mu\mathrm{m}^{-1}H^{-1}$): $f(a) = Ag(a)$, where A is a coefficient to normalize the distribution to the number of hydrogen atoms (H^{-1}) and $g(a)$ (in $\mu\mathrm{m}^{-1}$) is approximated with the function

[3]Dust grains not coated by icy or molecular mantles.

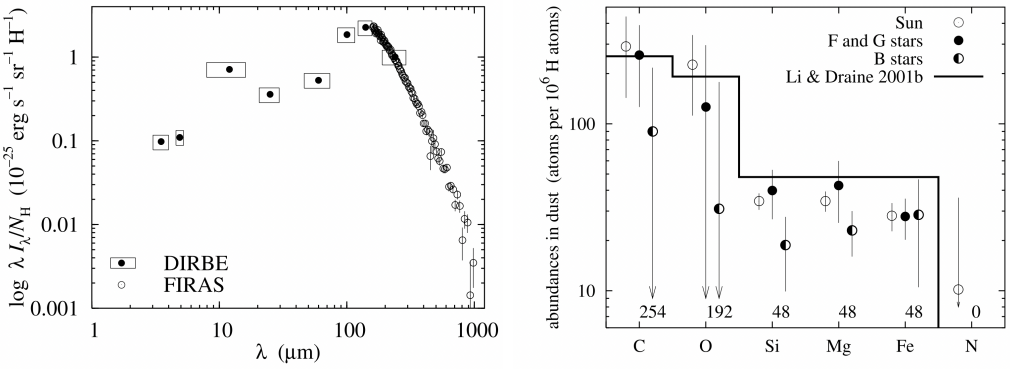

Figure 1.4: Left panel: Intensity of IR dust emission per hydrogen atom observed with DIRBE (Arendt et al., 1998) and FIRAS (Dwek et al., 1997). Right panel: Elemental abundances of dust based on those of the Sun, F and G stars, and B stars. The black solid line represents the abundances in the Li and Draine (2001) model. Figures from Zubko et al. (2004).

$\bar{g}(a)$:

$$\log \bar{g}(a) = c_0 + b_0 \log(a) - b_1 \left| \log\left(\frac{a}{a_1}\right) \right|^{m1} - b_2 \left| \log\left(\frac{a}{a_2}\right) \right|^{m2} - b_3 |a - a_3|^{m3} - b_4 |a - a_4|^{m4}. \tag{1.13}$$

This expression involves 14 parameters, which are tabulated in Tables 7 through 21 of Zubko et al. (2004), corresponding to each dust model composition. The dust distribution obtained for the BARE-GR-B and the COMP-AC-FG models are shown in Figure 1.5 as a reference.

The Hirashita and Murga Model

In contrast to the other models discussed above, Hirashita and Murga (2020) developed a comprehensive scheme that models the evolution of the grain size distribution from first principles. Their approach accounts for a wide range of processes, including stellar dust production, dust destruction by supernova shocks in the ISM, dust growth via accretion and coagulation in dense ISM regions, and dust disruption through shattering. In this framework, interstellar dust is grouped into two main types – silicate and carbonaceous grains – with the latter further divided into aromatic and non-aromatic forms. Given the dependence of dust evolution processes (such as accretion, coagulation, and shattering) on ISM density, the authors introduce a key parameter, the mass fraction of the dense gas ($\eta_{\rm dense}$), to quantify these effects.

Their results indicate that, at an age of approximately 10 Gyr and for a dense gas fraction of $\eta_{\rm dense} = 0.5$, the modeled extinction curves closely resemble those observed in the Milky Way in terms of both the far-ultraviolet slope and the strength of the carbon bump. Furthermore, by adopting a shorter star formation timescale and increasing the dense gas fraction to $\eta_{\rm dense} = 0.9$, the resulting extinction curves exhibit features comparable to those observed in the Small Magellanic Cloud and in high-redshift quasars.

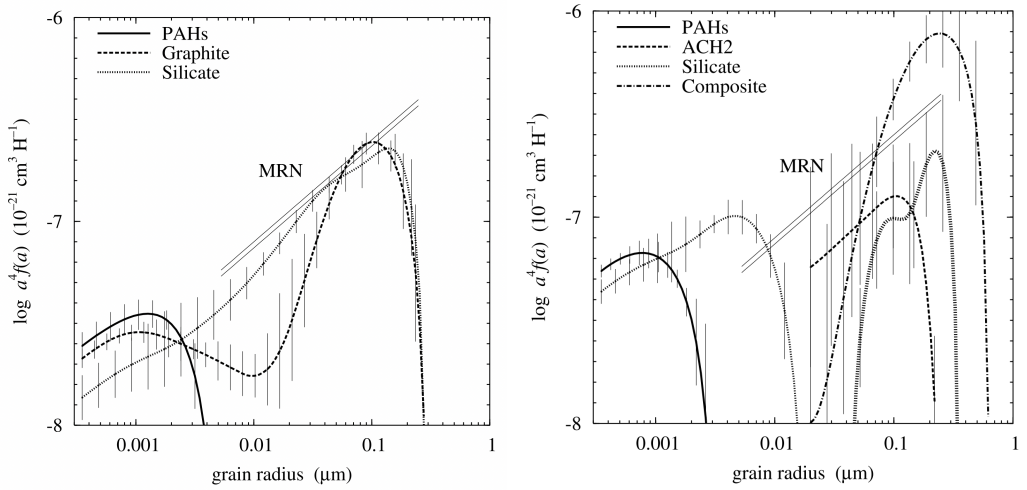

Figure 1.5: BARE-GR-B (left panel) and COMP-AC-FG (right panel) dust size distribution models from Zubko et al. (2004). For comparison the MRN size distributions are shown, for silicate (upper straight line) and for graphite (lower straight line).

Figure 1.6 illustrates the temporal evolution of the grain size distribution as obtained by Hirashita and Murga (2020), along with a comparison with the canonical MRN slope, for three values of the dense gas fraction: 0.1 (left panel), 0.5 (center panel), and 0.9 (right panel). In addition to the grain size distribution (top), the evolution of the aromatic fraction is also presented (bottom).

1.2.6 Gas to Dust ratio

To study the global relationship between gas and dust, we can compare an indicator of the gas content with an indicator of the dust content. The total amount of gas along a given LOS, expressed as hydrogen column density, $N_{\rm H}$ (Sect. 1.1.1), can be measured using different methods, such as ultraviolet absorption lines, 21 cm and CO emission, or X-ray spectral fitting. These techniques probe different phases of the interstellar medium and may yield slightly different values of $N_{\rm H}$. Instead, the color excess (Sect. 1.2.1) can be used as an indicator of the amount of dust along the LOS. The hydrogen column densities and the color excess, obtained for a number of stars in a wide distance range and different directions, can be plotted as points on an $N_{\rm H}$ vs. E_{B-V} plot. When these quantities are obtained for a large number of stars in various Galactic directions, their comparison reveals a clear positive correlation, as shown in Fig. 1.7. In that figure, the hydrogen column densities are derived from ultraviolet absorption lines, while the corresponding color excesses are obtained from optical reddening measurements of about one hundred stars and can be best represented by the following straight line:

$$N({\rm HI} + 2{\rm H_2}) / \, {\rm E}_{B-V} = 6 \times 10^{25} \, {\rm atoms \, m^{-2} mag^{-1}}, \tag{1.14}$$

where $N({\rm HI} + 2{\rm H_2})$ is the column density of hydrogen atoms and E_{B-V} is the color excess. This correlation suggests that the interstellar clouds that contain the dust

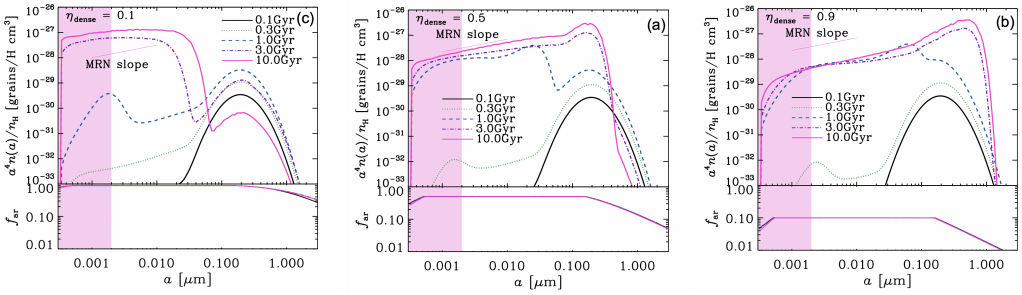

Figure 1.6: Grain size distribution (top panel) and aromatic fraction (bottom panel) as functions of grain radius (a). The solid, dotted, dashed, dot-dashed, and triple-dot-dashed lines correspond to evolutionary times of $t = 0.1$, 0.3, 1, 3, and 10 Gyr, respectively. Note that all lines overlap in the bottom panel. For reference, the thin dotted straight line in the top panel indicates the slope of the MRN grain size distribution ($n \propto a^{-3.5}$). The pink shaded region highlights the characteristic range for the grain radius of PAHs. Left panel: $\eta_{\rm dense} = 0.1$. Middle panel: $\eta_{\rm dense} = 0.5$. Right panel: $\eta_{\rm dense} = 0.9$. Figures from Hirashita and Murga (2020).

also contain hydrogen in approximately proportional amounts.

In X-ray astronomy, the $N_{\rm H}$ value can be derived from spectral analysis of relatively bright X-ray sources by assuming a photoelectric absorption model and abundances. The expected optical extinction, A_V, for the possible optical counterpart of the X-ray source can then be estimated from Eq. 1.14 and Eq. 1.8. Over the years, the relationship between optical extinction and X-ray absorption has been derived from different classes of astrophysical objects and with different telescopes. The following works can be taken as examples: Zhu et al. (2017) utilized supernova remnants, planetary nebulae, and X-ray binaries in their research. Watson (2011) conducted a study based on a substantial sample of several hundred gamma-ray bursts, while Vuong et al. (2003) focused on T-Tauri stars in six nearby star-forming regions. These studies show that, although there is a clear correlation between $N_{\rm H}$ and A_V, the normalization of this relation can vary significantly depending on the sample and environment considered. Zhu et al. (2017), for example, report values in the range $N_{\rm H}/A_V \simeq (1.0\text{–}2.9) \times 10^{21}\,{\rm H\,cm^{-2}\,mag^{-1}}$. Despite this scatter, once a specific relation is adopted, it provides a useful means to convert X-ray measurements of $N_{\rm H}$ into optical extinctions–or, conversely, to estimate the expected X-ray absorption from optical or infrared observations.

1.3 The structure of the Galaxy

One of the main goals of studying the ISM is to reconstruct the structure of the galaxy we live in. The Milky Way (illustrated in Figure 1.8) is a barred-spiral galaxy (Bland-Hawthorn and Gerhard, 2016) with a stellar disk of radius ∼15 kpc. The Sun is approximately 8 kpc from the center. Despite extensive studies throughout the last century, the exact spiral structure of the Milky Way is not yet well defined.

The Galactic structure is reconstructed on the basis of different tracers. The most widely used tracers are 6.7 GHz methanol masers, giant molecular clouds

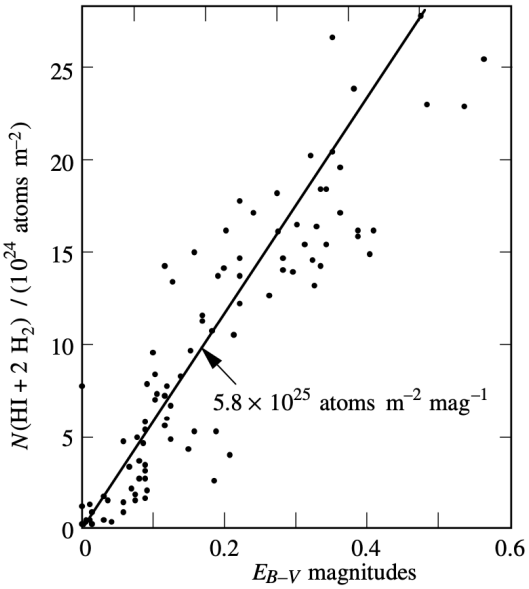

Figure 1.7: Correlation between hydrogen column density derived from ultraviolet absorption lines and color excess caused by interstellar dust along the lines of sight toward ∼100 stars. Each point corresponds to an individual star. Figure from Bradt (2004).

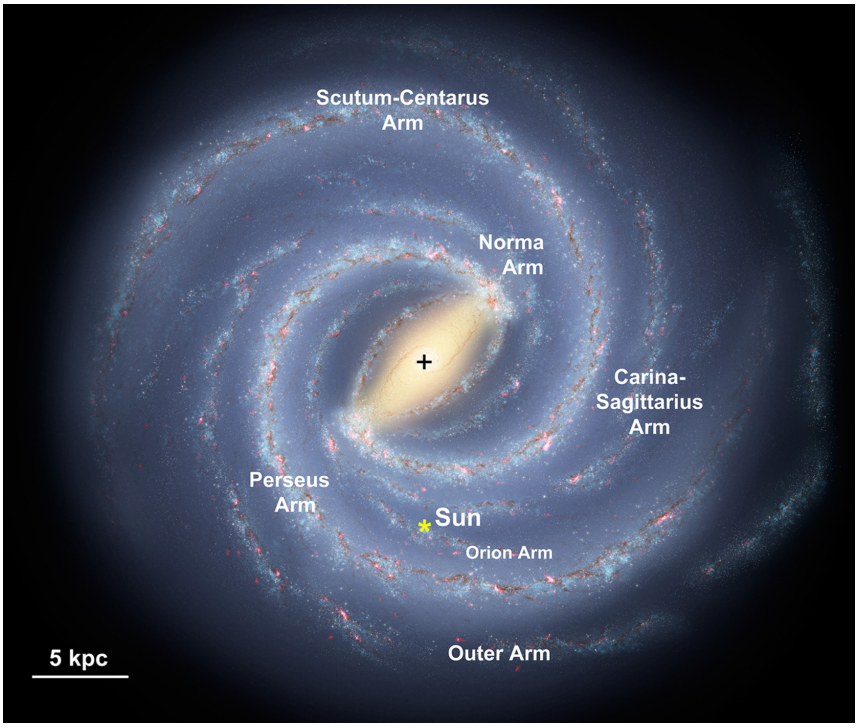

Figure 1.8: Schematic representation of the Milky Way. Spiral arm structures are labeled, with the Galactic Center marked by a black cross and the Sun indicated by a yellow asterisk. Red regions within the spiral arms denote H II regions. Figure from Whittet (2022).

(GMCs), HII regions, and clouds of neutral atomic hydrogen (HI). The distances of the regions identified in HI and HII surveys (see Sect. 1.1) are typically inferred from a Galactic rotation curve (Sect. 1.3.1). The choice and accuracy of the rotation curve are therefore crucial in assigning kinematic distances of Galactic objects.

HII regions and methanol masers are predominantly associated with star-forming regions, and GMCs serve as the birthplaces of massive stars. Because of this, their spatial distribution is expected to be consistent with that of the Galactic young stellar population. The observed masers are likely dense condensations of interstellar gas and dust located in the vicinity of a recently formed luminous star. Like lasers, masers generate coherent radiation through the process of stimulated emission. Masers, however, emit radiation at microwave frequencies, typically at well-defined spectral lines corresponding to specific molecular transitions–for instance, H_2O and methanol. The angular positions of individual maser spots are monitored over time using very long baseline interferometry (VLBI). This technique enables both trigonometric parallax measurements – providing direct geometric distances – and determinations of proper motions, and thus of tangential velocities. When combined with the radial velocities derived from the Doppler shifts of the maser spectral lines, these measurements also allow the derivation of kinematic distances, once a Galactic rotation curve is assumed.

A major breakthrough in the study of the Milky Way's structure was achieved with the launch of the ESA Gaia satellite in 2013 (Gaia Collaboration et al., 2016), which has delivered the most precise and extensive astrometric data set currently available. By repeatedly observing more than one billion stars, Gaia provides highly accurate measurements of stellar positions, parallaxes, and proper motions, enabling the construction of a detailed three-dimensional map of the Galaxy and the investigation of its kinematics and dynamics. In addition to astrometry, Gaia collects broad-band photometry and low-resolution spectroscopy, which allow the estimation of stellar parameters such as effective temperature, luminosity, and radial velocity for a large subset of stars. Based on these measurements, which are available for the full sky, Gaia is also able to provide not only precise distances but also estimates of interstellar extinction for an unprecedented number of Galactic stars, thereby offering crucial information on the distribution of dust and its impact on observed stellar properties (see, for example, Lallement et al. 2022; Green et al. 2019; Edenhofer et al. 2024).

The accuracy of Gaia parallaxes and extinction estimates decreases for faint stars and in regions of high dust density, restricting reliable measurements to the nearby Galaxy ($\sim$ 1 kpc) and highlighting the need for complementary observations. To explore more distant regions of the Galactic plane, extinction maps based on IR data can be utilized. Over the years, significant work has been done in this field. For example, Schlegel et al. (1998) used far-infrared dust emission data from the IRAS and COBE satellites to create an all-sky dust column density map. In 2006, Lombardi et al. (2006) employed 2MASS photometric data and the color excess technique to study molecular clouds, while Schlafly et al. (2010) used data from the Sloan Digital Sky Survey (SDSS). More recently, Rezaei et al. (2024) produced a 3D map of the Milky Way's plane extending up to 10 kpc using near-IR data from the SDSS Apache Point Observatory Galactic Evolution Experiment (APOGEE).

All these tracers contribute to the knowledge of the spiral structure of the Milky way. Recent studies (Hou, L. G. and Han, J. L., 2014) suggest that our Galaxy has four spiral arms, which contrasts with earlier models that indicated only two arms (Oort et al., 1958). However, uncertainties persist with respect to the exact morphology of the Milky Way. For example, only in 2011 studying CO emission, Dame and Thaddeus (2011) identified a new spiral arm beyond the Outer Arm at $\simeq$ 15 kpc from the Galactic center, at longitudes from 13° to 55°. This new arm was overlooked in existing 21 cm surveys probably because it is substantially inclined with respect to the Galactic plane.

1.3.1 Rotation curve of the Milky Way

The main parameters of Galactic rotation curves are the Galactic constants (R_0, V_0), where R_0 denotes the distance of the Sun from the Galactic center and V_0, the circular velocity of the local standard of rest (LSR) at the Sun's position. Various studies (e.g., Clemens 1985; Honma et al. 2015; Reid et al. 2019) have converged to values of $R_0 \sim 8.0$–8.3 kpc and $V_0 \sim 240$ km s^{-1}.

However, the particular position of the Sun within the Milky Way makes it challenging to measure the rotation velocity of Galactic objects. Observations are carried out from within the Galactic disk, where dust extinction, non-axisymmetric structures (such as the Galactic bar and spiral arms), and the peculiar motions of individual sources introduce substantial uncertainties. Furthermore, different tracers of Galactic rotation–such as H I and CO molecular clouds–can provide slightly different results depending on the assumptions made about their systemic velocities and distances. To derive the Galactic rotation curve, several kinematic methods are typically employed, including the tangent-point method for the inner Galaxy ($R < R_0$), and parallax and proper motion measurements of masers through Very Long Baseline Interferometry (VLBI) for sources distributed across the disk (e.g. Reid et al. 2019).

1.4 Open questions on interstellar dust

As discussed in previous sections, over the past decades our understanding of interstellar dust has grown significantly. However, The exact composition of ISM dust is still not fully established. For example, it is not clear whether olivine or pyroxene is the dominant silicate in the ISM, and the form in which iron exists within dust grains remains uncertain. Observations indicate that interstellar dust is largely amorphous, yet the processes responsible for this amorphization are still debated. Both cosmic-ray irradiation and grain growth within the ISM have been proposed as possible causes. Similarly, the characteristics of the dust size distribution are not well constrained, particularly regarding the existence and importance of very large grains.

In addition, the spatial distribution of dust and gas throughout the Galaxy remains an open question, with considerable uncertainties in the outer regions.

X-ray observations offer a promising avenue for addressing these ongoing uncertainties and shed light on the nature and behavior of interstellar dust.

Chapter 2

X-rays to study dust

Similarly to optical radiation (Sect. 1.2.1), X-rays interact with interstellar dust through both absorption and scattering. The launch of the *XMM-Newton* and *Chandra* X-ray observatories in 1999 (see Appendix A) marked the beginning of a new era in the study of interstellar dust at X-ray wavelengths. Thanks to their large effective area and their excellent angular and energy resolution, these telescopes are well-suited for detailed investigations of these phenomena. The following two sections will explore the theory behind absorption and scattering in detail.

2.1 X-ray scattering

As discussed in Sect. 1.2.1, the interaction between starlight and interstellar dust involves both absorption and scattering processes. At relatively low photon energies (from infrared to ultraviolet wavelengths), photons may be scattered elastically by atoms or molecules, being temporarily absorbed and re-emitted without a change in energy. This process, known as Rayleigh scattering, is strongly wavelength dependent with shorter wavelengths being scattered more efficiently than longer ones (see Sect. 1.2.1). At higher photon energies, exceeding the ionization threshold of the atom, the dominant process is Thomson scattering. In this case as well, the photon is absorbed and promptly re-emitted in a different direction by a free electron, with its initial energy fully preserved. However, unlike Rayleigh scattering, Thomson scattering is independent of the frequency of the incident radiation. An example of Thomson scattering can be observed when X-rays interact with atmospheric molecules in a room near an X-ray generating machine. The scattering arises mainly from the outer-shell electrons of air molecules, whose binding energies are much lower than the energy of the incident photons. In this context, even the scattering of X-rays by interstellar dust can be interpreted as Thomson scattering by quasi-free electrons within the dust grains, where the angular dependence of the scattered intensity is mainly governed by the spatial distribution and size of the grains rather than by the radiation frequency. In the hard X-ray range (> 30 keV), Compton scattering becomes the dominant interaction mechanism. This process is an inelastic scattering between the photon and an electron, in which the photon transfers part of its energy to the electron and is therefore deflected with reduced energy. However, the cross-section for the interaction of dust with X-rays strongly

decreases with energy, and therefore X-ray dust-scattering is not expected to have detectable effects at such high energies.

The idea that X-rays could be scattered by interstellar dust was first proposed by Overbeck (1965), shortly after the discovery of the first X-ray point sources beyond the Solar System (Giacconi et al., 1962). However, the first detection of a dust scattering halo was not made until more than a decade later, around the bright low-mass X-ray binary GX 339-4, using the Einstein Observatory (Rolf, 1983). The launch of the German satellite ROSAT in 1990 (Truemper, 1982) enabled the first systematic survey of X-ray scattering halos, strengthening the connection between X-ray observations and the optical properties of the ISM.

X-ray scattering by dust is constrained to very small angles, typically less than one degree, and is only in the forward direction. This is because the characteristic scattering angle scales with the photon wavelength and the grain size as $\sim \lambda/2\pi a$, effectively confining the scattered radiation to small angles and low energies. Due to the small scattering cross sections, only a small fraction (usually a few percent) of the incident X-ray flux is deflected. Consequently, the observation of a detectable scattering halo requires both a bright X-ray source and a significant column of interstellar dust along the LOS.

We can divide the X-ray scattering signals into 3 groups:

- Constant dust scattering halos, formed by persistently bright X-ray sources behind a large amount of dust. These are the easiest to observe and were first extensively studied with the Einstein Observatory, followed by subsequent X-ray missions.

- Variable dust scattering halos, formed by bright but variable X-ray sources behind a thick veil of dust.

- X-ray expanding rings (see Fig. 2.1 for a few examples). When the X-ray source undergoes a distinct flare followed by a period of quiescence and the dust is concentrated in sufficiently thin dust layers, the scattering generates discrete expanding rings (one for each dust layer) instead of a diffuse halo, since only the photons scattered at a well-determined angle are detected at a given time.

The observation of dust-scattered X-rays is a time-dependent phenomenon. Scattered photons arrive later than direct ones because of their longer travel paths, a consequence of the scattering geometry (illustrated in Fig. 2.2). This time delay plays a crucial role in the study of variable halos and, more strikingly, expanding X-ray rings. The angular size of the formed expanding ring, θ, is given by the relation:

$$\theta = \sqrt{\frac{2c\Delta t}{D_{dust}}\left(1 - \frac{D_{dust}}{D}\right)}, \tag{2.1}$$

where c is the speed of light, Δt is the time delay between direct and scattered X-rays, D is the distance to the X-ray source, and D_{dust} is the distance to the dust cloud (Miralda-Escudé, 1999).
In the case of Galactic X-ray sources, if the distance to the dust layer is known,

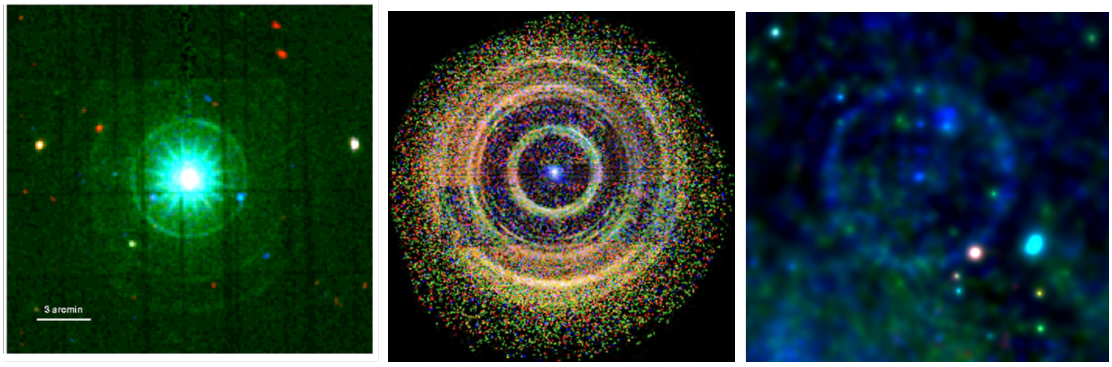

Figure 2.1: Left panel: XMM-Newton image of the three dust-scattering rings produced by the bursting activity of the Galactic magnetar 1E 1547.0-5408 (Tiengo et al., 2010). Middle panel: Combined Chandra and Swift observations of the light echo generated by the 2015 outburst of the black hole X-ray binary V404 Cygni, displaying eight rings (Heinz et al., 2016). Right panel: The giant dust scattering ring (diameter $> 1°$) around the black hole transient MAXI J1348-630 observed by SRG/eROSITA during its first X-ray all-sky survey (Lamer et al., 2021).

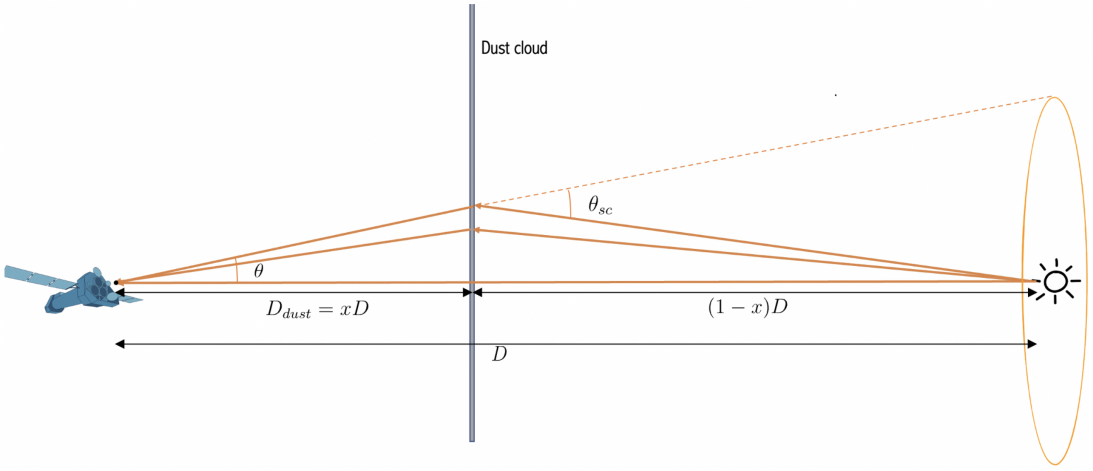

Figure 2.2: Geometry of the X-ray dust scattering phenomenon.

this method can be used to infer the distance to the source; conversely, if the source distance is known, this method can be used to infer the distance of the dust layer.

In the case of an extragalactic X-ray source (e.g. a Gamma-Ray burst) scattered by Galactic dust, the distance to the X-ray source, D, is much greater than the distance to the dust layer, D_{dust}. Under these circumstances, since D_{dust}/D is very small, the expression for the angle θ simplifies to the following:

$$\theta[\text{arcmin}] = 4.455\sqrt{\frac{\Delta\text{t[days]}}{\text{D}_{\text{dust}}[\text{kpc}]}}. \tag{2.2}$$

Thus, by analyzing the expansion of the rings over time, one can determine the distance to the intervening dust clouds.

The intensity of the scattered radiation depends not only on the property of the X-ray radiation but also on the spatial distribution of the dust along the LOS and the scattering cross section of the dust, with the latter being determined by the physical properties of the grains. By studying the temporal and spectral evolution of the expanding X-ray rings, it is therefore possible to simultaneously infer the characteristics of the intervening dust and the properties of the X-ray emission that generated them – such as its fluence and spectral shape. This relation can be expressed as:

$$I_\nu = N_{\text{H}} \frac{d\sigma_{\text{sca},\nu}}{d\Omega} \frac{F_\nu(t = t_{\text{obs}} - \Delta t)}{(1-x)^2}, \tag{2.3}$$

where N_{H} denotes the hydrogen column density responsible for the halo, $d\sigma_{\text{sca},\nu}/d\Omega$ represents the differential dust scattering cross section, $F_\nu(t)$ is the flux of the flare at time t, and $x = D_{dust}/D$ indicates the relative position of the dust layer as a fraction of the distance to the source. In the case of a short flare, the flux density of each ring is calculated through integration over θ, keeping $d\sigma_{\text{sca},\nu}/d\Omega$ constant across the ring:

$$F_{\text{ring},\,\nu} = \frac{2\pi c N_{\text{H}}}{x(1-x)D} \frac{d\sigma_{\text{sca},\nu}}{d\Omega} \mathcal{F}_\nu, \tag{2.4}$$

where $\mathcal{F}_\nu$ represents the fluence of the flare. The exact scattering cross sections can be calculated using the Mie theory, which is discussed in detail in the next section.

2.1.1 The Mie Theory

The total attenuation of an incident electromagnetic beam by a particle is quantitatively described by the extinction efficiency factor, defined as the ratio between the particle's extinction cross section (C_{ext}) and its geometric cross section, πa^2:

$$Q_{\text{ext}} = \frac{C_{\text{ext}}}{\pi a^2}. \tag{2.5}$$

The extinction efficiency can be further decomposed into the sum of the absorption and scattering efficiency factors:

$$Q_{\text{ext}} = Q_{\text{abs}} + Q_{\text{sca}}. \tag{2.6}$$

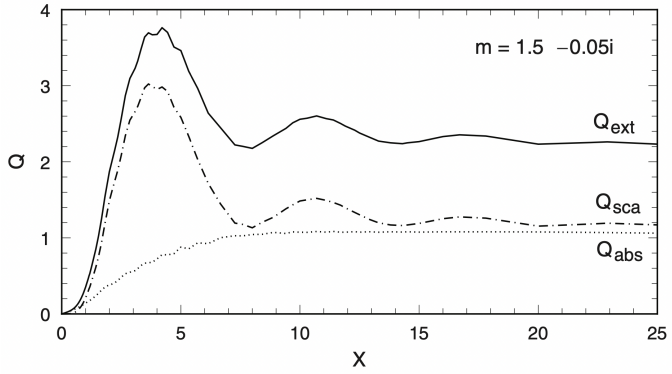

Figure 2.3: Mie theory results for spherical grains characterized by a refractive index $m = 1.5 - 0.05i$, shown as a function of the size parameter X. Figure from Whittet (2022).

Both $Q_{\rm abs}$ and $Q_{\rm sca}$ depend on two key parameters:

- a dimensionless size parameter, $X = \frac{2\pi a}{\lambda}$, which relates the radius of the particle a to the wavelength λ;
- the complex refractive index of the material, $m = n - ik$.

Therefore, to compute $Q_{\rm abs}$ and $Q_{\rm sca}$ for a given grain material, the refractive index components n and k must be determined at each wavelength λ.

This problem involves solving Maxwell's equations with the appropriate boundary conditions at the particle surface. The first analytical solution was provided by Mie (1908), and the method is now known as Mie theory. Figure 2.3 shows the results of the Mie theory for spherical grains with a constant complex refractive index.

Once $Q_{\rm sca}$ is known, the scattering cross section $C_{\rm sca}$ can be directly computed from Equation 2.5 as:

$$C_{\rm sca} = \pi a^2 Q_{\rm sca}. \tag{2.7}$$

2.1.2 Rayleigh-Gans approximation

The Rayleigh-Gans regime is applicable when the following two conditions are satisfied (Smith and Dwek, 1998):

- The reflection from the surface of the dust particle is negligible, which means $|m - 1| \ll 1$,
- The phase shift of the incident wave inside the particle is negligible, i.e. $(2\pi a/\lambda)\,|m - 1| \ll 1$.

Under these conditions, the differential scattering cross section can be analytically described (Mauche and Gorenstein, 1986) by:

$$\left(\frac{d\sigma}{d\Omega}\right)(E, a, \phi) = 2a^2 \left(\frac{2\pi a}{\lambda}\right)^4 |m - 1|^2 \left(\frac{j_1(y)}{y}\right)^2 (1 + \cos^2\phi). \tag{2.8}$$

Where $y = (4\pi a/\lambda)\sin(\phi/2)$ and j_1 is the spherical Bessel function which can be well approximated by a Gaussian factor:

$$\left(\frac{d\sigma}{d\Omega}\right)(E, a, \phi) \sim 2a^2\left(\frac{2\pi a}{\lambda}\right)^4 |m-1|^2 \, \frac{1}{9} \exp\left(-\frac{y^2}{2\sigma^2}\right)(1+\cos^2\phi), \qquad (2.9)$$

with σ which is a function of the energy and size of the dust particle. For typical grain sizes of interstellar dust, this approximation has limitations at energies below 2 keV, where the second condition is no longer satisfied and the calculated cross sections deviate from those predicted by Mie theory. Furthermore, this discrepancy becomes more pronounced for larger grain sizes. Most of the signal from the observed X-ray rings is concentrated below 2 keV so the Rayleigh-Gans approximation is not appropriate for the high quality X-ray spectra analyzed in this thesis.

2.1.3 Nonspherical grain

The Mie theory assumes that dust grains are homogeneous and spherical, a convenient but simplified approximation. However, in reality, growth and destruction processes are expected to produce irregular grains that are inhomogeneous in structure, composition, and shape. Even the observed polarization of starlight requires that interstellar grains be both appreciably non-spherical and partially aligned (Hiltner, 1949). As starlight propagates through the dusty interstellar medium, it becomes linearly polarized due to the preferential attenuation of one of the linear polarization modes. In addition to this, aligned dust grains produce polarized thermal emission at wavelengths from the far-infrared to the microwave.

An extension of the classical theory to account for particles with inhomogeneous composition can be achieved through Effective Medium Theory (EMT), in which a grain is modeled as an aggregate of cells made of different materials.

The effect of nonspherical grains on the X-ray scattering halo is to make it non-azimuthally symmetric, since the scattering cross section becomes dependent not only on the scattering angle but also on the orientation of the grains with respect to incident radiation (Draine and Allaf-Akbari, 2006).

2.1.4 Pseudo-distance distribution approach

In Tiengo and Mereghetti (2006) a new method was proposed to visualize and detect an expanding X-ray ring. This approach involves constructing a *dynamical image*, where photon counts are binned according to a new coordinate system defined as:

$$X_i = t_i - t_B = \Delta t_i$$

$$Y_i = (x_i - x_B)^2 + (y_i - y_B)^2 = \theta_i^2,$$

where t_i is the arrival time of the i-photon, x_i and y_i the detected position, t_B the time of the burst, and x_B and y_B the detected burst position. In this representation, each point in the dynamical image corresponds to a specific angular distance and time delay. Stationary celestial sources appear as horizontal lines (constant angular position over time), while, according to Eq. 2.1, expanding X-ray rings manifest

themselves as inclined lines, with slopes inversely related to the distance of the scattering dust (Fig. 2.4).

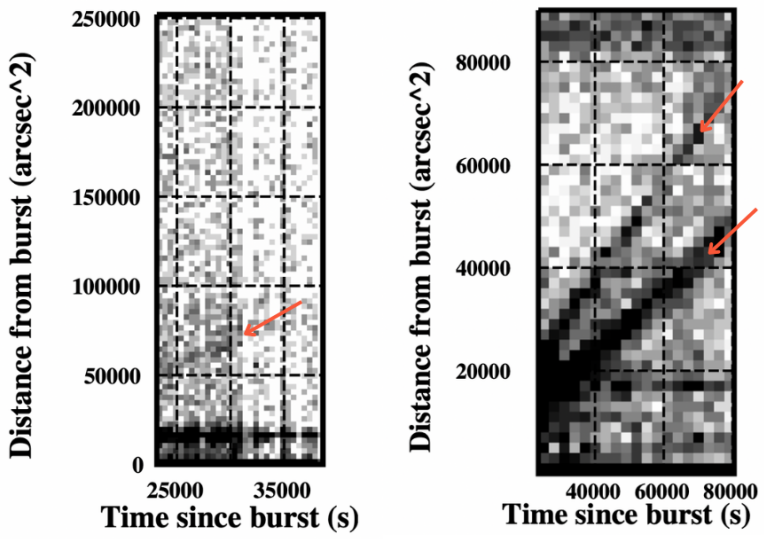

Figure 2.4: Dynamical images derived for *XMM-Newton* follow-up observations of GRB 050713A (left panel) and for GRB 031203 (right panel). The expanding rings are highlighted with orange arrows. Figure adapted from Tiengo and Mereghetti (2006).

Based on this coordinate transformation, a quantity known as the pseudo-distance can be defined as:

$$D_i = 2c\Delta t_i/\theta_i^2.$$

For events that are not related to dust-scattered photons, this quantity does not represent a true physical distance. However, for photons from a ring that expands according to Eq. 2.1, the pseudo-distance, D_i, corresponds to the distance of the dust grains that scattered them. Consequently, all the X-rays scattered by a given dust cloud are detected at times and positions corresponding to approximately the same values of D_i, resulting in a peak in the pseudo-distance distribution at the cloud's distance (Fig. 2.5).

2.2 X-ray absorption

As discussed in Sect. 1.1.1, when the energy of an incoming photon exceeds the binding energy of an atomic electron, the photon can ionize the atom by ejecting the electron with kinetic energy equal to $E - E_0$, where E is the photon energy and E_0 the electron binding energy.

In the X-ray regime, photon energies are sufficiently high to remove electrons from the innermost atomic shells (K, L, M). This produces characteristic discontinuities in the absorption spectrum, known as absorption edges, marked by a sudden

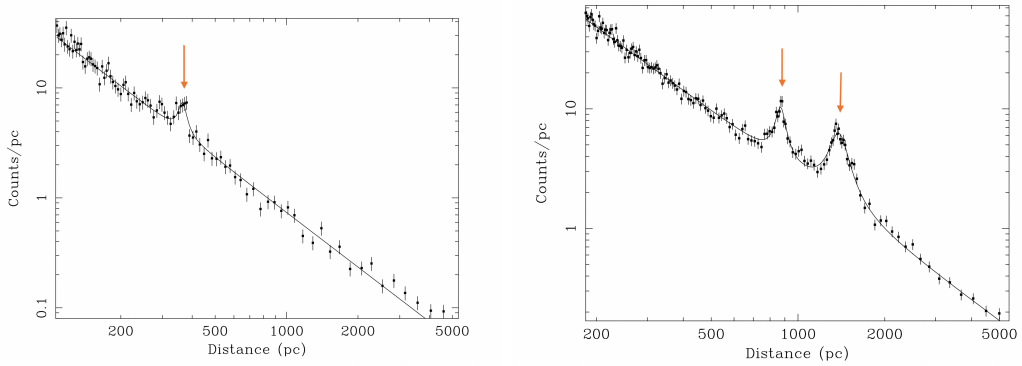

Figure 2.5: Pseudo-distance distribution from *XMM-Newton*/pn follow-up observations of GRB 050713A (left panel) and GRB 031203 (right panel). The peaks corresponding to the expanding rings shown in Fig. 2.4 are highlighted with orange arrows. Figure adapted from Tiengo and Mereghetti (2006).

drop in intensity at the binding energy of the ejected electron. Beyond the edge, the absorption probability decreases approximately exponentially, as photons with energies above the threshold penetrate more easily through the material, generating the typical sawtooth pattern (left panel of Fig. 2.6).

The presence of solid particles modifies these features, producing oscillatory modulations known as X-ray Absorption Fine Structure (XAFS, Costantini and Corrales 2022). In these cases, the incoming photon interacts with the electron in the shell as in the gas case, but the photoelectron produced interacts with the neighboring atoms, creating positive and negative interference (right panel Fig. 2.6). This diffraction pattern depends on the number of electrons and their distance to the nucleus, therefore revealing the chemical composition and crystallinity of the dust grains. The XAFS are usually divided into two main regimes: the X-ray absorption near-edge (XANES) which extends from about 5 to 10 eV below the edge threshold energy to about 50 eV above the edge; and the extended X-ray absorption fine structure (EXAFS), which extends from $\simeq$ 50 eV above the edge energy to some hundreds eV (Newville, 2004). The XANES are the results of multiple backscattering with neighbor atoms, instead the EXAFS are the product of single backscattering (Costantini and Corrales, 2022).

As already said, these features are sensitive to both the composition and the crystallinity of the dust grains and even to the dust size distribution. Therefore, modeling this feature offers a unique probe of dust physical properties. The possibility of observing the XAFS of interstellar grains through high-resolution X-ray spectroscopy was initially proposed by Martin (1970) and Evans (1986). However, the first fine structures due to dust were detected only in 2002 in the X-ray spectrum of the bright microquasar GRS 1915+105 (Lee et al., 2002). At that time, it was not possible to characterise them, since a proper X-ray extinction model was not available. The data in the literature on XAFS did not include measurements tailored for astronomical purposes. The lack of available models prompted laboratory measurement campaigns to create an adequate database of models (Lee and Ravel, 2005; Lee et al., 2009; Costantini and de Vries, 2013).

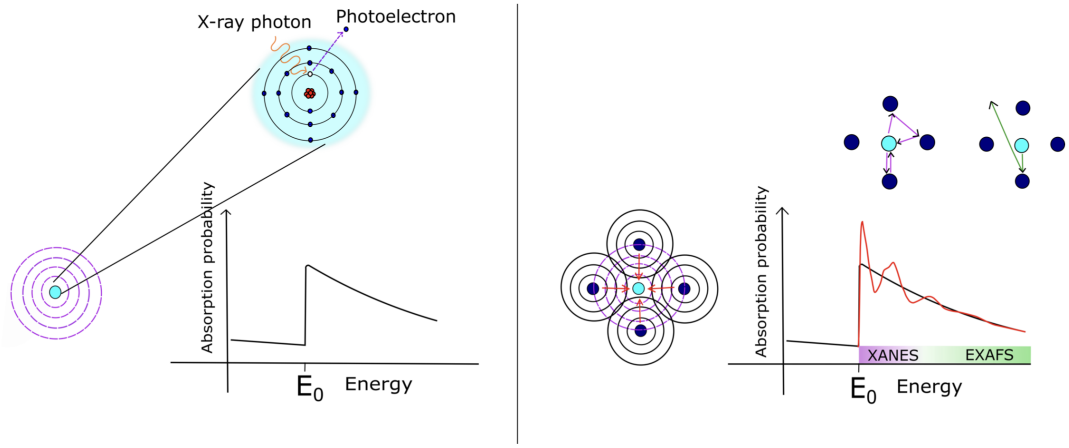

Figure 2.6: When X-ray photons interact with a gas (left panel), the resulting absorption cross section shows a sharp rise at the binding energy. In the presence of neighboring atoms (right panel), the photoelectron wave scatters, producing interference patterns that modulate the absorption spectrum. Figure from Costantini and Corrales (2022).

The spectra of X-ray binaries provide an excellent opportunity to study the absorption of dust and gas along their LOS. These systems are classified into two categories based on the mass of the companion star: Low Mass X-ray Binaries (LMXBs) and High Mass X-ray Binaries (HMXBs). LMXBs within our Galaxy are particularly well-suited for investigating XAFS due to their significant column densities, high flux, and relatively simple spectra. In fact, most LMXBs do not exhibit intrinsic absorption features below 10 keV, making them ideal for such studies.

2.2.1 X-ray laboratory studies

A laboratory campaign began in 2010 at SRON in the Netherlands (Costantini and de Vries, 2013), with the objective of developing extinction cross-section models for the analysis of absorption edges in X-ray spectra. For edges in the 1-10 keV energy range, synchrotron facilities were used to perform the measurements. In particular, laboratory data for the Si K and Mg K absorption edges were obtained at the LUCIA beamline (Line for Ultimate Characterization by Imaging and Absorption; Flank et al. 2006) of the SOLEIL synchrotron facility in Paris. This beamline operates in the 0.8–8 keV energy domain, providing access to the K-edges of low-Z elements, ranging from sodium to iron. The synchrotron measurements can be performed in either transmission or fluorescence configurations.

In the fluorescence configuration, the secondary X-ray emission produced by the sample under synchrotron irradiation is detected. These incident X-rays are sufficiently energetic to eject inner-shell electrons, leaving the atomic structure unstable. The vacancy is subsequently filled by an electron from a higher shell, releasing energy in the form of fluorescent X-rays. This signal provides information on the degree of absorption above the edge.

From such laboratory measurements, the imaginary part of the refractive index can be directly derived. The corresponding real part can then be calculated through

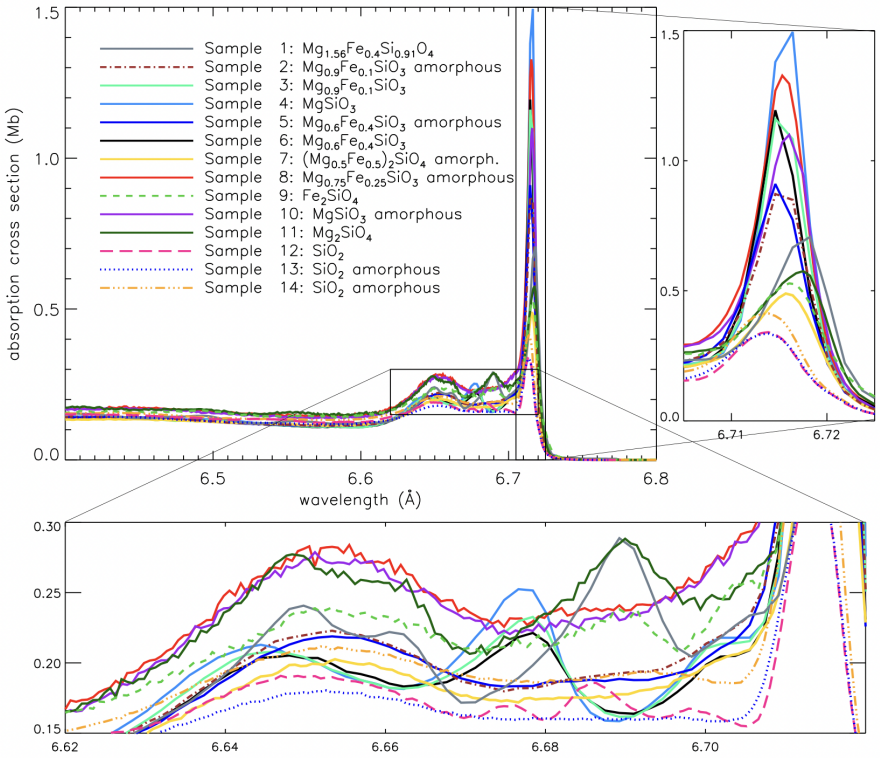

Figure 2.7: Figure from Zeegers et al. (2019), showing the absorption cross sections of the Si K-edge of silicate samples. The insets shows the XAFS whith more details, the differences between the crystalline structures of olivines and pyroxenes can be observed by comparison of e.g., sample 1 and 4. The effect of amorphization can be observed by comparing e.g., sample 2 and 3, where some of the XAFS features are absent in the amorphous sample.

the Kramers-Kronig relations (see Zeegers et al. 2019; Rogantini et al. 2019 for the procedure to obtain n from k, and Bohren 2010 for a review of the Kramers-Kronig formalism). As outlined in Sect. 2.1.1, the total extinction cross section is derived by integrating the extinction efficiency-computed here using the Anomalous Diffraction Theory (ADT; (van de Hulst, 1946))-over the particle size distribution. In this context, the ADT provides an approximation that is formally analogous to Mie theory.

The resulting models, covering different absorption edges and dust compositions, have been incorporated into the SPEX X-ray spectral fitting code (Kaastra et al., 2018). As an example, Figure 2.7 shows the resulting laboratory measurements of the Si K-edge (Zeegers et al., 2019).

Chapter 3

The X-ray dust scattering rings around GRB 221009A

3.1 Introduction

The gamma-ray burst (GRB) 221009A was first reported when its hard X-ray (>15 keV) emission triggered the Swift Neil Gehrels observatory/Burst Alert Telescope (*Swift*/BAT) instrument on 2022 October 9 at 14:10:17 UT (Dichiara et al., 2022). Due to its low Galactic latitude and long duration, it was initially believed to be a new Galactic transient. However, it soon became clear that *Swift*/BAT was triggered by the afterglow of a very bright and long GRB, which had been detected with the Gamma-Ray Burst Monitor (GBM; 10 keV-25 MeV) on board Fermi about 1 hr earlier (Kennea et al., 2022; Veres et al., 2022). Observations of the afterglow with X-shooter at ESO's UT3 of the Very Large Telescope determined a redshift of $z = 0.151$ (de Ugarte Postigo et al., 2022), which, assuming a flat ΛCDM cosmology with $H_0 = 67.4\ \mathrm{km\,s^{-1}\,Mpc^{-1}}$ and $\Omega_\mathrm{m} = 0.315$, corresponds to a luminosity distance of $d_L = 745$ Mpc (Malesani et al., 2023), placing it among the most energetic GRBs ever detected. GRB 221009A is, in fact, the brightest GRB ever recorded (Burns et al., 2023) and its prompt emission saturated most X-/gamma-ray instruments. It occurred in a direction close to the Galactic plane (b = 4°.32, l = 52°.96), resulting in the formation of 21 X-ray rings due to scattering by interstellar dust in our Galaxy (Tiengo et al., 2023; Vasilopoulos et al., 2023; Williams et al., 2023; Zhao and Shen, 2024). GRB 221009A presents a unique opportunity to investigate the Galactic ISM through X-ray scattering and absorption because of the combination of its exceptional fluence and its ideal position in Galactic coordinates. A GRB with this luminosity occurring at such a close distance is estimated to be a once-in-10,000-year event (Burns et al., 2023), and its line of sight intercepts all the Milky Way spiral arms up to a distance of nearly 20 kpc from us (Williams et al., 2023; Tiengo et al., 2023; Vasilopoulos et al., 2023). These X-ray dust scattering rings were observed by the X-ray Telescope (XRT) on *Swift* (Vasilopoulos et al., 2023; Williams et al., 2023), *XMM-Newton* (Tiengo et al., 2023), the *Imaging X-ray Polarimetry Explorer* (IXPE) (Negro et al., 2023), and *Chandra*.

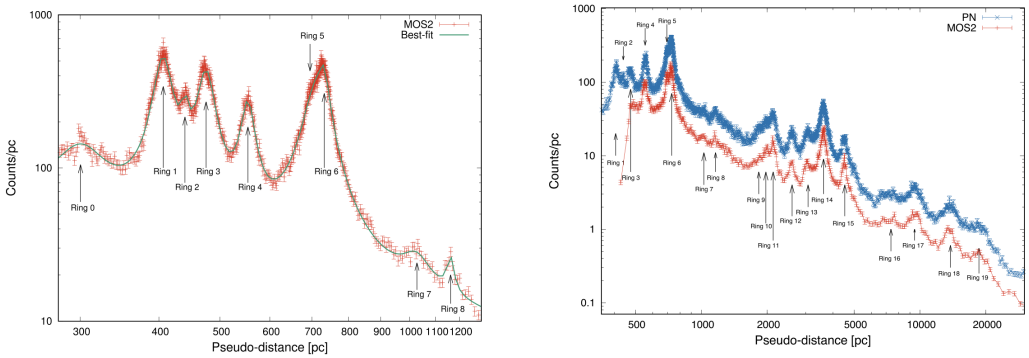

Figure 3.1: Pseudo-distance distributions in the 0.7–4 keV energy band for the two XMM-Newton observations (Obs1: left; Obs2: right). Arrows indicate the ring numbers as reported in Tiengo et al. (2023), which are also adopted in this thesis. MOS2 data are in red, pn in blue, and the green line in the left panel indicates the best-fit model with a power law plus 9 Lorentzian functions. Figure from Tiengo et al. (2023).

3.1.1 GRB 221009A soft X-ray prompt emission

Tiengo et al. (2023) derived the fluence and spectrum of the soft X-ray emission of GRB 221009A from the two observations of its dust-scattering rings, performed a few days after the GRB by the *XMM-Newton* satellite. The expanding dust-scattering rings were investigated using the method of the pseudo-distance distribution outlined in Section 2.1.4. The resulting pseudo-distance histograms from the two *XMM-Newton* observations (Fig. 3.1) exhibit multiple peaks, indicative of many discrete dust-scattering layers located at different distances along the line of sight.

Each instrument's histogram was independently modeled by fitting a combination of a power-law component (accounting for the background, which was not subtracted in this analysis) and multiple Lorentzian profiles. In total, twenty distinct dust layers were identified.

Among all detected rings, only the brightest one (ring 6) allowed a reliable estimate of the dust content in the cloud responsible for its formation, based on the available optical-IR extinction maps. Its spectrum (see Eq. 2.4) was therefore extracted and fitted using the XSPEC model: CONSTANT × TBABS × ZTBABS × RINGSCAT × PEGPWRLW. In this model, RINGSCAT accounts for the dust-scattering optical depth, calculated for different dust models characterized by various compositions and size distributions (e.g. Zubko et al. 2004; Mathis et al. 1977; Draine 2003). The constant term represents the inverse of the exposure time, while the prompt GRB emission is modeled as a power law (PEGPWRLW) modified by both Galactic (TBABS) and host-galaxy (ZTBABS, with redshift fixed at $z = 0.151$; Malesani et al. 2023) absorption, following the prescription of Wilms et al. (2000). The Galactic column density was fixed to $N_{\rm H,G} = 7 \times 10^{21}\,{\rm cm}^{-2}$, which is the average value inferred from the Planck two-dimensional dust map (Planck Collaboration et al., 2014) at the ring position. The dust column density of the cloud producing ring 6 was estimated from the extinction map of Lallement et al. (2022), which displays an excess corresponding to $\Delta N_{\rm H} = 8 \times 10^{20}\,{\rm cm}^{-2}$ at the cloud distance.

To distinguish between competing dust models and better constrain the spectral shape of the GRB 221009A prompt X-ray emission, Tiengo et al. (2023) performed a broader spectral fitting analysis using the same XSPEC model described above. This included a simultaneous fit of the spectra for rings 1–6 from Obs1, which were entirely within the MOS2 field of view and originate from dust located between 350 and 800 pc. Since the differential extinction due to each dust cloud could not be separated, the cumulative contribution in this distance range ($\Delta N_H = 4 \times 10^{21}\,\mathrm{cm}^{-2}$) was assumed (Lallement et al., 2022). Additionally, a separate fit was carried out using 19 rings, incorporating pn data from rings 7–19 in Obs2, and adopting a column density based on Lallement et al. (2022) of $\Delta N_H = 6.7 \times 10^{21}\,\mathrm{cm}^{-2}$, for the cumulative column density in the 19 dust clouds.

The results of these spectral fits are summarized in Table 3.1. Among the tested models, BARE-GR-B (see Sect. 1.2.5) provided the best match to the observed data, producing the most reliable estimation of the X-ray fluence of GRB 221009A in the 0.5–5 keV band: $2.6 \times 10^{-3}\,\mathrm{erg\,cm}^{-2}$, which is approximately an order of magnitude higher than the value derived by extrapolating the high-energy (>20 keV) prompt emission model to lower energies.

In this chapter, we use the same dataset of Tiengo et al. (2023) supported by observations with the XRT onboard *Swift* to study the distribution of interstellar dust responsible for scattering, both along the line of sight and in the plane of the sky. Here, we mostly focus on clouds within 800 pc, which can also be identified through optical extinction. Section 3.2 details the reduction of the observations, Section 3.3 outlines the analysis and the results, in Section 3.4 we discuss the results, and in Section 3.5 presents our conclusions. This work is published in Vaia et al. (2025).

3.2 Observations and data reduction

In this study, we examine *Swift*/XRT and *XMM-Newton* observations of GRB 221009A, performed between October 10 and October 14. The associated observation IDs are presented in Table 3.2. In later time observations, only the rings produced by the most distant clouds were fully covered (see Eq. 2.2). On the other hand, *Swift* exposures taken within 1 day from the GRB discovery were not considered because the windowed-timing mode was used and no 2D images were produced.

3.2.1 *XMM-Newton*

XMM-Newton observed GRB 221009A for 50 ks on October 11, 2022 (Obs1) and for 62 ks on October 14, 2022 (Obs2). To minimize pileup in Obs1, the EPIC pn (Strüder et al., 2001) and the two EPIC metal oxide semiconductor (MOS) cameras (Turner et al., 2001) were operated in timing mode, with the thick optical-blocking filter. In timing mode, only the peripheral CCDs of the MOS cameras offer full imaging capabilities from $\simeq 5'$ to $\simeq 15'$, from the target position. In Obs2, all EPIC cameras were in full-frame mode, and the thin optical filter was used. The second part of this observation was affected by strong and variable particle background.

Dataset	Dust model	$N_{H,z}$[a] (10^{21} cm^{-2})	Γ_{GRB}[b]	GRB fluence[c] (10^{-3} erg cm^{-2})	χ^2/d.o.f.
Ring 6[d]	BARE-GR-B	4.9±0.6	1.3±0.1	2.57±0.05	36.77/30
	BARE-GR-S	5.0±0.6	1.2±0.1	2.52±0.05	40.76/30
	BARE-GR-FG	5.0±0.6	1.2±0.1	2.52±0.05	39.77/30
	COMP-GR-B	5.8±0.6	1.2±0.1	4.2±0.1	45.55/30
	COMP-GR-S	5.3±0.5	1.05±0.09	4.4±0.1	34.57/30
	COMP-GR-FG	5.9±0.6	1.1±0.1	4.0±0.1	41.05/30
	MRN	6.7±0.6	1.5±0.1	2.03±0.04	44.57/30
	Draine (2003)	6.7±0.5	1.1±0.1	2.41±0.06	34.94/30
Rings 1–6[e]	BARE-GR-B	4.6±0.4	1.39±0.05	1.94±0.02	103.83/72
	BARE-GR-S	5.3±0.4	1.31±0.05	1.87±0.02	107.46/72
	BARE-GR-FG	5.6±0.4	1.32±0.05	1.89±0.02	117.45/72
	COMP-GR-B	5.6±0.4	1.17±0.05	3.09±0.03	110.10/72
	COMP-GR-S	6.7±0.4	1.08±0.05	3.23±0.04	143.07/72
	COMP-GR-FG	6.3±0.5	1.09±0.05	2.91±0.04	124.39/72
	MRN	7.5±0.5	1.44±0.05	1.55±0.02	141.06/72
	Draine (2003)	7.1±0.4	1.12±0.05	1.59±0.02	99.39/72
Rings 1–19[f]	BARE-GR-B	4.4±0.3	1.37±0.04	1.67±0.02	194.34/155
	BARE-GR-S	4.6±0.4	1.20±0.04	1.53±0.01	210.77/155
	BARE-GR-FG	4.6±0.3	1.18±0.04	1.54±0.01	235.18/155
	COMP-GR-B	5.1±0.2	1.08±0.04	2.47±0.03	204.99/155
	COMP-GR-S	5.2±0.2	0.86±0.04	2.52±0.03	298.95/155
	COMP-GR-FG	5.0±0.4	0.89±0.04	2.28±0.02	257.26/155
	MRN	6.0±0.4	1.21±0.04	1.24±0.01	302.54/155
	Draine (2003)	6.3±0.4	1.00±0.04	1.25±0.01	211.10/155

[a]Absorption in the host galaxy ($z = 0.151$). [b]Photon index of the GRB prompt emission [c]Unabsorbed GRB fluence in the 0.5–5 keV energy band. [d]PN and MOS2 spectra of ring 6 in Obs2, assuming ΔN_H=8×10^{20} cm^{-2} in the dust cloud. [e]MOS2 spectra of rings 1–6 in Obs1, assuming $\Delta N_H = 4 \times 10^{21}$ cm^{-2} in the 6 dust clouds. [f]MOS2 spectra of rings 1–6 in Obs1 and PN spectra of rings 7–19 in Obs2, assuming $\Delta N_H = 6.7\times10^{21}$ cm^{-2} in the 19 dust clouds.

Table 3.1: Best-fit parameters of the GRB prompt emission derived from different choices of dust-scattering rings and dust models, from Tiengo et al. (2023). All uncertainties are at 1 σ.

Table 3.2: Log of the *Swift*/XRT and *XMM-Newton* observations of GRB 221009A.

Satellite/Instrument	Obs. ID	Start time (UTC)	Stop time (UTC)	Exp. time
Swift/XRT	01126853004	2022-10-10T08:05:13	2022-10-10T17:23:57	3.0 ks
Swift/XRT	01126853005	2022-10-10T18:31:37	2022-10-10T19:02:39	1.5 ks
Swift/XRT	01126853006	2022-10-10T20:22:49	2022-10-11T13:50:34	13.0 ks
XMM-Newton/MOS2	0913991501	2022-10-11T20:52:49	2022-10-12T10:46:09	50.0 ks
Swift/XRT	01126853008	2022-10-12T01:15:43	2022-10-12T21:54:53	3.0 ks
Swift/XRT	01126853009	2022-10-13T00:42:50	2022-10-13T04:22:52	4.4 ks
XMM-Newton/MOS2	0913991601	2022-10-14T05:41:21	2022-10-14T22:52:21	33.5 ks
XMM-Newton/pn	0913991601	2022-10-14T05:41:21	2022-10-14T22:52:21	29.7 ks

Therefore, we limited the analysis to the longest uninterrupted time interval with quiescent background, resulting in a net exposure time of 33.5 ks for the MOS2 and 29.7 ks for the pn. We do not report the analysis of the MOS1 data for either observation due to the permanent damage sustained by two external CCDs during the early stages of the mission.

To subtract the contribution from the X-ray background as well as from the GRB afterglow and its possible dust-scattering halo in Obs2, without any contamination from X-ray rings, we searched for archival observations of extragalactic point sources with similar flux and spectrum and behind a significant amount of Galactic dust. As our best choice, we selected an observation of the bright high-redshift quasar RBS 315 (Observation ID: 0690900201) performed in January 2013, at a similar phase of the Solar Cycle, in order to have a similar contamination from the unfocused particle background (Gastaldello et al., 2022). This quasar is located in a relatively dusty region ($A_v = 0.7$, Schlafly and Finkbeiner 2011) and was observed by *XMM-Newton* in full-frame mode with the thin filter, as in Obs2.

The data were processed using Science Analysis Software (SAS) 20.0.0 (Gabriel et al., 2004) and the latest calibration files. The EPIC events were cleaned with standard filtering expressions[1]. Point-like sources were removed by excluding circular regions after running the SAS source detection task `emldetect`. For the spectral analysis response matrices were generated using the SAS tasks `rmfgen` and `arfgen`.

3.2.2 *Swift*-XRT

In this work, we analyzed *Swift* observations of GRB 221009A made with XRT from October 10 to October 13, all taken in photon-counting mode. The corresponding observation IDs are listed in Table 3.2. Additionally, we used late-time observations of the GRB performed in March and April 2023 (observation IDs from 01126853076 to 01126853084) to create a single sky background event file. We also employed observations from October 25-29, 2022 (Observation IDs 01126853023 to 01126853027), where the GRB afterglow was still present but the rings were sufficiently large and faint, to isolate the afterglow contribution.

The data were processed with standard procedures using the FTOOLS task `xrtpipeline`. Point-like sources were removed by excluding circular regions after source detection (we chose to exclude point-like sources with a signal to noise ratio > 3). For the spectral analysis the Redistribution Matrix File (RMF) was obtained from the calibration database released on 01-01-2013 and the Ancillary Response Files (ARFs) were created using the task `xrtmkarf` (imposing `psfcorr=no`).

3.3 Data analysis and results

Since *Swift*/XRT began observing GRB 221009A in photon-counting mode one day after the burst, it could observe rings formed by dust clouds at heliocentric distances smaller than 300 pc, which were already outside the EPIC field of view (FOV) during

[1]For pn data: `#XMMEA_EP&&(FLAG==0)&&(PATTERN<=4)` and for MOS: `#XMMEA_EM&&(PATTERN<=12)`.

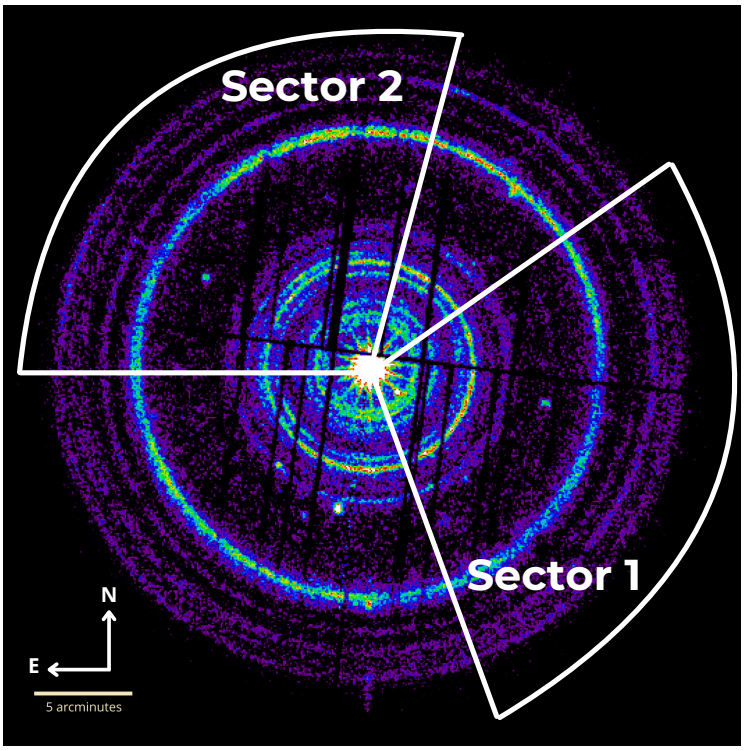

Figure 3.2: *XMM-Newton* combined X-ray observations of GRB 221009A, with the two sectors used for our analysis highlighted.

the *XMM-Newton* observations (see Eq. 2.2). Unfortunately, due to the telescope's off-axis pointing, we were not able to observe these rings across the entire *Swift*/XRT FOV, but only within a 105° wide sector (290° − 395°, measured counterclockwise from the West direction) which extended up to 14′ from the GRB. This sector, that we will call Sector 1 (see Fig. 3.2), represents therefore the only region in which we can map the dust distribution throughout the whole Galaxy (from $\sim$ 0.1 to $\sim$ 20 kpc). As noted in Tiengo et al. (2023), there are significant variations in the azimuthal distribution of the surface brightness of the brightest X-ray rings, which can be explained by the non-uniform distribution of dust in the intervening clouds. To exploit this azimuthal variation, we selected another sector with the same size as Sector 1 (Sector 2; see Fig 3.2). The selection of this sector was driven by the analysis of X-ray absorption in Obs2, as outlined in the following paragraph (3.3.1), which showed that Sector 2 (75° − 180°) is the only region with a significant $N_{\rm H}$ excess. This result is also confirmed by the total $N_{\rm H}$ map of the GRB 221009A region estimated from *Planck* submillimeter data of thermal dust emission (see Fig. 3.3).

3.3.1 Azimuthal Variability of X-ray absorption

To optimize the selection of azimuthal sectors for mapping the Galactic dust in the directions around the GRB 221009A position, a spectral analysis of annular sectors with similar numbers of counts was performed to evaluate the possible variation of X-ray absorption. The MOS2 field of view in Obs2 was divided into seven concentric

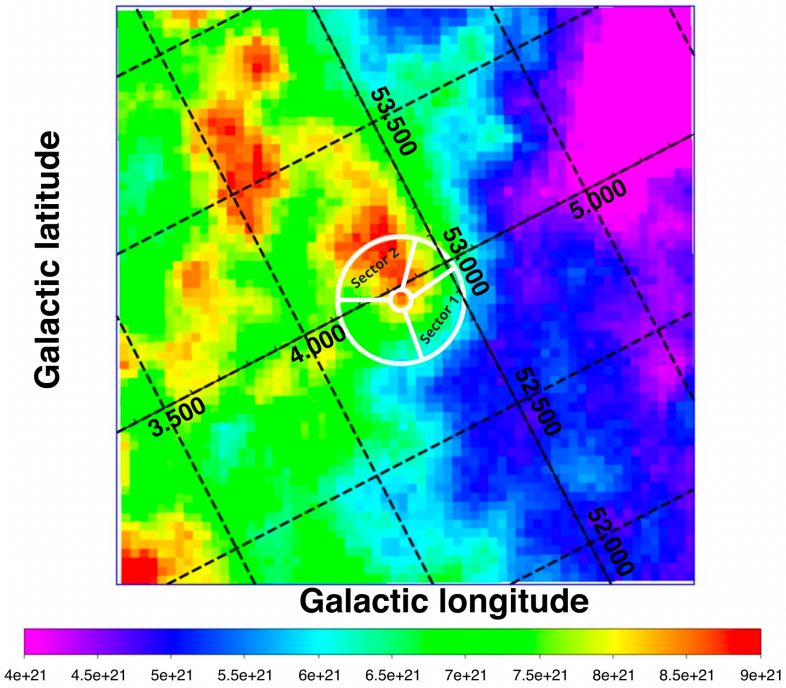

Figure 3.3: Map showing the total hydrogen column density in the sky region surrounding GRB 221009A (Planck Collaboration et al., 2014). White circles with radii of 2′ and 12′ mark the area covered by the X-ray rings observed with *XMM-Newton*, with the two sectors – used in this analysis – highlighted. The figure has been adapted from Tiengo et al. (2023).

annuli (labeled rings A through G) with adjacent scattering rings grouped together to form regions containing at least 8000 counts (Fig.3.4). Each ring was then further subdivided into eight sectors, ensuring that all sectors within the same ring had about the same number of counts (>1000, to maintain sufficient statistics). The background spectra were obtained from the same region but extracted from the late time observation made with *XMM-Newton* on November 11. The spectra of each annular sector were simultaneously fit using the XSPEC model already adopted in Tiengo et al. (2023) and already described in Section 3.1.1: CONSTANT × ZTBABS × TBABS × RINGSCAT × PEGPWRLW. For this analysis, we adopted the dust model that provides the best-fit to the spectra of the 19 X-ray rings studied in Tiengo et al. (2023) (see Table 3.1): BARE-GR-B. All the parameters were fixed to the best-fit values found in Tiengo et al. (2023), except for the Galactic absorption and the overall normalization (CONSTANT). An acceptable fit (χ^2/dof = 2207/2177; nhp = 32%) was obtained, which means that the angular dependence of the scattering cross-section (modeled by the RINGSCAT spectral component) and a spatially-variable Galactic absorption can fully explain the spectral variability detected across the MOS2 FOV. The best-fit Galactic absorption hydrogen column densities derived for each spectrum are shown in Fig. 3.5. Ring F, which contains the X-ray radiation scattered by dust at ∼700 pc (rings 5 and 6 in Tiengo et al. 2023), displays significant azimuthal variability, with a prominent absorption excess in sectors F3 and F4, which range from 94° to 180°. The level of X-ray absorption in the other sectors of this ring, $N_{\rm H}$=0.726 ± 0.018, is compatible with the constant values derived for the other rings with radii larger than ∼3′. For Ring A, containing rings 17–19, instead, we found a lower column density, but, at such small angles, both the subtraction of the X-ray afterglow and the calculation of the scattering cross-section are affected by larger systematic uncertainties.

3.3.2 Background subtraction

In Sectors 1 and 2, we analyzed the expanding dust-scattering rings using the pseudo-distance distribution (Tiengo and Mereghetti, 2006), discussed in 2.1.4. The subtraction of the contribution of events not produced by X-ray dust scattering to the pseudo-distance distribution is crucial to avoid overestimating the quantity of dust in our Galaxy. To analyze the *Swift*/XRT observations, we implemented a double background-subtraction technique to isolate the emission from the rings by removing contributions from both the sky and instrumental background and the GRB afterglow. First, we constructed a pseudo-distance distribution for each sector from late-time observations (Obs IDs from 01126853076 to 01126853084). These background distributions were generated by randomizing the time within the range of the *Swift*/XRT observations of the GRB during which the rings were visible and by measuring the angular distance from the GRB in sky coordinates.

To further remove the afterglow, we used a second set of observations taken about 15 days after the burst (Obs IDs from 01126853023 to 01126853027). By this time, the afterglow was still bright, but the flux of the X-ray rings was below the detection threshold. The pseudo-distance distribution for the afterglow in each sector was produced as for the late time observations, which, in turn, were used to obtain

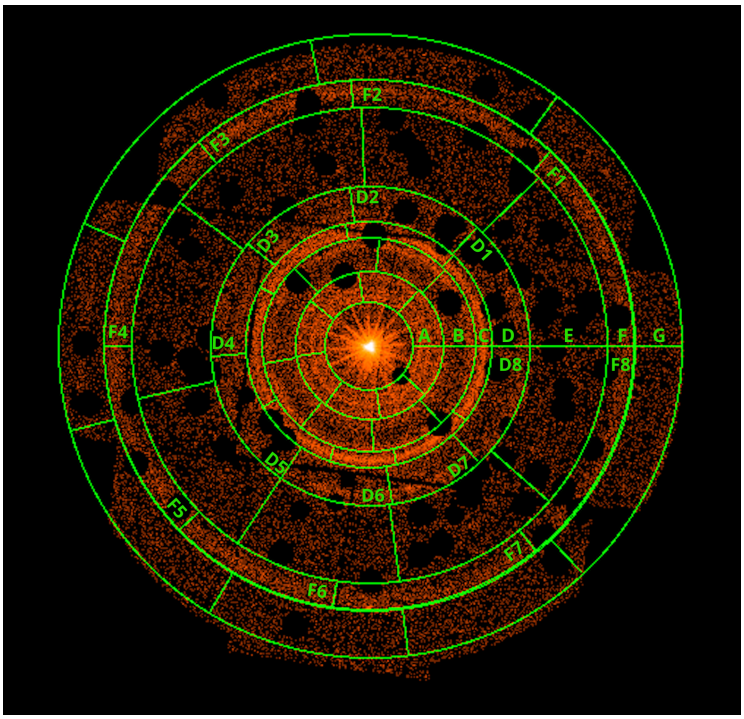

Figure 3.4: Annular sectors in which we performed the spectral analysis to evaluate the variation of X-ray absorption. The inner and outer radii for each ring are: Ring A (2′-3.37′), Ring B (3.37′-4.88′), Ring C (4.88′-5.62′), Ring D (5.62′-7.27′), Ring E (7.27′-10.85′), Ring F (10.85′-12.1′), and Ring G (12.1′-14.2′). Each ring is divided into 8 sectors containing the same number of counts.

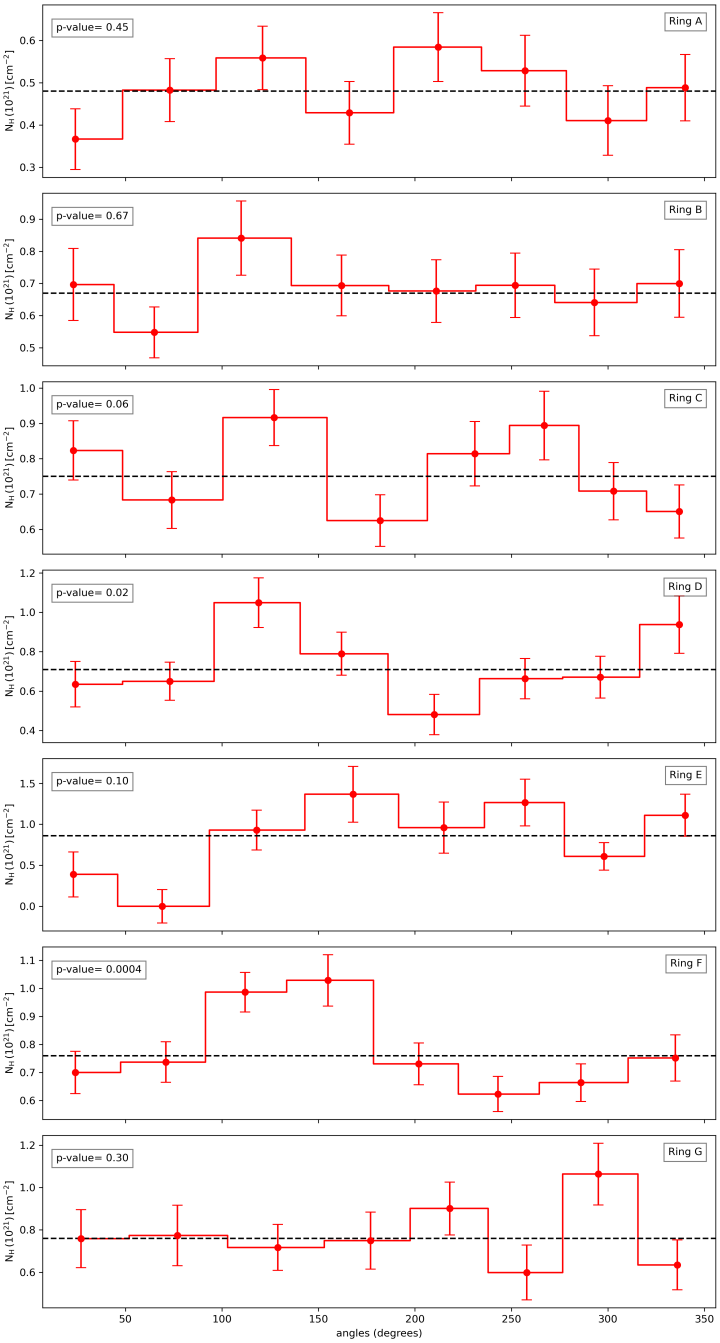

Figure 3.5: X-ray absorption for the seven rings derived from the spectral analysis using the model: CONSTANT × ZTBABS × TBABS × RINGSCAT × PEGPWRLW. Each sector within the same region is fit with a constant, yielding acceptable fits (p-value displayed in the upper left of each plot) for all rings except for ring F.

a background-subtracted afterglow distribution. Such distributions were then enhanced by a factor corresponding to the ratio of the average afterglow flux in the 0.3 - 5 keV energy band measured during the observations from 10 to 13 October (when the rings were detected) and from 25 to 29 October (from which we extracted the pseudo-distance distribution of the afterglow). To obtain the net contribution from the X-ray dust scattering halo, we therefore subtracted from the original pseudo-distance distributions of the two sectors both these afterglow distributions and those obtained for the background at late times.

In the two *XMM-Newton* observations, we did not utilize late-time observations as background, due to the residual contamination by X-ray dust scattering. Instead, we subtracted both the sky background and the afterglow contribution using a single observation of a different target (RBS 315; see Section 3.2.1 for details).

For the first *XMM-Newton* observation (Obs1), the subtraction was straightforward, involving a direct subtraction between the two pseudo-distance distributions, where angular distances were calculated in detector coordinates and the arrival times of the events in the background observation were randomly attributed in the time interval covered by Obs1. In contrast, the subtraction in the second *XMM-Newton* observation (Obs2) was complicated by the presence of an anomalous electronic noise in some MOS2 CCDs. Specifically, the ratio between the counts in individual CCDs and the total counts in the 5-10 keV band (where the X-ray rings are not detectable) showed an excess with respect to Filter Wheel Closed (FWC) exposures[2]. For Obs1 and the background observation, instead, the count ratios of every CCD were consistent with those observed in the FWC exposures.

To account for this anomalous background in Obs2, we rescaled the background pseudo-distance distribution of each CCD before performing the subtraction. The scaling factor was the ratio between the 5-10 keV counts in Obs2 and those in the background observation for each CCD.

3.3.3 Galactic Dust Distribution

After constructing the histogram of the pseudo-distances for each sector (already presented in Tiengo et al. 2023 for the whole FoV) and subtracting the background, we transformed this count distribution $C(D)$ into the equivalent hydrogen column density of the dust $\Delta N_{\rm H}(D)$. This parameter can be obtained from our spectral model because the dust model is normalized to the number of hydrogen atoms (Zubko et al., 2004). For this transformation, we used a conversion factor $f(\theta, t)$ that must be computed separately for each angular distance from the GRB position (θ) and for each observation, accounting for the time elapsed since the GRB (t), the exposure duration, and the detector efficiency.

To compute the conversion factors $f(\theta, t)$, which allow us to transform the pseudo-distance distributions $C(D)$ into the equivalent hydrogen column density of the dust $\Delta N_{\rm H}(D)$, we divided the two sectors into annular regions, with a width

[2]The EPIC CCD cameras on board *XMM-Newton* are equipped with a filter wheel system and 6 different filter setups, including a closed position, in which the sky is blocked by a $\sim$ 1 mm thick layer of Aluminum. The FWC exposures, which are dominated by the instrumental background, are typically used to model and subtract the internal instrumental background of the *XMM-Newton* EPIC CCD cameras.

of 30″, ranging from 2′ to 12′ and extracted the corresponding spectra. For each spectrum, a specific response matrix was generated. Using XSPEC (Arnaud, 1996), we calculated the expected number of detected counts in each spectrum $C(D)$ for a fixed amount of dust, calculating the distance D from Eq.2.2, where t is the time elapsed between the GRB and the middle of the observation and θ is the average radius of the spectral extraction region. For the scattered emission, we adopted the model reported in Tiengo et al. (2023) and already described in this chapter: CONSTANT × ZTBABS × TBABS × RINGSCAT × PEGPWRLW. In this case, the CONSTANT is the inverse of the exposure time, adjusted by the ratio of the sector's angular dimension to the full circle (105°/ 360°) and the amount of dust in RINGSCAT is fixed to $\Delta N_{\rm H} = 10^{21}{\rm cm}^{-2}$. All the other spectral parameters, including the GRB fluence of $F_{\rm GRB} = 2.6 \times 10^{-3}\,{\rm erg\,cm}^{-2}$, are fixed to the best-fit values reported in Tiengo et al. (2023). The conversion factor $f(\theta, t)$ for each dataset, in units of $10^{21}{\rm cm}^{-2}$, is therefore the inverse of the number of expected counts in the 0.7–4 keV energy band, from which the pseudo-distance distributions were extracted.

Applying these conversion factors, we obtained the differential hydrogen column density distribution shown in Fig. 3.6 for the two sectors in the two MOS2 datasets and only for Sector 1 in the combined XRT observations (see Table 3.2), which allow us to sample nearby dust. The $N_{\rm H}$ distributions obtained across the entire field of view for both MOS and pn cameras were compared and found to be consistent. However, in this work, we report the $\Delta N_{\rm H}$ maps only for the MOS2 camera, as it provides better coverage of Sector 1. Fig. 3.6 demonstrates that the various datasets within the same sector are compatible with each other.

Due to the short duration of the GRB prompt emission, the brightness of the X-ray rings in different observations does not depend on the time variability of the source, but only on the spatial distribution of dust and on the angular dependence of the scattering cross-section, according to the selected dust model. To evaluate the azimuthal uniformity of the dust clouds at different angular distances (θ), we generated the diagrams in Fig. 3.7, which display the integrated $N_{\rm H}$ for the four main peaks in Fig. 3.6 observed by both the *Swift* and *XMM-Newton* satellites. In these charts, data for Sector 1 were represented as positive values of θ, while the data for the other sector are shown as negative values. To reduce uncertainties, *Swift* observations from multiple orbits were merged. From these figures, it is evident that the clouds at 406 pc (ring 1), 550 pc (ring 4), and the cloud complex at 700 pc (ring 5 and 6) contain more dust in Sector 2 than in Sector 1. On the contrary, for the cloud at 475 pc (ring 3), we do not detect any significant variability. The inset of the last panel in Fig. 3.7 illustrates the contributions of the two clouds within the cloud complex at ∼700 pc in Sector 1: ring 6 dominates up to 10′, but at larger angular distances, covered by the second *XMM-Newton* observation, it fades away and the contribution from the cloud at 695 pc (ring 5) becomes predominant.

3.3.4 Absorption in the host galaxy

In addition to the variation in ring intensity across the two different sectors (discussed in Sect. 3.3.3), we also detect spectral differences, which, as already shown in Sect. 3.3.1, can be explained by a different amount of Galactic absorption. The com-

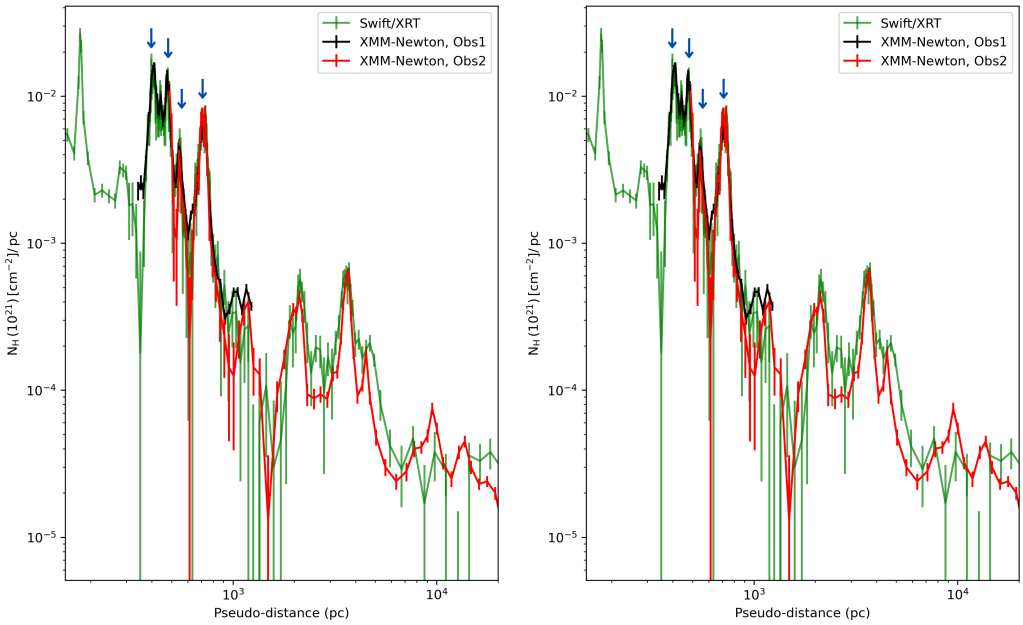

Figure 3.6: Left panel: Differential Hydrogen column density in Sector 1; in green *Swift*-XRT data, in black the data obtained from the first *XMM-Newton* observation and in red the data obtained from the second *XMM-Newton* observation. Right panel: Differential Hydrogen column density in Sector 2; in black the data obtained from the first *XMM-Newton* observation and in red the data obtained from the second *XMM-Newton* observation. The blue arrows highlight the four main peaks observed by both *XMM-Newton* and *Swift* satellites.

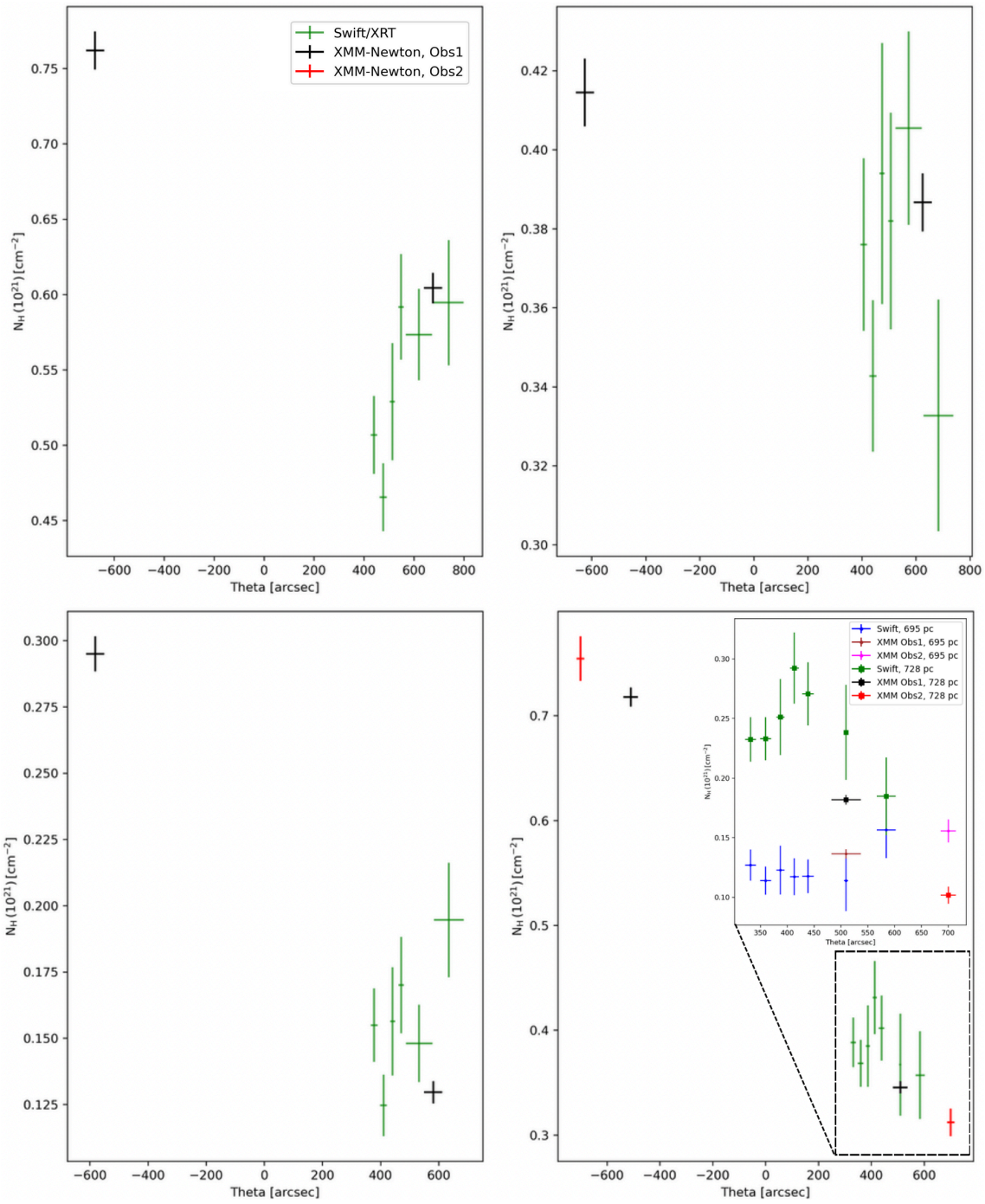

Figure 3.7: Hydrogen column density obtained by integrating the pseudo-distance distribution at the four main peaks in Fig. 3.6 (highlighted with blue arrows), centered at 406.3 pc (ring 1; upper left panel), 475.2 pc (ring 3; upper right panel), 553.6 pc (ring 4; bottom left panel) and ∼700 pc (rings 5 and 6; bottom right panel). The inset of the last panel shows the two clouds around 700 pc as separate values: the circles refer to the peak at 695.4 pc (ring 5; *Swift*-XRT in blue, *XMM-Newton* in brown for Obs1, and pink for Obs2) and the squares to the peak centered at 728.6 pc (ring 6; *Swift*-XRT in green, *XMM-Newton* in black for Obs1, and red for Obs2). In all the other panels the values from *Swift*-XRT observations are shown in green, and from *XMM-Newton* observations in black (Obs1) and red (Obs2).

bined analysis of the spatially-resolved intensity and absorption of the dust-scattered X-ray emission of GRB 221009A enables us to distinguish between Galactic absorption and the contribution from the host galaxy. Specifically, the intensity of the X-ray rings allows for the quantification of dust along the line of sight within our Galaxy, while the X-ray absorption in the ring spectra is produced by the combined effect of the ISM both in our Galaxy and in the host galaxy. By assuming a dust-to-gas ratio and subtracting these values, we can determine the amount of dust (and gas) present in the host galaxy.

To calculate the total X-ray absorption for each sector, we selected the annular regions with the largest signal-to-noise ratio. We extracted the ring spectra from the first *XMM-Newton* observation within the angular ranges from $8'$ to $9'$ (covering rings 5 and 6) and from $9'$ to $12'$ (including rings 1–4). For the second *XMM-Newton* observation, we extracted the spectra in the angular range from $11'$ to $12'$ (containing rings 5 and 6), utilizing data from both the MOS2 and the pn cameras. For each spectrum, the background was extracted from the same detector region in the RBS 315 observation. We fit simultaneously the spectra of each ring with the XSPEC model: CONSTANT × TBABS × RINGSCAT × PEGPWRLW, where, at odds with the model described in Sect. 3.3.1, TBABS includes the cumulative absorption from the ISM in our Galaxy and in the host galaxy. The angles in the RINGSCAT spectral component were fixed to the limits of each ring and all the other spectral parameters, except for $N_{\rm H}$ in TBABS and the value of the CONSTANT,[3] were linked to the same values for the spectra of the two sectors. With this model, we obtained a good fit: $\chi^2/{\rm dof} = 140.4/150$, corresponding to a null-hypothesis probability (nhp) of 96.5%. The best-fit photon index of the power-law component ($\Gamma = 1.38 \pm 0.05$) is perfectly consistent with the one derived, making similar assumptions, in Tiengo et al. (2023) for the full rings (see Tab. 3.1) and, as anticipated by Section 3.3.1, the absorption in the two sectors is significantly different: $N_{\rm H,abs\,1} = (9.6 \pm 0.2) \times 10^{21}\,{\rm cm}^{-2}$ and $N_{\rm H,abs\,2} = (12.0 \pm 0.2) \times 10^{21}\,{\rm cm}^{-2}$ for sector 1 and 2, respectively. This confirms that the spectral differences between the two sectors can be fully attributed to Galactic X-ray absorption and we do not find any evidence for a different scattering cross-section in the two sectors. Significant spectral differences would be expected in case of strong spatial variability of the dust population (see, e.g., the spectral parameters obtained in Tiengo et al. 2023 for different dust models in Tab. 3.1) or for non-spherical grains (Draine and Allaf-Akbari, 2006).

For both sectors, we produced the cumulative $N_{\rm H}$ in our Galaxy from ring emission (left panel of Fig. 3.8) by integrating the corresponding pseudo-distance distributions, starting from the largest distances. To complete the cumulative distribution for Sector 2, we assumed the same dust concentration as in Sector 1 for distances smaller than 300 pc. We utilized *Swift* data up to 300 pc, Obs1 data up to 900 pc, and, beyond 900 pc, we used data derived from Obs2. The total integrated values for sector 1 and 2 are $N_{\rm H,sca\,1} = (4.34 \pm 0.04) \times 10^{21}\,{\rm cm}^{-2}$ and $N_{\rm H,sca\,2} = (5.54 \pm 0.04) \times 10^{21}\,{\rm cm}^{-2}$, respectively.

Although the difference between the final value of the cumulative dust distribution ($\Delta N_{\rm H,sca} = N_{\rm H,sca\,2} - N_{\rm H,sca\,1}$) and the total X-ray absorption ($\Delta N_{\rm H,abs} =$

[3]Since we are interested only in the spectral shape to constrain the absorption, we can ignore the brightness of the X-ray rings.

$N_{\mathrm{H,abs\,2}} - N_{\mathrm{H,abs\,1}}$) in the two sectors should be consistent, since it does not depend on the absorption in the host galaxy, we found significantly different values: $\Delta N_{\mathrm{H,sca}} = (1.20 \pm 0.06) \times 10^{21}\,\mathrm{cm}^{-2}$ and $\Delta N_{\mathrm{H,abs}} = (2.4 \pm 0.3) \times 10^{21}\,\mathrm{cm}^{-2}$.

This discrepancy is likely due to some of the assumptions made during the computation of the cumulative dust map ($N_{\mathrm{H,sca}}$). For instance, as described in Sect. 3.3.3, we adopted a GRB fluence based on the values reported in Tiengo et al. (2023). However, this measurement is affected by the systematic uncertainties discussed in Section 3.4.4. Since $N_{\mathrm{H,sca}}$ is inversely proportional to the GRB fluence (see Eq. 2.4), to reconcile the observed values, we could assume a 1.9 times lower GRB fluence. This adjustment results in the cumulative distributions shown in the central panel of Fig. 3.8 and an absorption in the host galaxy of $N_{\mathrm{H,z=0.151}}(1.8 \pm 0.3) \times 10^{21}\,\mathrm{cm}^{-2}$. The second assumption involves the extrapolation to small distances for the cumulative distribution of Sector 2, which is assumed to be the same as that of Sector 1. By instead assuming an excess of dust by a factor of 2.6 in the dust clouds at distances smaller than 300 pc in Sector 2, we obtain the cumulative dust distributions shown in the right panel of Fig. 3.8, and the resulting absorption in the host galaxy is $N_{\mathrm{H,z=0.151}} = (7.0 \pm 0.3) \times 10^{21}\,\mathrm{cm}^{-2}$. A more robust estimate of $N_{\mathrm{H,z=0.151}}$ can be derived from the detailed comparison of our dust distance distributions with 3D optical extinction maps, which will be discussed in the next section.

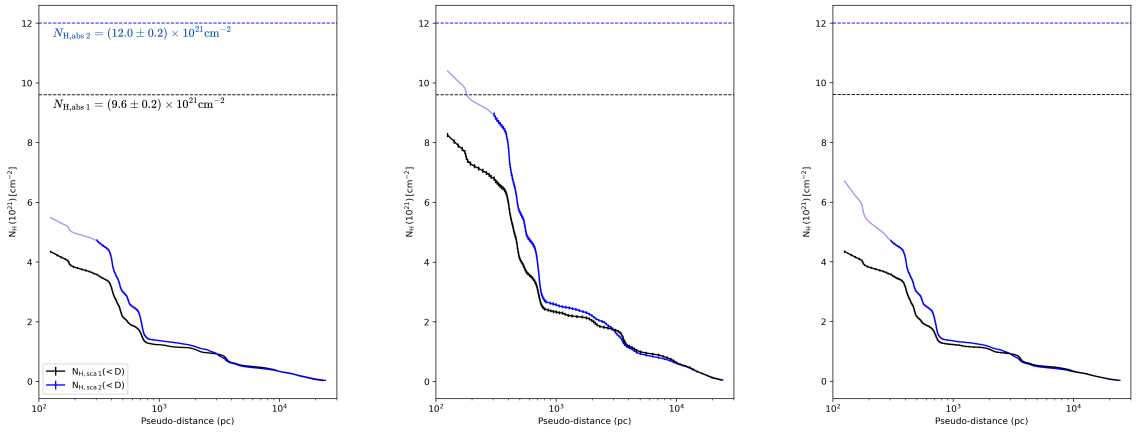

Figure 3.8: Cumulative hydrogen column density in our Galaxy for Sector 1 (black solid lines) and Sector 2 (blue solid lines) derived from ring emission under different assumptions: GRB fluence from Tiengo et al. (2023) (left panel); 1.9 times lower fluence than in Tiengo et al. (2023) (middle panel); GRB fluence from Tiengo et al. (2023) and 2.6 times more dust in Sector 2 than in Sector 1 within 300 pc (right panel). In the first two panels, the same dust concentration is assumed for both sectors at distances < 300 pc. The dashed lines (black for Sector 1, blue for Sector 2) indicate the total hydrogen column density, including contributions from both our Galaxy and the host galaxy, measured from the absorption inferred from X-ray spectral fitting.

3.4 Discussion

We can compare the dust map derived from X-ray scattering with other maps generated in the direction of GRB 221009A using data at various wavelengths. Here we focus on the 3D extinction maps from Lallement et al. (2022), Edenhofer et al. (2024), and Green et al. (2019).

3.4.1 Comparison with the Lallement map

The extinction map constructed by Lallement et al. (2022) integrates *Gaia* Early Data Release 3 (EDR3) and 2MASS photometric data with *Gaia* EDR3 parallaxes. This map has a distance resolution of 25 pc and an angular resolution greater than 1° in the plane of the sky[4].

Such angular resolution is not sufficient to separately probe the directions of the two sectors sampled by the X-ray data. However, most extinction increases in the Lallement et al. (2022) map extracted in the direction of GRB 221009A occur at the same distances as the peaks of the pseudo-distance distributions of the two sectors (left panel of Fig. 3.9). This confirms the results reported by Šiljeg et al. (2023) for the dust distribution averaged over the full FOV.

Thanks to the conversion factors described in Sect. 3.3.3 and adopting the $A_{\rm v}$ to $N_{\rm H}$ relation derived in Tiengo et al. (2023) ($N_{\rm H}/A_{\rm v} = 1.9 \times 10^{21} {\rm cm}^{-2}\,{\rm mag}^{-1}$), we can compare the peak heights as well. Taking into account the lower angular resolution of the Lallement et al. (2022) map, the peak values are in good agreement. In fact, the extinction features that display the largest discrepancies correspond to peaks in the pseudo-distance distributions with the most prominent differences in the two sectors, which indicate a significant gradient in the dust spatial distribution of the associated cloud. Moreover, features present in the Lallement et al. (2022) map but not detected through X-ray dust-scattering, such as the one at 650 pc, are likely due to dust clouds located at angular distances from the GRB position exceeding the radius of the largest X-ray ring ($\sim$12′, corresponding to 2.3 pc at this distance) or to spurious structures generated by the interpolation procedure required by the scarcity of suitable stars in the sampled volume Lallement et al. (2022).

3.4.2 Comparison with the Edenhofer map

The 3D dust differential extinction map presented by Edenhofer et al. (2024) is based on distance and extinction estimates for 54 million nearby stars, derived from *Gaia* BP/RP spectra. This map offers improved angular resolution compared to the Lallement et al. (2022) map (up to 14′), with distance resolution varying from 0.4 pc at 69 pc to 7 pc at 1.25 kpc. It is publicly accessible through the DUSTMAPS Python package (Green, 2018). The map provides unitless extinction values as defined in Zhang et al. (2023). To convert it to Johnson's V-band, we apply a factor of 2.8 (Zhang et al., 2023), and then convert it to $N_{\rm H}$ using the $A_{\rm v}/N_{\rm H}$ conversion factor from Tiengo et al. (2023).

[4]The map is publicly available on the EXPLORE website: `https://explore-platform.eu`.

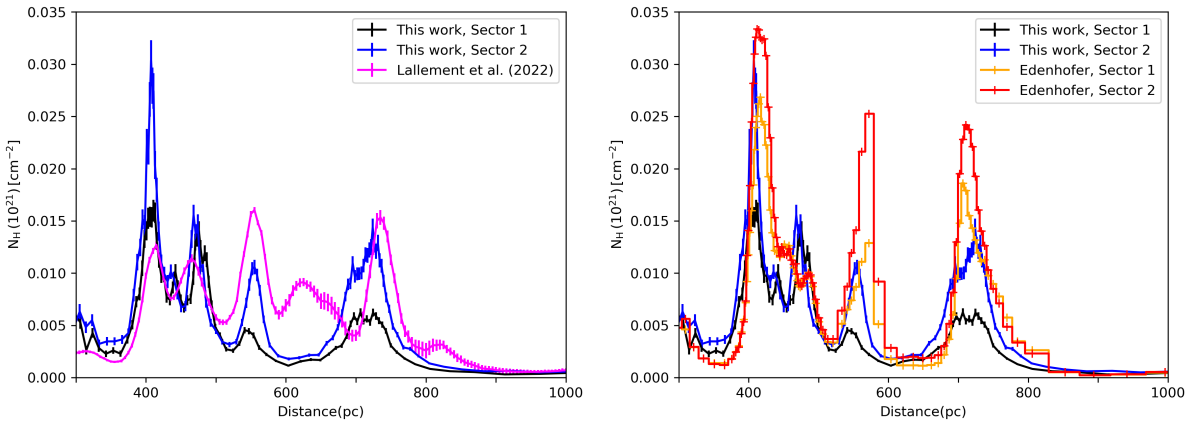

Figure 3.9: Differential hydrogen column density derived from X-ray dust scattering for Sector 1 (black) and Sector 2 (blue), compared to 3D optical extinction maps. In the left panel, the values derived by Lallement et al. (2022) are displayed in pink, while in the right panel the differential hydrogen column density from Edenhofer et al. (2024) is presented in orange for Sector 1 and in red for Sector 2. A conversion factor of $1.9 \times 10^{21} \mathrm{cm}^{-2}\,\mathrm{mag}^{-1}$ between N_H and A_v was used.

Thanks to the better resolution of the Edenhofer et al. (2024) map, in this case we can extract the differential extinction map for Sector 1 (RA = 288.10°, Dec = 19.71°) and Sector 2 (RA = 288.38°, Dec = 19.90°) and compare them with the corresponding pseudo-distance distributions (right panel of Fig. 3.9). The three main peaks emerging in the Edenhofer et al. (2024) map are not only at compatible distances, but they also have similar relative heights, with systematically higher values in sector 2. The corresponding peak values, instead, are always larger in the Edenhofer et al. (2024) map, which suggests a lower fluence for the GRB prompt emission. The pseudo-distance distribution peaks at ∼440 pc (ring 2) and ∼480 pc (ring 3) are not resolved in the Edenhofer et al. (2024) map, which however confirms the spatial uniformity of dust at these distances. Moreover, the Edenhofer et al. (2024) map does not detect the features around ∼600 pc and ∼800 pc, which are present in the Lallement et al. (2022) map but not in our pseudo-distance distributions. The images shown in Fig. 3.10 allow us to confirm one of the hypothesis formulated above to interpret this discrepancy: the broad bump above 600 pc is very likely caused by the dust cloud visible in the North-East direction in the 567–639 pc distance bin (central right panel of Fig. 3.10), which vanishes at ∼1° from the GRB, well beyond the region explored by X-ray observations (highlighted in white). Similarly, in the 740–812 pc bin (bottom right panel of Fig. 3.10), another dust cloud outside the FOV of the X-ray instruments is probably responsible for the small bump detected by Lallement et al. (2022) above 800 pc (left panel of Fig. 3.9). Fig. 3.10 also presents the extinction maps in the distance bins where dust clouds are observed though X-ray scattering. These figures clearly show the morphology of such clouds in the sky plane and confirm that for most clouds Sector 2 contains more dust compared to Sector 1.

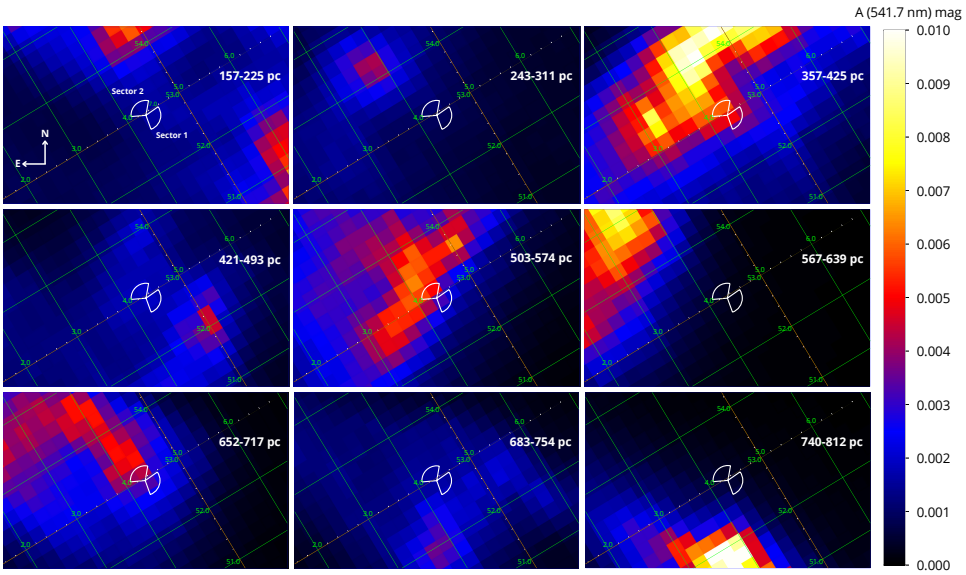

Figure 3.10: Extinction maps at $\lambda = 541.7$ nm from Edenhofer et al. (2024) in the direction of GRB 221009A, integrated in the following distance intervals: 157–225 pc (top left panel), 243–311 pc (top central panel), 357–425 pc (top right panel), 421–493 pc (central left panel), 503–574 pc (central panel), 567–639 pc (central right panel), 652–717 pc (bottom left panel), 683–754 pc (bottom central panel), and 740–812 pc (bottom right panel). The regions covered by the two sectors studied in this work are highlighted in white in each panel. The green grid indicates the Galactic coordinates in degrees.

3.4.3 Comparison with the Green map

The Green et al. (2019) map combines stellar photometry from *Gaia* Data Release 2 (DR2), Pan-STARRS 1, and 2MASS to provide extinction estimates with *Gaia* DR2 parallaxes. The map provides cumulative extinction across sight lines in 120 logarithmically spaced distance bins ranging from 63 pc to 63 kpc. In the direction of GRB 221009A, extinction can be measured for stars at distances from ∼0.3 to ∼5 kpc, extending well beyond the volume covered by the Lallement et al. (2022) and Edenhofer et al. (2024) maps. The angular resolution varies between 3.4′ and 13.7′, depending on the region of the sky. This map is also publicly available via the Python package DUSTMAPS. It provides extinction values in arbitrary units, which we converted to A_v using the conversion formula outlined in Green et al. (2019) (see Table 1 and Eq. 30).

We compared our pseudo-distance distributions in the two sectors with those from Green et al. (2019), using the $A_v - N_H$ conversion factor from Tiengo et al. (2023). The comparison was carried out by extracting the Green et al. (2019) maps of Sector 1 (brown in Fig. 3.11) and Sector 2 (green in Fig. 3.11) from the same directions chosen for the Edenhofer et al. (2024) maps in section 3.4.2. As shown in the left panel of Fig. 3.11, the pseudo-distance distributions (Sector 1 in black and Sector 2 in blue) yield a total N_H along the line of sight within our Galaxy that is lower than the values found by Green et al. (2019) in the same sector. As already discussed in Sect. 3.4.2, this discrepancy could result from our choice of the GRB fluence which, as explained in Tiengo et al. (2023), is affected by large systematic uncertainties. For example, by decreasing the GRB fluence by a factor of 1.35, the cumulative N_H obtained from X-ray dust scattering in Sector 1 matches that of the Green map in the same sector at ∼ 700 pc and at 5 kpc and the one of Edenhofer et al. (2024) (reported in orange in Fig. 3.11) from 700 pc to 1 kpc. The total value of $N_{H,sca\,1} = (6.07 \pm 0.05) \times 10^{21}\,cm^{-2}$ is consistent with the average value provided by the Planck Collaboration et al. (2014) 2D map in Sector 1: $N_H = (6.3 \pm 0.4) \times 10^{21}\,cm^{-2}$. The absorption value in the host galaxy found with this revised fluence is $N_{H,z=0.151} = (3.7 \pm 0.3) \times 10^{21}\,cm^{-2}$. The difference $\Delta N_H = 2.48 \times 10^{21}\,cm^{-2}$ between the values derived by Green et al. (2019) for the two sectors at 5 kpc (the farthest distance at which Green et al. 2019 can estimate stellar extinction) is consistent with the difference in X-ray absorption in the two sectors derived from the spectral analysis described in Sect. 3.3.4 ($\Delta N_{H,abs} = 2.4 \pm 0.3 \times 10^{21}\,cm^{-2}$). On the contrary, even assuming the reduced fluence, the excess of dust in Sector 2 derived from X-ray scattering is significantly smaller: $\Delta N_{H,sca} = (1.63 \pm 0.07) \times 10^{21}\,cm^{-2}$. To achieve a compatible value, the dust content within 300 pc in Sector 2 should be ∼1.6 times greater than that in Sector 1 at the same distance. Finally, we note that, as the X-ray absorption is primarily due to gas along the line of sight, these values could also be reconciled by assuming a different dust-to-gas ratio (see, e.g., Zhu et al. 2017).

3.4.4 Impact on GRB 221009A properties

Our last estimate of the X-ray absorption in the host galaxy, $N_{H,z=0.151} = (3.7 \pm 0.3) \times 10^{21}\,cm^{-2}$, is significantly smaller than the value obtained by Williams et al.

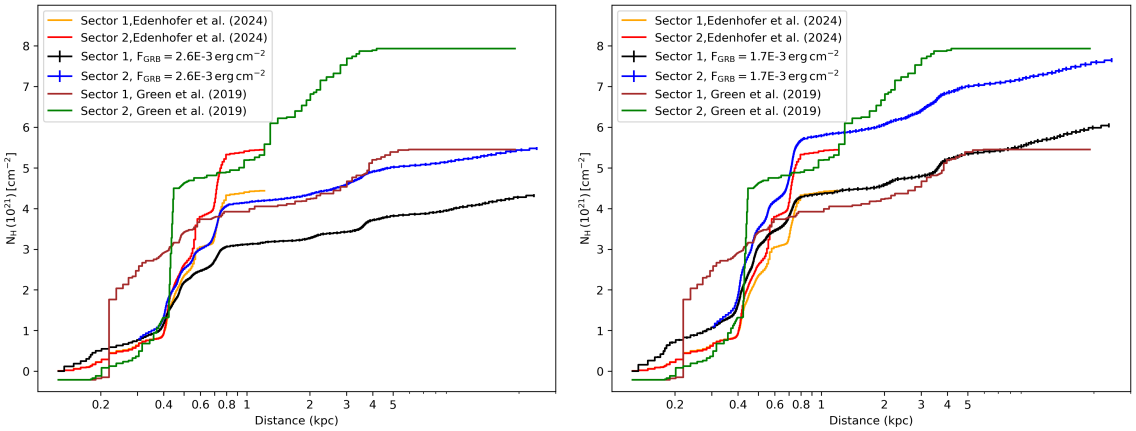

Figure 3.11: Cumulative hydrogen column densities obtained from X-ray dust scattering for Sector 1 (black) and for Sector 2 (blue), calculated using either the best-fit fluence from Tiengo et al. (2023) (left panel) or a factor 1.35 smaller fluence (right panel). In both cases the same dust distribution for distances <300 pc were assumed for the two sectors. Both panels also show a comparison with the cumulative hydrogen column density derived from Green et al. (2019) (brown for Sector 1 and green for Sector 2) and from Edenhofer et al. (2024) (orange for Sector 1 and red for Sector 2). A conversion factor between $N_{\rm H}$ and $A_{\rm v}$ equal to $1.9 \times 10^{21} {\rm cm}^{-2}\,{\rm mag}^{-1}$ was used.

(2023) from the analysis of the afterglow X-ray spectrum, $N_{\rm H,z=0.151} = (1.4 \pm 0.4) \times 10^{22}\,{\rm cm}^{-2}$. This difference can be explained by the smaller value assumed by Williams et al. (2023) for the Galactic absorption ($N_{\rm H,Gal} = 5.38 \times 10^{21}\,{\rm cm}^{-2}$), derived from a $N_{\rm H}$ map with poor angular resolution (Willingale et al., 2013). As already noted in Tiengo et al. (2023), the $N_{\rm H}$ inferred from *Planck* data ($N_{\rm H,Gal} \simeq 9 \times 10^{21}\,{\rm cm}^{-2}$; Planck Collaboration et al. 2014) indicates a significantly greater absorption in our Galaxy at the afterglow position.

In the analysis of the multi-wavelength afterglow reported by Kann et al. (2023), the impact of multiple values for the Galactic extinction, ranging from 0 to $A_{\rm v} = 5.2$ mag (corresponding to no additional extinction in the host galaxy), was explored. Fulton et al. (2023) determined that in order to align the optical and X-ray fluxes observed 1-2 days after the burst, an additional extinction of $A_{\rm v} = 1.5$ mag ($N_{\rm H} = 2.85 \times 10^{21} {\rm cm}^{-2}$ using a conversion factor $N_{\rm H}/A_{\rm v} = 1.9 \times 10^{21} {\rm cm}^{-2}\,{\rm mag}^{-1}$; Tiengo et al. 2023) is required. This excess is likely due to the contribution of the ISM in the host galaxy and it is only slightly smaller than our estimate, which corresponds to $N_{\rm H} = (3.5 \pm 0.3) \times 10^{21} {\rm cm}^{-2}$, if the correction due to the host galaxy redshift is not applied. Actually, Fulton et al. (2023) observed that this additional extinction decreased to 1.0 mag and 0.8 mag 2-3 days and 4-5 days after the GRB, respectively. The slightly larger X-ray absorption that we derive from the spectral analysis of the dust-scattered prompt GRB emission might therefore be part of this decreasing trend. A similar variability with time has been observed in other GRBs, such as GRB 190114C, and attributed to the photo-ionization of the surrounding ISM (Campana et al., 2021).

The best estimate of the X-ray fluence of GRB 221009A in the soft X-ray range

given in Tiengo et al. (2023) ($2.6 \times 10^{-3}\,\mathrm{erg\,cm^{-2}}$) is approximately an order of magnitude larger than the value obtained by extrapolating to the same energy range the GRB spectrum observed at higher energies (Frederiks et al., 2023; An et al., 2023; Burns et al., 2023). This estimate was derived by assuming in the spectral model of ring 6 the amount of dust in the cloud at 0.73 kpc as determined by Lallement et al. (2022), which, as discussed in Sect. 3.9, lacks adequate angular resolution. Decreasing the fluence by a factor 1.9 or 1.35, as suggested by the spatially-resolved analysis reported in Sect. 3.3.4 and 3.4.3, respectively, would only partially reduce the magnitude of the soft excess found in Tiengo et al. (2023), which would still be a few times brighter than the extrapolation of the prompt GRB emission estimated from hard X-ray data.

The sector analysis reported here and the adoption of different extinction maps allow us to better control systematic effects, but our results are still based on a single dust model (BARE-GR-B) and a specific relation between hydrogen column density and optical extinction ($N_\mathrm{H} = 1.9 \times 10^{21}\,A_\mathrm{v}\,\mathrm{cm^{-2}\,mag^{-1}}$; Tiengo et al. 2023). Even if the BARE-GR-B model is the best one describing the dust responsible for the X-ray rings observed around GRB 221009A, Tiengo et al. (2023) have shown that other dust models provide similarly good fits to the ring spectra (e.g., COMP-GR-B from Zubko et al. 2004 or the Draine 2003 model). In these cases, we obtain a GRB fluence that can be different by up to a factor 1.5. Additionally, the $N_\mathrm{H}/A_\mathrm{v}$ relationship is also subject to systematic uncertainties, as demonstrated by the scatter in previous measurements across various sky regions and astrophysical objects, which range from 1.0×10^{21} to $2.8 \times 10^{21}\,\mathrm{cm^{-2}\,mag^{-1}}$ (Zhu et al., 2017). Finally, although the spatially-resolved spectral analysis of the X-ray rings reported in Sect. 3.3.1 suggests that all the dust clouds are formed by dust grains with the same properties, we cannot exclude the existence of different dust populations depending on the local environment.

3.5 Conclusion

We presented a detailed analysis of the dust-scattered X-ray emission from GRB 221009A observed by *XMM-Newton* and *Swift*/XRT. The main aim of this analysis, supported by the comparison with recently published 3D extinction maps, was to constrain the properties of the ISM in the GRB direction both in our Galaxy and in the host galaxy. In particular, we generated a 3D map of the Galactic dust distribution in a $\sim$0.5° wide region centered at the position of the GRB with a better resolution than previous studies, both in the plane of the sky (few arcminutes) and along the radial direction (approximately 1 pc for distances $D < 1$ kpc and 100 pc for $D > 10$ kpc). Although this map covers a very small sky region, the dust cloud distances are directly measured throughout the whole Galaxy using a geometrical method, in analogy with parallaxes for stars, and can therefore be used to calibrate other maps based on indirect or model-dependent distance measurements.

In addition, the spectral analysis of the brightest X-ray rings revealed considerable variability in the hydrogen column density of the total absorbing matter across the FOV, which, coupled to the correlated intensity variability of the dust-scattered radiation, allowed us to separate Galactic absorption from the host galaxy

contribution. Such measurement is crucial not only to characterize the GRB local environment and its time evolution induced by the burst radiation, but also to constrain the intrinsic luminosity of a possibly associated supernova (see, e.g., Shrestha et al. 2023).

Finally, this work refined the soft X-ray fluence estimate from Tiengo et al. (2023) ($2.6 \times 10^{-3}\,\mathrm{erg\,cm^{-2}}$), reducing it by a factor of at least 1.35. However, the revised values, based on the comparison of our modeling of the dust-scattering rings with three different 3D extinction maps, are not small enough to eliminate the soft excess in the prompt X-ray emission found in the previous work.

Chapter 4

Accurate distances of the Galactic spiral arms from dust-scattered X-ray emission of gamma-ray bursts

4.1 Introduction

Despite extensive studies throughout the last century, the exact spiral structure of the Milky Way is not yet well defined (see 4.7). The Galactic structure is reconstructed on the basis of different tracers, whose distance is often affected by large uncertainties arising from kinematic distance ambiguities and the dependence on a Galactic rotation curve model. A promising complementary approach is provided by studies of X-ray dust scattering rings (see Sect. 2.1), which allow a purely geometric determination of the distances to interstellar clouds along the line of sight.

To constrain the structure of our Galaxy, particularly focusing on the most distant arms, we identified three low-latitude ($|b| < 5°$) GRBs around which X-ray scattering rings were detected by *XMM-Newton* or *Chandra*: GRB 221009A ($l \simeq 53°$, $b \simeq 4°$; Tiengo et al. 2023; Williams et al. 2023), GRB 160623A ($l \simeq 84°$, $b \simeq -3°$; Pintore et al. 2017), and GRB 031203 ($l \simeq 255°$, $b \simeq -5°$; Vaughan et al. 2004; Tiengo and Mereghetti 2006; Feng and Fox 2010). These measurements can be used to constrain the structure of the Perseus, Outer, and Outer Scutum-Centaurus (OSC) arms.

This Chapter is structured as follows: Section 4.2 describes the data reduction process, Section 4.3 explains the analysis methodology and reports the results, which are discussed in Section 4.4, and Section 4.5 presents the conclusions.

4.2 Observations and data reduction

In this work, we report the analysis of X-ray data collected by the *XMM-Newton* (Jansen et al., 2001) and *Chandra* (Weisskopf et al., 2000) missions (Obs IDs in Table 4.1). The study of X-ray expanding rings requires a detailed characterization of the spatial distribution of the background signal (i.e. the instrumental and diffuse X-ray contribution unrelated to the source), which was obtained either through the

Table 4.1: Log of the *Chandra* and *XMM-Newton* observations of the GRBs.

Satellite/instrument	Observation ID	Start time (UTC)	Stop time (UTC)	Exp. time
GRB 221009A:				
XMM-Newton/pn	0913991601 (Obs2)	2022-10-14T05:41:21	2022-10-14T22:52:21	34.0 ks
Chandra/ACIS	27517	2022-10-17T16:53:32	2022-10-17T23:36:58	21.7 ks
XMM-Newton/pn	0913991701 (Obs3)	2022-10-30T04:56:37	2022-10-30T21:48:17	34.0 ks
XMM-Newton/pn	0913991801 (Obs4)	2022-11-01T07:21:37	2022-11-01T21:39:57	35.0 ks
XMM-Newton/pn	0913991901 (Obs5)	2022-11-10T16:09:14	2022-11-11T21:00:54	87.8 ks
GRB 160623A:				
XMM-Newton/pn	0781100201	2016-06-24T20:23:46	2016-06-25T12:53:46	50.0 ks
XMM-Newton/MOS	”	”	”	55.0 ks
GRB 031203:				
XMM-Newton/pn	0158160201	2003-12-04T04:09:29	2003-12-04T20:19:40	56.0 ks
XMM-Newton/MOS	”	”	”	56.0 ks
XMM-Newton/pn	0163360201	2003-12-06T18:11:07	2003-12-07T09:21:17	37.0 ks
XMM-Newton/MOS	”	”	”	35.0 ks
Chandra/ACIS	05298	2004-01-22T21:17:36	2004-01-23T03:44:30	21.5 ks

use of archival observations or counts from the same observation but in a different energy band.

For the *XMM-Newton* observations, we analyzed data from the EPIC pn camera (Strüder et al., 2001) and the two EPIC Metal-Oxide Semiconductor (MOS; Turner et al. 2001) cameras. These data were processed using the Science Analysis Software (SAS) 20.0.0 (Gabriel et al., 2004) and the latest calibration files. The EPIC events were cleaned with standard filtering expressions[1]. Point-like sources, identified through the SAS source detection task `emldetect`, were excluded by masking circular regions, each with a radius of 25″ (except for particularly bright sources where the radius was set to 40″). For most *XMM-Newton* observations, the pn background was extracted over a broad energy range of 0.5-15 keV. We excluded two intervals: the band containing significant ring emission (0.7-4 keV for GRB 221009A and GRB 160623A, and 0.8-2.2 keV for GRB 031203), and the 7.3-9.3 keV region. The latter contains fluorescence features from the detectors and their surrounding structure, whose intensity is not uniform across the pn camera[2]. For the MOS cameras, we adopted a similar strategy, extracting the background from the 4-12 keV range. Before subtraction, the background extracted from an energy range where no dust-scattering emission is observed must be rescaled by the ratio of the number of counts detected in the source and background energy ranges in a spatial region where no dust-scattering signal is expected at any energy.

The *Chandra* data reduction was performed with the Chandra Interactive Analysis of Observations (`CIAO v4.15`, Fruscione et al. 2006) software and the calibration data files `CALDB(v4.10.2)`. In order to reprocess the data, the chandra_repro script was used, while the blank-sky script automatically selected the appropriate blank-sky background files in each observation. Point-like sources were identified using the wavdetect tool and excluded from the analysis.

[1]For pn data: #`XMMEA_EP`&&`(FLAG==0)`&&`(PATTERN<=4)` and for MOS: #`XMMEA_EM`&&`(PATTERN<=12)`.

[2]This band contains the emission lines corresponding to $Cu-K\alpha$, $Ni-K\alpha$, and $Zn-K\alpha$.

4.2.1 GRB 221009A

GRB 221009A was initially reported by the Burst Alert Telescope (BAT) aboard the *Swift Neil Gehrels Observatory* on October 9, 2022, at 14:10:17 UT (Dichiara et al., 2022). However, the GRB started about an hour before as observed for example by the *Fermi* Gamma-ray Burst Monitor (GBM; Lesage et al. 2023) . This GRB is the brightest ever recorded and occurred near the direction of the Galactic plane, producing multiple X-ray dust scattering rings later observed by the X-ray Telescope (XRT) on Swift (Williams et al., 2023; Vasilopoulos et al., 2023; Vaia et al., 2025), as well as by *XMM-Newton* (Tiengo et al., 2023; Vaia et al., 2025), the *Imaging X-ray Polarimetry Explorer* (IXPE) (Negro et al., 2023), and *Chandra*. For this study, we shall focus on data from *XMM-Newton* and *Chandra*, which are more sensitive to the relatively small and faint rings produced by distant dust.

XMM-Newton observations

XMM-Newton observed GRB 221009A on five occasions from October 11 to November 11 2022. To minimize pile-up during the first observation, the pn and the two MOS cameras were operated in Timing mode, using the thick optical-blocking filter. In Timing mode, only the peripheral CCDs of the MOS cameras provide full imaging capabilities, covering a region from approximately $5'$ to $15'$ from the target position. As a result, only the rings produced by clouds at distances smaller than 1.6 kpc (see equation 2.2) are visible in this observation (Tiengo et al., 2023; Vaia et al., 2025). This data set is not used in this work, as we focus on clouds at distances greater than 5 kpc. The log of all the observations analysed in this work is reported in Table 4.1.

As a background for Obs2, we selected, for both cameras, data from the observation of the bright high-redshift quasar RBS 315 conducted in January 2013 (Observation ID: 0690900201). As in Vaia et al. (2025), this observation was chosen due to the similarities of the central source with the GRB 221009A X-ray afterglow and because it occurred during a similar phase of the Solar Cycle, ensuring comparable contamination from the unfocused particle background (Gastaldello et al., 2022). We adopted this strategy for the background to subtract the contribution from the X-ray background, as well as from the GRB afterglow and its possible dust-scattering halo. The approach outlined at the beginning of Section 4.2 was instead applied to the remaining three *XMM-Newton* observations. To maximize the signal-to-noise ratio of the rings, the analysis was confined to the 0.7–4 keV energy band, as in Tiengo et al. (2023) and Vaia et al. (2025).

Chandra observation

The *Chandra* telescope started observing GRB 221009A on October 17, 2022 at 16:53:32 UT with an exposure time of 21.7 ks (Table 4.1). The data were acquired using the ACIS-I instrument in FAINT mode. As shown in Fig.4.1, the rings are not fully covered and only a portion of them is visible since the observation was performed off-axis. This strategy was chosen to exclude the afterglow emission and allow the detection of the largest rings.

No significant background flares were detected and so the full exposure could be analysed. As an alternative to blank-sky background files, we also selected events from the same observation, but in a hard energy band (4-10 keV), where no signal from X-ray dust-scattering is expected. To maximize the signal-to-noise ratio of the scattered X-ray rings, the analysis was restricted to the 0.7–4 keV energy band as for the *XMM-Newton* data.

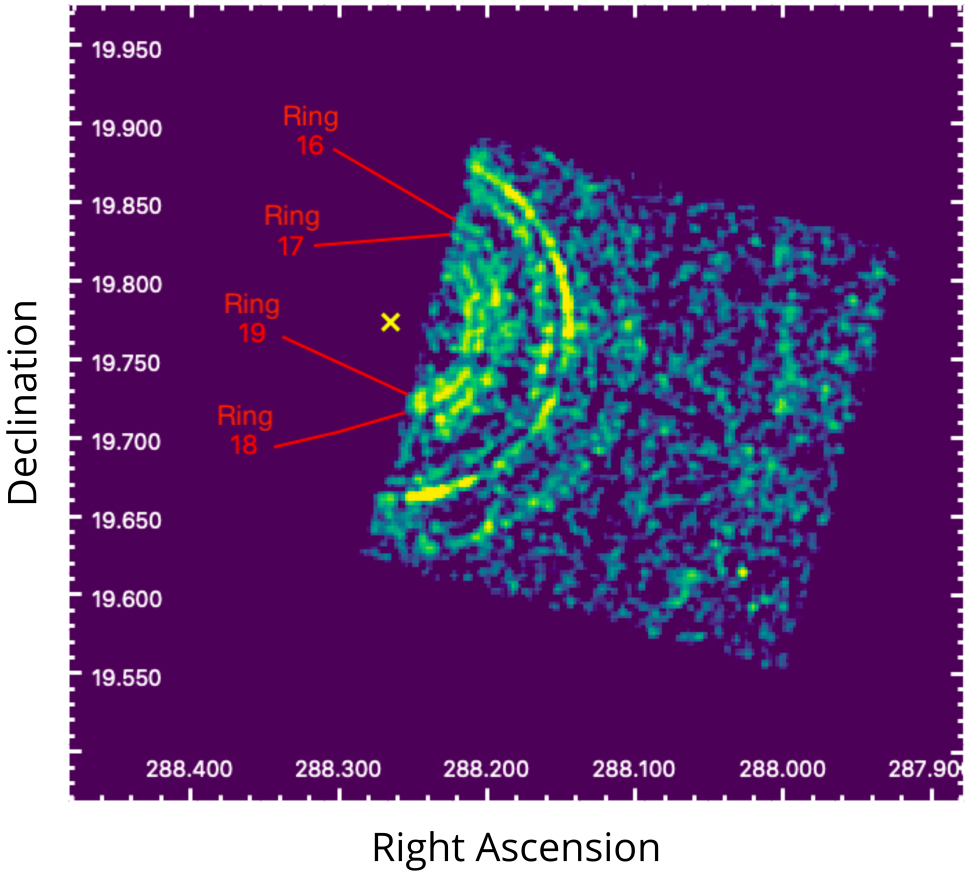

Figure 4.1: 0.7–4 keV ACIS-I *Chandra* image of GRB 221009A. The image is smoothed with a Gaussian kernel of $\sigma = 1''$ and the point sources are excluded. The yellow cross marks the position of the GRB afterglow. The red labels indicate the positions of the rings 16, 17, 18, and 19 produced by clouds at approximately 8, 10, 14 and 19 kpc, respectively.

4.2.2 GRB 160623A

GRB 160623A was detected by the Fermi/GBM instrument on June 23, 2016, at 05:00:34.23 UT. This burst was also observed above 1 GeV by Fermi/LAT (Vianello and Longo, 2016) and detected by Konus-Wind (Frederiks et al., 2016). Approximately 40 ks after the burst, Swift/XRT performed its first observation of the GRB afterglow, revealing a dust-scattering ring with a radius of about $3.5'$ (Tiengo et al., 2016), attributed to a dust cloud located at approximately 800 pc (see Eq. 2.2). In a subsequent *XMM-Newton* observation six X-ray dust-scattering rings were identified

(Pintore et al., 2017).

XMM-Newton observation

The *XMM-Newton* satellite started observing GRB 160623A approximately two days later on June 24, 2016 at 20:23:46 UT, employing all EPIC cameras in full-frame mode for a duration of 16 hours (Table 4.1). No more *XMM-Newton* or *Chandra*, observations of this field are available.

4.2.3 GRB 031203

On December 3, 2003, at 22:01:28 UT, GRB 031203 was identified by the Imager aboard the INTEGRAL satellite (IBIS; Gotz et al. 2003). This GRB had a single peak with a duration of 30 s and a peak flux of $1.3 \times 10^{-7} \mathrm{erg\,s^{-1}\,cm^{-2}}$ in the $20 - 200$ keV energy range. At the time of the burst, the *Swift* satellite was not yet operational. The *XMM-Newton* observatory responded immediately, while *Chandra* performed its first observations more than a month after the burst.

XMM-Newton observations

A 58 ks observation of the GRB 031203 field with *XMM-Newton* started about six hours after the burst, on December 4, 2003, at 04:09:29 UT (Table 4.1). The *XMM-Newton* satellite captured the GRB on-axis, utilizing all EPIC cameras in full-frame mode.

On December 6, 2003, GRB 031203 was serendipitously observed at an off-axis angle of $\sim 10'$ during a Zeta Puppis pointing (Table 4.1). Following Eq. 2.2, the radius of the ring detected by Feng and Fox (2010), which was generated by a cloud at a distance of 9.9 kpc, is expected to be $\sim 2.4'$ after three days, remaining fully within the Field of View of all three instruments. To maximize the signal-to-noise ratio of the rings, the analysis was confined to the 0.8–2.2 keV energy band, as in Tiengo and Mereghetti (2006).

Chandra observation

The *Chandra* telescope started observing GRB 031203 on January 22, 2004 at 21:17:36 UT with an exposure time of 21.5 ks (Table 4.1). A 30 ks *Chandra* observation taken on April 18, 2004 was not considered because no detectable X-ray rings were expected more than 100 days after the GRB.

The data were acquired using both ACIS-I and ACIS-S chips in VFAINT mode. No significant background flares were detected during the observation. As in the *XMM-Newton* analysis, we focused on the 0.8–2.2 keV energy. The background blank-sky subtraction was performed separately for CCD S4 and for CCDs I2, I3, S2 and S3, due to the different exposure time of CCD S4 blank-sky data. To provide additional background estimates, the original event file was filtered both in the 2.2–5 keV and 4–10 keV high energy bands, where negligible dust-scattered X-ray emission is expected.

4.3 Data analysis and results

In this study, we analyze the X-ray dust-scattering rings of GRB 221009A, GRB 160623A, and GRB 031203, with a particular focus on determining the distances to dust clouds located beyond 5 kpc. For these GRBs, we applied the pseudo-distance distribution method (see Sect. 2.1.4 and Tiengo and Mereghetti 2006).

The data analysis for GRB 221009A, GRB 160623A, and GRB 031203 is detailed in the following subsections.

4.3.1 GRB 221009A

For GRB 221009A, we created histograms of the pseudo-distances for all the observations and their respective backgrounds, but we limited our analysis only to pseudo-distances larger than 6 kpc. To indicate the peaks and the corresponding rings in the X-ray images, we adopted the nomenclature introduced in Tiengo et al. (2023), where Ring 16, 17, 18, and 19 were identified in this distance range.

For *XMM-Newton* observations, we conducted separate analyses of the data collected by the MOS and pn cameras. After verifying that the results were consistent and that the pn camera provided smaller uncertainties, we chose to present only the pn data. For Obs2, the background-subtracted pseudo-distance was fit in the range from 6 to 30 kpc using a model comprising the sum of four Lorentzian functions, resulting in a good fit (p-value = 0.28, see the top-left panel of Fig. 4.2). Each Lorentzian component corresponds to a distinct dust cloud, identified in Tiengo et al. (2023) for this GRB within the distance range fitted. The distances of these peaks correspond to those of the rings from 16 to 19 reported in Tiengo et al. (2023). Similarly, for Obs3 and Obs4, the pn background-subtracted pseudo-distances were adequately fit (p-value = 0.20 for Obs3 and p-value = 0.31 for Obs4) by the sum of three Lorentzian functions, corresponding to Ring 17, 18, and 19 (see Fig. 4.2). To check if Ring 16 could be detected in these observations as well, we attempted a fit over the same distance range using the sum of four Lorentzian functions. Although the model provided good fits in both cases (Fig. 4.2), adding an additional Lorentzian did not improve the results, and the best-fit parameters of the three peaks remained consistent with those obtained from the former.

For Obs5, the data were well fitted with three Lorentzians (Rings 17-19, p-value = 0.22). A four-Lorentzian model was also tested to include Ring 16, but the extra peak's distance and width were unconstrained and thus fixed to Obs2 values. This addition did not improve the fit (p-value = 0.26) and left the other parameters unchanged (Fig. 4.2, bottom-right).

For the *Chandra* observation, we derived the histogram of the pseudo-distances and tested both methods for background subtraction. The blank-sky background was simply rescaled by the ratio of the source and background exposure times, while the background derived from the same observation at high energies was normalized by the ratio of the counts extracted in the 0.7–4 keV and 4–10 keV energy bands from a region free of scattering-ring contamination, corresponding to the 1.3–1.7 kpc distance interval. The background-subtracted data were fit with a model consisting of the sum of four Lorentzian functions over the 6.2–25 kpc distance range. The

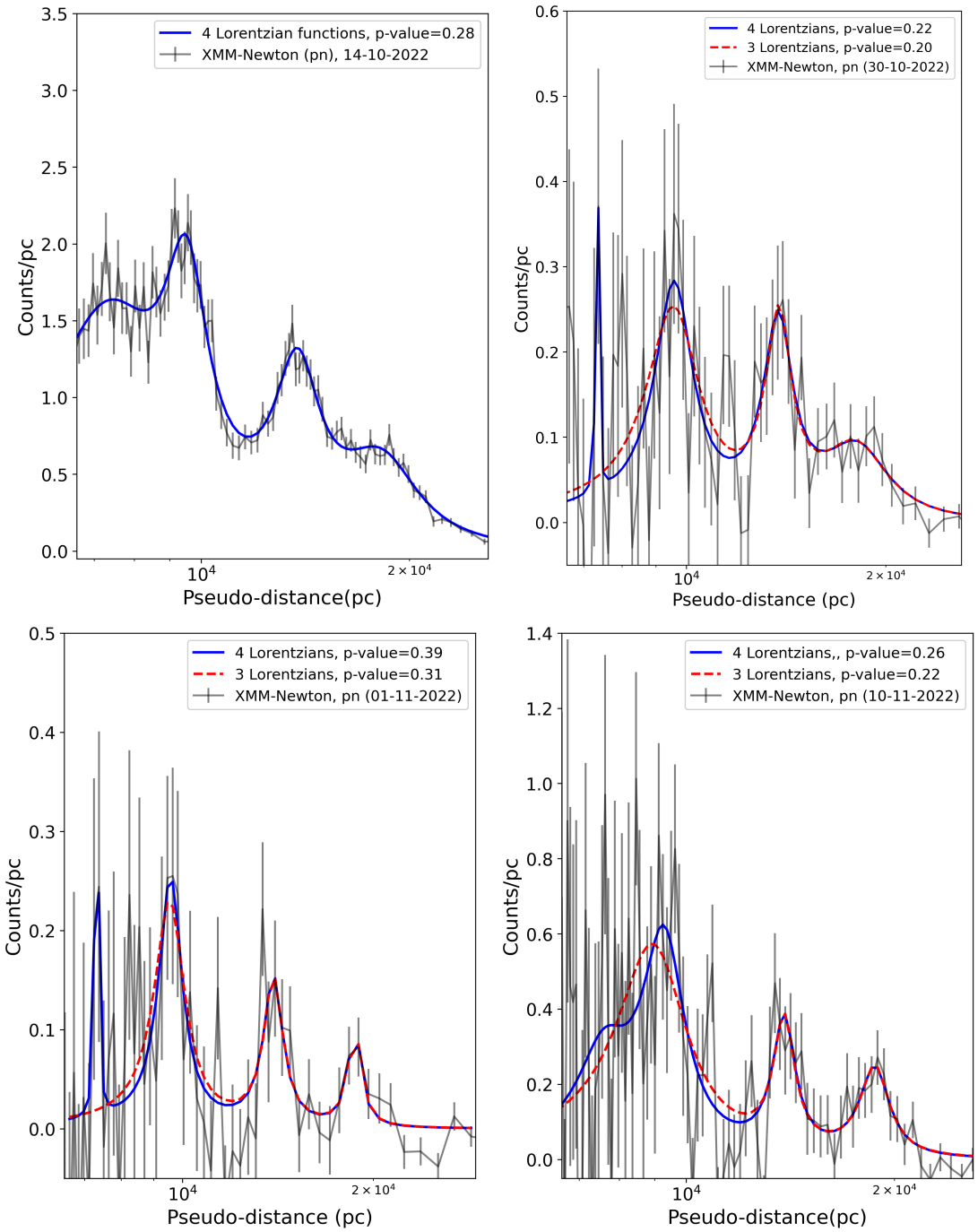

Figure 4.2: Pseudo-distance distributions in the 0.7–4 keV energy band for the GRB 221009A observations performed by *XMM-Newton* on October 14 (Obs2, top-left panel), October 30 (Obs3, top-right panel), November 1 (Obs4, bottom-left panel), and November 10 (Obs5, bottom-right panel). The red dashed and blue solid lines indicate the best-fit models with 3 and 4 Lorentzian functions, respectively.

best-fit results are reported in Tab.4.2.

Since the fit obtained with the blank-sky background subtraction was only marginally acceptable, we also added a fifth Lorentzian function to the model. As can be seen in

Fig.4.3 and Tab.4.2, the additional Lorentzian accounts for a small excess between the first two peaks, with no significant effects on the positions of the four main peaks.

The distances and widths of the dust structures producing Ring 17, 18, and 19 derived from the *XMM-Newton* and *Chandra* observations are shown in Fig. 4.4. A constant fit to the distances obtained from the different observations reproduces the data well, indicating that all the measurements – despite being taken with different instruments and at different epochs – are consistent. Similarly, the widths derived from the three late-time *XMM-Newton* observations agree with each other and with the value found by *Chandra*. The width measured in Obs2 is significantly larger, but this can be explained by the fact that in this earlier observation the rings have smaller radii and the peak width is strongly affected by the instrumental point-spread function. The consistency among the other four observations demonstrates that the measured width corresponds to the intrinsic size of the dust cloud and is not dominated by the instrumental spatial resolution.

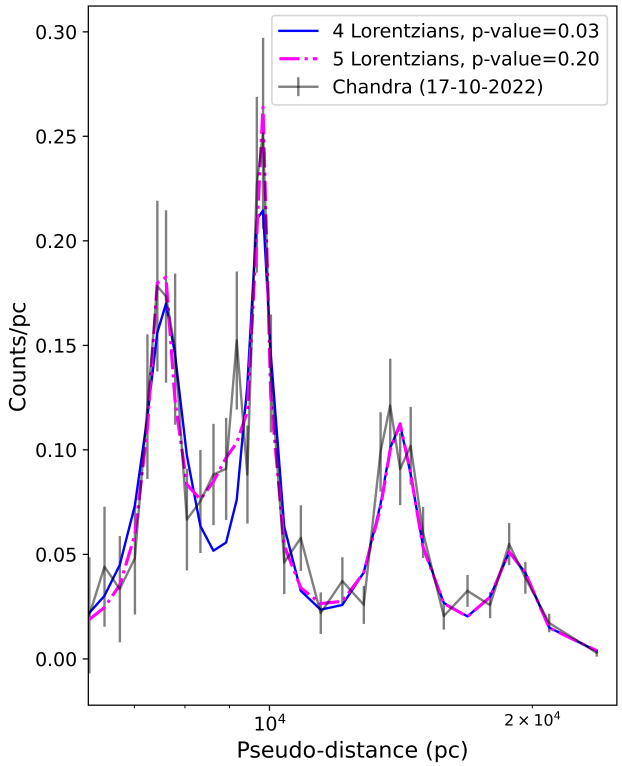

Figure 4.3: Pseudo-distance distribution in the 0.7–4 keV energy band for the GRB 221009A *Chandra* observation. The background was subtracted from blank-sky observations. The red line indicates the best-fit model with four Lorentzian functions, while the blue line represents the best-fit model with five Lorentzian functions.

Table 4.2: Best-fit parameters of the pseudo-distance distribution in the 0.7–4 keV energy band for the GRB 221009A *Chandra* observation. Two background-subtraction methods (blank-sky or 4–10 keV background) and two models (4 or 5 Lorentzians) were adopted.

	Ring 16	Ring 17	Ring 18	Ring 19
Blank-Sky (4 Lorentzians)				
D [kpc]	7.58 ± 0.07	9.76 ± 0.05	14.0 ± 0.1	19.0 ± 0.2
Width [kpc]	0.5 ± 0.1	0.36 ± 0.07	0.9 ± 0.1	1.1 ± 0.3
Counts	124	119	145	86
χ^2/d.o.f.		36.62/22		
p-value		0.026		
4–10 keV background (4 Lorentzians)				
D [kpc]	7.66 ± 0.08	9.75 ± 0.05	13.9 ± 0.1	19.0 ± 0.2
Width [kpc]	0.4 ± 0.1	0.33 ± 0.07	0.8 ± 0.1	1.1 ± 0.3
Counts	93	106	129	76
χ^2/d.o.f.		28.65/22		
p-value		0.155		
Blank-Sky (5 Lorentzians)				
D [kpc]	7.53 ± 0.06	9.1 ± 0.4 9.80 ± 0.04	14.1 ± 0.1	19.0 ± 0.2
Width [kpc]	0.3 ± 0.1	1.0 ± 0.4 0.16 ± 0.07	0.8 ± 0.1	1.1 ± 0.3
Counts	77	129 56	139	85
χ^2/d.o.f		23.89/19		
p-value		0.200		

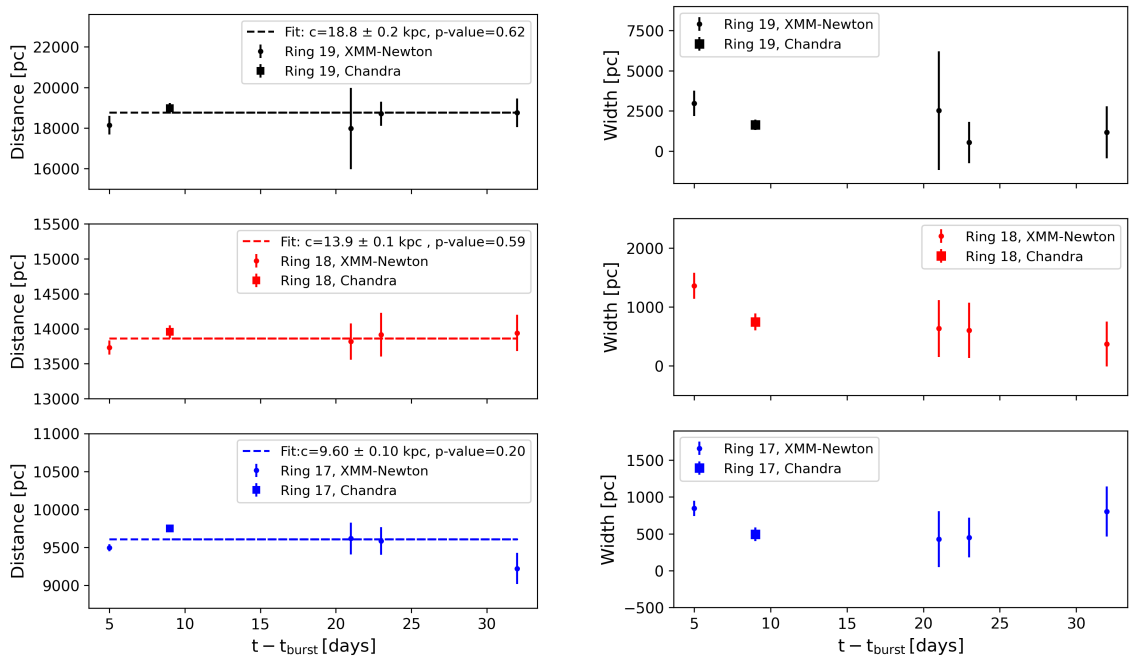

Figure 4.4: Distances (left panels) and widths (right panels) of Ring 19 (upper panels), Ring 18 (central panels), and Ring 17 (bottom panels) determined from the *XMM-Newton* (circles) and *Chandra* (squares) observations of GRB 221009A. The dashed line represents the best-fit with a constant.

4.3.2 GRB 160623A

The X-ray dust scattering rings around GRB 160623A were previously studied by Pintore et al. (2017), who identified six dust scattering rings, including one at a distance greater than 5 kpc, specifically at 5079 ± 64 pc. In Pintore et al. (2017), the pseudo-distance method was also used to analyze the rings; however, in that case, the background was phenomenologically fit with the sum of two power-law functions, whereas in our analysis, we subtracted the background before fitting. For this GRB, after having verified the consistency of data from all three cameras[3], we combined all data to minimize uncertainties. We then derived the pseudo-distance distribution from all cameras for both the observation and the background (obtained as described in Section 4.2). The two distributions were subtracted, with normalization applied in a region free from X-ray dust scattering contamination, following the same approach as for GRB 221009A (in this case, the distance interval was 2–3 kpc). From the background-subtracted pseudo-distance distribution at distances greater than 5 kpc, we confirm the peak previously identified by Pintore et al. (2017) at $D_1 = 5125 \pm 29$ pc ($\sigma_1 = 410 \pm 47$ pc). Additionally, we detected two more peaks at distances $D_2 = 6909 \pm 56$ pc and $D_3 = 9908 \pm 624$ pc, with widths of $\sigma_2 = 299 \pm 91$ pc and $\sigma_3 = 1027 \pm 190$ pc, respectively.

[3]We also included data from the MOS1 camera despite the damage sustained by two of its external CCDs early in the mission, as we are only interested in features at distances greater than 5 kpc, corresponding to angles smaller than $\simeq 3'$, which are fully covered by the central chip.

When modeling the data with the sum of only two Lorentzian functions, centered at D_1 and D_2, we obtain a p-value of 0.001, whereas a model incorporating three Lorentzian functions yields a p-value of 0.19 (see Figure 4.5).

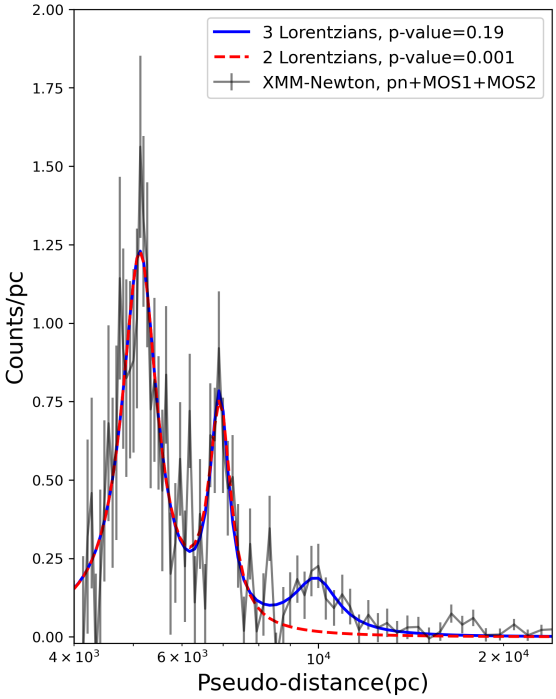

Figure 4.5: Pseudo-distance distributions in the 0.7–4 keV energy band for the GRB 160623A *XMM-Newton* observations of June 24 between 4 and 20 kpc. The blue solid line indicates the best-fit model with 3 Lorentzian functions. The red dashed line indicates the best-fit model with 2 Lorentzian functions.

4.3.3 GRB 031203

The X-ray dust scattering rings around GRB 031203 have been extensively studied over the years. Vaughan et al. (2004) identified two dust scattering rings at distances of less than 2 kpc, a finding later confirmed by Tiengo and Mereghetti (2006) using the pseudo-distance method. A subsequent analysis of the same data by Feng and Fox (2010) reported the discovery of a third ring at a distance 9.94 ± 0.39 kpc.

In this work, we reanalyze the first *XMM-Newton* observation and, for the first time, apply the pseudo-distance distribution method to both the *Chandra* data and the second *XMM-Newton* observation of this GRB. For *XMM-Newton*, after confirming consistency across all three cameras – following a procedure similar to that used for GRB 160623A – we combined the data of each observation to reduce statistical uncertainties. We then derived the pseudo-distance distributions for both observations and subtracted their corresponding backgrounds (as described in Section 4.2). The background distributions were normalized in a region free from X-ray dust scattering contamination, specifically between 4 and 7 kpc, in line with the method used for GRB 221009A and GRB 160623A. By fitting the background-subtracted

pseudo-distance distribution of the first observation in the 4–25 kpc range, we confirmed the presence of the peak identified, with a different method, by Feng and Fox (2010). Our analysis yielded a dust cloud distance of 9.9 ± 0.4 kpc and a width of $\sigma = 1.5 \pm 0.6$ kpc, with a fit p-value of 0.30 (see upper panel Figure 4.6). The same peak is also visible in the second *XMM-Newton* observation, though with a lower significance. Fitting its background-subtracted pseudo-distance distribution, we found a peak at 8.7 ± 0.8 kpc with a width of $\sigma = 1.2 \pm 0.7$ kpc. This fit returned a p-value of 0.05, while a fit using a constant model resulted in a much lower p-value of 0.0005 (see the bottom panel of Figure 4.6). The weighted average of these two measurements provides a distance of 9.7 ± 0.4 kpc.

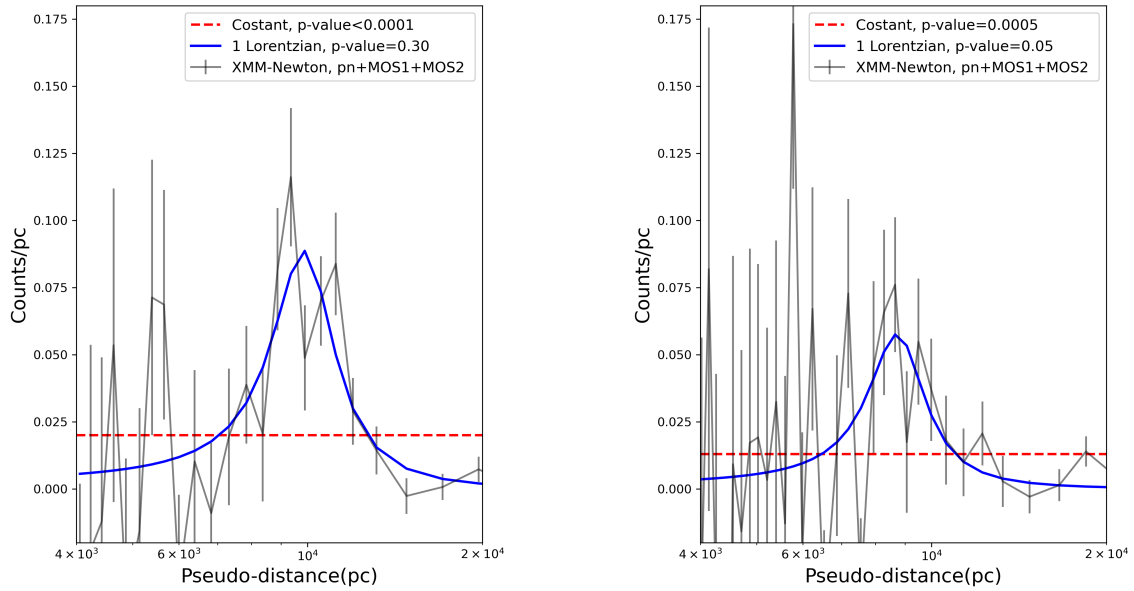

Figure 4.6: Pseudo-distance distributions in the 0.8–2.2 keV band for the *XMM-Newton* observations of GRB 031203 on December 4 (left panel) and December 6 (right panel). The blue solid line shows the best-fit with a Lorentzian function, and the red dashed line the best-fit with a constant.

For the *Chandra* observation, we derived histograms of the pseudo-distances both subtracting blank-sky and high-energy backgrounds, but no significant dust-scattered emission was detected. In the latter case, the background pseudo-distance values were normalized by the ratio of the total counts in the 0.8–2.2 keV band to those in the 2.2–5 keV range, extracted from a region free of scattering ring contamination (corresponding to distances in the 12–15 kpc interval). The fit of the background-subtracted distribution with a constant was perfectly consistent with no signal in the 3.5–20 kpc distance range ($y = -0.007 \pm 0.004$, $\chi^2/dof = 27.43/35$, p-value = 0.82).

4.4 Discussion

By analyzing the expanding X-ray scattering rings of GRB 221009A, GRB 160623A, and GRB 031203, we have been able to map the outer structure of the Milky Way

with an unprecedented level of precision. Unlike the most commonly used methods that rely on kinematic models, the dust scattering rings provide a direct geometric measurement of the distance to dust clouds along the line of sight. Owing to the good angular resolution of our X-ray data, we can measure not only the distance but also the spatial thickness of the spiral arms, as the shape of the peaks in the pseudo-distance distributions reflects the radial distribution of dust within each arm.

In Fig. 4.7, we overlaid the 3 directions sampled by the selected GRBs on the Milky Way picture reported in Sun et al. (2024). As indicated by the red dots, our analysis allows us to probe the structure of the Perseus, Outer, and OSC arms.

Perseus Arm

As shown in Fig. 4.7, the directions of the 3 GRBs cross the Perseus Arm. GRB 031203 is located very close to the end of this spiral arm, and no X-ray ring at the corresponding distance has been detected. This result indicates that a negligible amount of dust content is present in the Perseus Arm in the GRB direction ($l = 256°$, $b = -5°$).

Dust scattering rings can instead be associated to the Perseus Arm in the X-ray observations of GRB 221009A and GRB 160623A, allowing us to accurately measure its distance towards their directions: 9.6 ± 0.1 and 5.12 ± 0.03 kpc, respectively. Both these independent measurements are fully consistent with a symmetric inner-Galaxy spiral structure (Vallée, 2008), as shown by the black dashed lines in Fig. 4.7. The detection of significant amounts of dust at the Galactic longitudes of GRB 221009A ($l = 53°$) and GRB 160623A ($l = 84°$) is particularly interesting because they are close to the edges of the Perseus Arm Gap, which is a $\sim$6 kpc section of the spiral arm with a reduced massive star formation activity (Zhang et al., 2013; Sakai et al., 2022).

Outer Arm

The Outer Arm is the only spiral arm that could be mapped in all three directions. The detection of a significant excess in the pseudo-distance distributions derived from two different *XMM-Newton* observations of GRB 031203 with distance and width consistent with those expected for the Outer Arm in this direction, allows us to confirm that this spiral arm extends up to $l = 256°$ and $b = -5°$.

The distances measured for Ring 18 in GRB 221009A (13.9 ± 0.1 kpc) and for the smallest newly discovered ring in GRB 160623A (9.9 ± 0.6 kpc) exceed those predicted by the model in Fig. 4.7. This suggests that the rotation curve used by Sun et al. (2024) to derive the Milky Way structure underestimates the distance of the Outer Arm in this direction.

Outer Scutum-Centaurus Arm

The OSC arm was clearly detected only in the direction of GRB 221009A, positioning the arm farther than both models shown in Fig. 4.7: the dashed white line is the extrapolation of the symmetrical spiral structure by Vallée (2008) and the solid

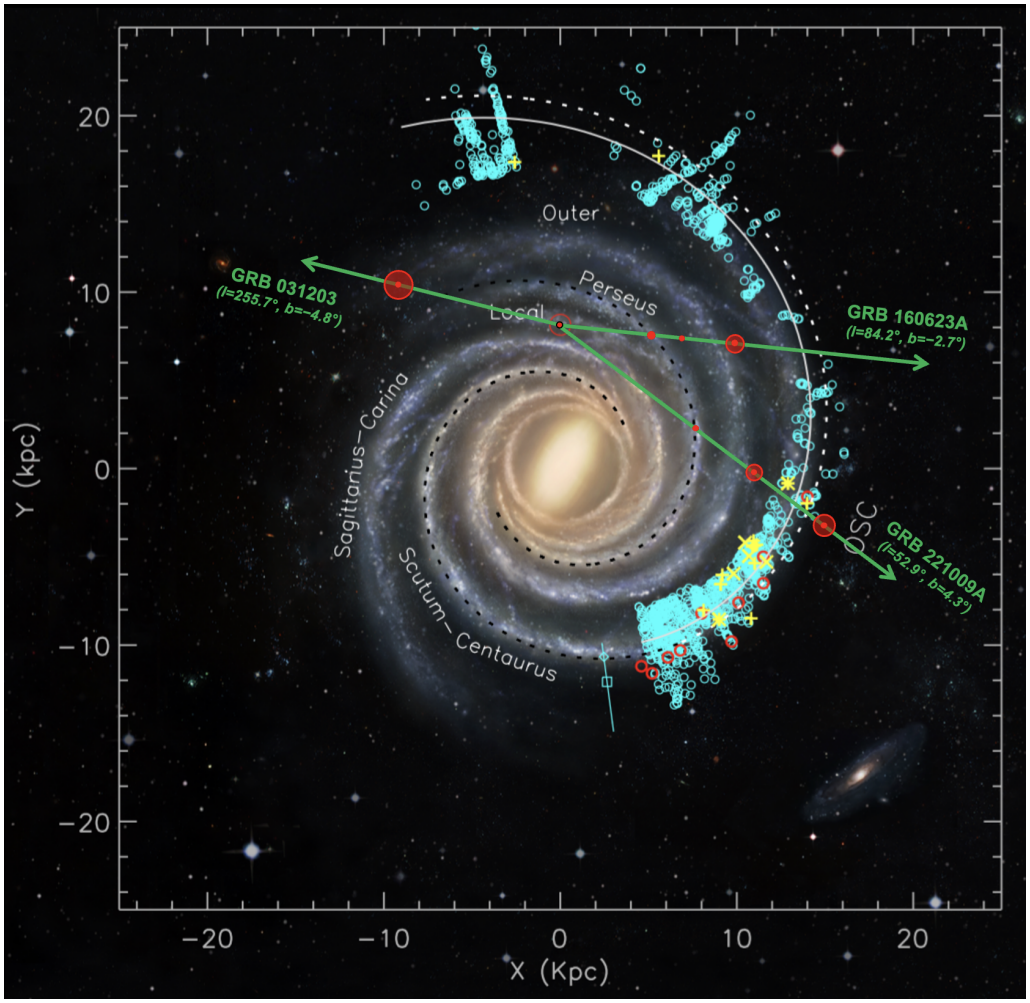

Figure 4.7: Spiral structure of the Milky Way, adapted from Sun et al. (2024). The background map shows the distribution of molecular clouds (MCs) and high-mass star-forming regions (HMSFRs). Cyan and red circles indicate 1306 MCs from Sun et al. (2024) and 10 MCs from Dame and Thaddeus (2011), respectively. The black dashed lines represent the symmetrical Scutum - Centaurus and Perseus arms. The cyan square with error bar marks the only directly measured trigonometric parallax for the OSC arm (Sanna et al., 2017), while the diamond represents the kinematically derived location of the same HMSFR. Yellow pluses and crosses indicate distant H II regions and star-forming masers, respectively. Our measured distances are overlaid as red dots, showing the positions and the widths (surrounding red circles) of the spiral arms as determined from X-ray scattering rings of GRB 221009A (Rings 17, 18, and 19), GRB 160623A, and GRB 031203. The directions of these three GRBs are highlighted in green.

white line is derived from the analysis of a selection of molecular clouds (Sun et al., 2024).

The other distance measurements of individual objects reported in Fig. 4.7 are spread over a relatively wide distance range and are affected by large uncertainties. The choice of a specific rotation curve (Reid et al. 2019 in this case) leads to an un-

derestimation of all distances derived from kinematic methods. On the other hand, the most robust distance measurement previously reported for this arm ($20.4^{+2.8}_{-2.2}$ kpc; Sanna et al. 2017), based on the parallax of a water maser source at small Galactic longitude (cyan square with error bar in Fig. 4.7), has an order of magnitude larger uncertainty than our measurement (19.0 ± 0.2 kpc from *Chandra* data). Moreover, the peak width of ∼2 kpc reflects the radial extent of dust along the line of sight, supporting the interpretation that it traces the arm's thickness rather than a single localized cloud.

The detection of a peak at 19 kpc in the pseudo-distance distribution might be surprising even for an exceptionally bright event such as GRB 221009A, since its latitude of 4.3°implies the presence of a significant amount of dust 1.4 kpc above the Galactic plane. However, this part of the OSC Arm is significantly inclined, with an average latitude of $\sim 3°$ and a width $> 2°$ at the longitude of GRB 221009A (Dame and Thaddeus, 2011). Therefore, the non-detection of a similar structure in the direction of GRB 160623A is justified not only by the lower fluence of this GRB, but also by its negative latitude ($b = -2.7°$).

Comparison with H I/CO Data and Kinematic Models

H I and CO emission can trace the large-scale structure of spiral arms across the Galaxy, but their interpretation relies on Galactic kinematic models, introducing systematic uncertainties at large distances. Figure 4.8 presents a direct comparison of our distance measurements (blue solid lines) for the directions of GRB 221009A and GRB 160623A with H I data from the EBHIS survey (Winkel, B. et al., 2016), which covers the entire northern sky. For GRB 031203 direction, located in the southern hemisphere, a similar comparison is made using H I data from the GASS survey (HI4PI Collaboration: et al., 2016). The H I data are extracted from a $15'$ circular region around the GRB directions for GRB 221009A and GRB 160623A, and a $30'$ region for GRB 031203.

The local standard of rest velocities of the H I clouds are deprojected into distances using two different Galactic rotation curve models: Reid et al. (2019) and Clemens (1985). These two rotation curves are among the most widely used in the literature: Clemens (1985) is based on CO observations and adopts $R_0 = 8.5$ kpc and $\Theta_0 = 220$ km s^{-1}, while Reid et al. (2019), derived from maser parallaxes of high-mass star-forming regions, assumes $R_0 = 8.15$ kpc and $\Theta_0 = 236$ km s^{-1}. For each velocity, the deprojection yields two possible distances that are displayed along the two horizontal axes in Figure 4.8.

In general, the Galactic rotation curve model of Reid et al. (2019) provides a better match to the dust cloud locations derived in this work compared to the Clemens (1985) model. However, at large distances, even the Reid et al. (2019) model appears to diverge systematically from the distribution of the dust clouds, suggesting possible deviations in the assumed Galactic dynamics. In particular, in the directions of GRB 221009A and GRB 160623A, the peaks obtained from the Reid et al. (2019) model are systematically at smaller distances than those derived from X-ray data, whereas the Clemens (1985) rotation curve always provides larger distances.

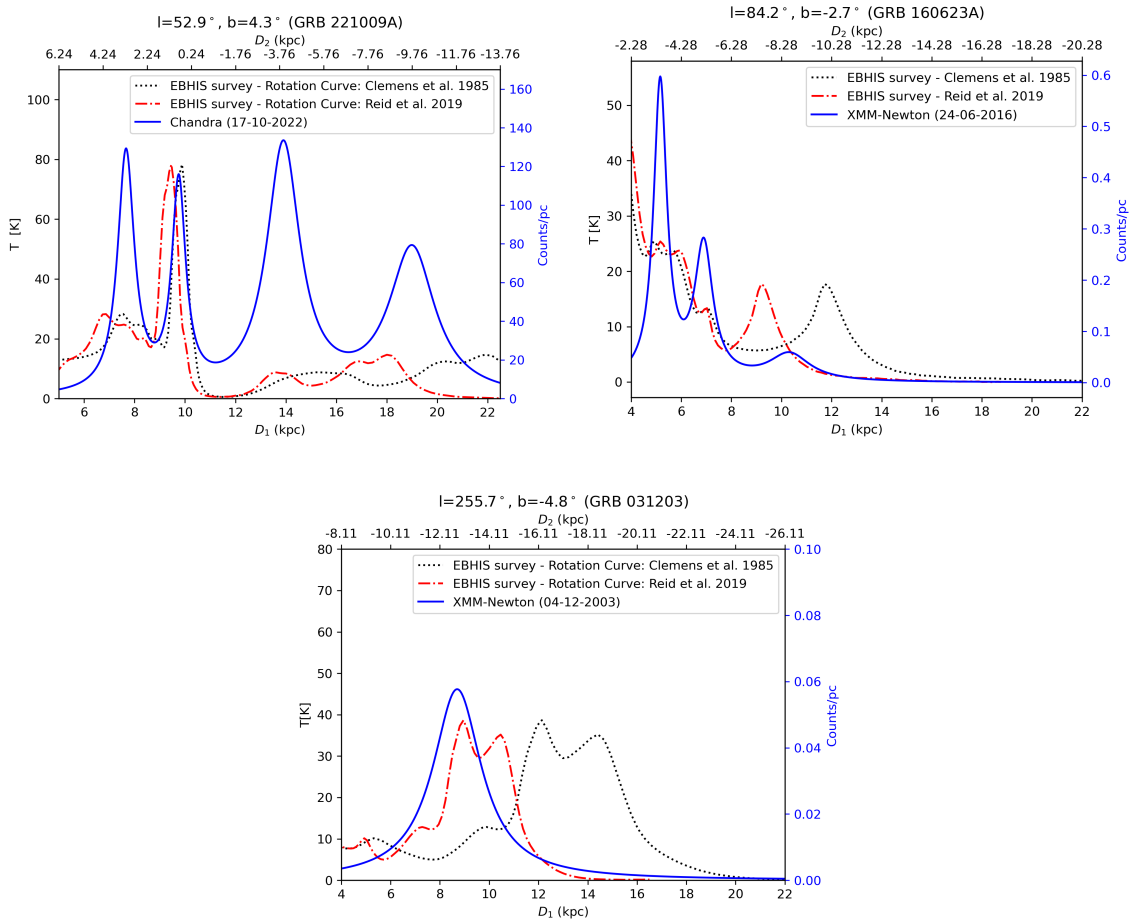

Figure 4.8: Comparison of our dust distance measurements (blue solid lines) in the directions of GRB 221009A (upper panel), GRB 160623A (central panel) and GRB 031203 (lower panel) with H I data from the EBHIS survey (Winkel, B. et al., 2016) for GRB221009A and GRB100623A, and from the GASS survey (HI4PI Collaboration: et al., 2016) for GRB031203. The LSR velocities are deprojected into distances using two different models for the Galactic rotation curve: Reid et al. (2019) (red dot-dashed lines) and Clemens (1985) (black dotted lines).

We also examined the sightlines towards the three GRBs using the CO survey by Dame et al. (2001), extracting data in the GRB directions and averaging over a 1° region. However, no significant CO emission was detected at distances greater than 5 kpc.

4.5 Conclusions

Combining *XMM-Newton* and *Chandra* observations of three low-latitude GRBs in different directions, we could map multiple Galactic spiral arms, cross-check distances, and provide robust constraints on the large-scale geometry of the outer Galaxy. In particular, our measurement of the OSC arm places it at 19.0 ± 0.2

kpc, achieving a precision far superior to the previous maser-parallax measurements ($20.4^{+2.8}_{-2.2}$ kpc; Sanna et al. 2017).

Although low-latitude GRBs as bright as GRB 221009A are very unlikely to repeat soon, future X-ray observatories such as *AXIS* (Reynolds et al., 2023) and *New Athena* (Cruise et al., 2025) will enable systematic campaigns of GRB follow-ups, which, thanks to their higher sensitivity, will expand the sample of X-ray rings generated by dust in the outskirts of the Milky Way. This will allow precise mapping of interstellar clouds traced by dust along more sightlines, complementing the 3D dust distributions derived from extinction studies in the optical and infrared band, based, for example, on future Gaia Data Releases and the Galactic plane Survey that will be performed by the *Nancy Grace Roman Space Telescope* (Akeson et al., 2019).

Chapter 5

Investigating interstellar dust along the line of sight of GX 13+1 using different dust size distributions

5.1 Introduction

In the previous chapters, X-ray scattering by interstellar dust was employed as a tool to probe both the spatial distribution of dust clouds and the overall properties of the dust grains along the line of sight. In this final part of the thesis, the focus shifts from scattering to absorption. As already described in Sect. 2.2, the presence of solid particles modifies the X-ray absorption edges of abundant metals, producing oscillatory modulations known as X-ray Absorption Fine Structure (XAFS; Costantini and Corrales 2022). These features are sensitive to the chemical composition, crystallinity, and internal structure of the grains, and therefore modeling them provides a unique diagnostic of the physical and chemical state of interstellar dust.

Current models of XAFS are based on dedicated laboratory measurements performed at synchrotron facilities. In particular, the Si K edge has been extensively studied by Zeegers et al. (2017), while the Mg K edge has been investigated by Rogantini et al. (2019). These laboratory data represent the fundamental basis for accurate modeling of the X-ray absorption features observed in astronomical sources.

In this chapter, we study the Si K and Mg K absorption edges (1.84 keV and 1.3 keV) observed with the *Chandra* High Energy Transmission Grating Spectrometer (HETG, Appendix A) toward the bright low-mass X-ray binary GX 13+1. For the first time, we directly compare the traditional MRN grain size distribution with more complex models, including the Weingartner and Draine (2001) distribution for three different values of R_V (3.1, 4.0, and 5.5), and the Hirashita and Murga (2020) distribution for four different dense-gas fractions, $\eta_{\rm dense} = 0.1$, 0.3, 0.5, and 0.8.

The chapter is organized as follows: Section 5.2 introduces the dust size distribution models; Section 5.3 describes the data reduction; Section 5.4 presents the analysis methodology and results; Section 5.5 discusses the implications of our findings; Section 5.6 summarizes the conclusions.

5.2 Dust size distributions models

This project includes several commonly used dust size distributions which are adapted to the X-ray spectrum. In previous X-ray spectroscopy studies of interstellar dust, the size distribution of the dust grains was calculated using a MRN size distribution (e.g., Zeegers et al., 2017; Rogantini et al., 2018). In this work, we compare that with more complex dust size distribution models, such as those by Weingartner and Draine (2001) and Hirashita and Murga (2020). These models do not consider mixed carbonaceous and silicate dust and thus contain separate grain size distributions for carbonaceous and silicate dust grains. Examples of the size distribution models are shown in Figure 5.1. The simplest model is the MRN model, shown by the orange line. This model was developed to describe the observed extinction by dust and is described in Section 1.2.5. Although the MRN model is a useful and simple parametrization of the size distribution, it does not always fit the observed extinction well. The extinction has been found to vary in the Galaxy and can be characterized by the parameter R_V (Cardelli et al., 1989). This parameter correlates with the density of the ISM and the grain size: a lower R_V corresponds to the diffuse ISM and indicates a larger population of small grains.

Therefore, Weingartner and Draine (2001) models expand the size distribution to smaller particles than the classic MRN distribution with a lower dust size limit of $a_{\rm min} = 3.5 \times 10^{-4}\,\mu$m. The grain size distribution is given by the function described in Section 1.2.5 (see Eq. 1.10, 1.11, and 1.12). We investigate this model using three different values of R_V (3.1, 4.0 and 5.5). The Hirashita and Murga (2020) model is a dust evolution model and models changes in the grain size distributions for 0.1, 0.3, 1.0, 3.0 and 10 Gyr. In our study we only considered the models with a dust evolution time of 10 Gyr, which resemble Milky Way dust. The silicate component in the Hirashita and Murga (2020) model accounts for about 60–70% of the total dust mass. The minimum grain size considered is $a_{\rm min} = 3 \times 10^{-4}\,\mu$m. Particles smaller than this size are too small to be regarded as dust grains. The largest grains used in their modeling are a $= 10\,\mu$m. Differences in gas density affect the grain growth and destruction mechanisms in the Hirashita and Murga (2020) dust evolution models. In this work, we investigate the size distribution models for four different values of dense gas fraction ($\eta_{\rm dense}$ = 0.1, 0.3, 0.5, 0.8), exploring different environments with different densities. Similarly to the models of Weingartner and Draine (2001), smaller grains are present in the most diffuse environments, as can be seen in Fig 5.1. The adaptation of these models to X-ray data follows the method described in Zeegers et al. (2017) and Rogantini et al. (2018), and summarized in Section 2.2.1, based on the MRN distribution. We used the same dust species and optical constants as those reported in Zeegers et al. (2019) and Rogantini et al. (2020). At each energy and grain size we calculated the extinction, scattering, and absorption efficiencies ($Q_{\rm ext}$,$Q_{\rm sca}$ and $Q_{\rm abs}$) using the anomalous diffraction theory (ADT) as described in Rogantini et al. (2018). The size distribution models from Weingartner and Draine (2001) have been calculated using the Fortran code referenced in their publication. In the case of Hirashita and Murga (2020) the size distributions are numerically derived and we use their tabulated dust size in our analysis. We then calculated the total cross section ($C_{\rm ext} = \pi a^2 Q_{\rm ext}$) by

integrating over the grain size distribution:

$$\sigma_{\rm ext} = \int C_{\rm ext}(a,\lambda) n(a) da \tag{5.1}$$

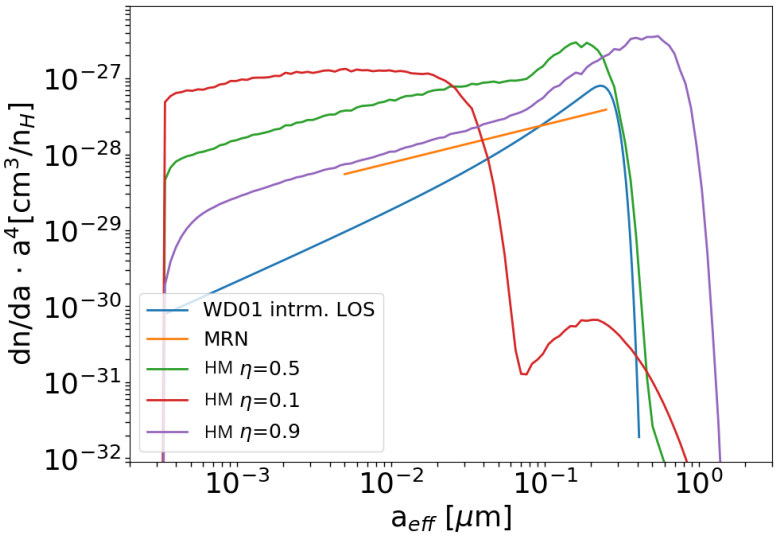

Figure 5.1: Comparisons of several different size distributions used in this study. The orange line shows the MRN distribution. The blue line shows the one of the Weingartner and Draine (2001) models with R_V of 4.0, indicated as WD01. Three models of Hirashita and Murga (2020) are shown by the green red and purple lines, showing different values of dense gas fraction with a dust evolution time of 10 Gyr.

5.3 Observations and data reduction

5.3.1 GX 13+1

GX 13+1 is a luminous neutron star LMXB, originally classified as an atoll source due to its lower luminosity (Hasinger and van der Klis, 1989). However, subsequent observations have revealed properties more characteristic of Z sources (Fridriksson et al., 2015). All *Chandra* observations of GX 13+1 exhibit wind signatures (Rogantini et al., 2025), characterized by significantly blue-shifted absorption lines produced by an ionized outflow, indicating the presence of disk winds with velocities reaching approximately $800\,{\rm km\,s^{-1}}$ (Ueda et al., 2004; Madej et al., 2014). GX 13+1 has previously shown type-I X-ray bursts (Matsuba et al., 1995) and absorption dips (Iaria et al., 2014), but we did not observe any such events in our light curves.

Located at approximately 7 kpc from Earth (Bandyopadhyay et al., 1999), GX 13+1 is positioned at Galactic coordinates ($b = 0°.11$, $l = 13°.52$) and its brightness $\simeq 6 \times 10^{-9}\,{\rm erg\,cm^{-2}\,s^{-1}}$ (D'Aì et al., 2014), makes it an ideal target for the investigation of absorption edges originating from the ISM. GX 13+1 has been included in samples aimed at studying the absorption edges produced by interstellar dust, particularly those associated with silicon (Zeegers et al., 2019; Yang et al., 2022) and sulfur (Gatuzz et al., 2024).

Table 5.1: Log of the *Chandra* observations used in this work.

Obs. ID	Start time (UTC)	Exposure (ks)
11814	2010-08-01T00:31:31	29.1
11815	2010-07-24T05:46:27	29.0
11816	2010-07-30T14:47:25	29.1
11817	2010-08-03T10:12:10	29.1
20191	2018-05-10T06:21:06	25.1
20192	2018-05-26T07:09:48	23.1
20193	2019-02-17T11:54:29	26.2
20194	2019-05-30T03:44:31	25.4

5.3.2 Data reduction

In this work, we report the analysis of X-ray data collected by the HETG instrument of *Chandra* (Canizares et al., 2005) in TE mode between July 2010 and May 2019 (Obs.ID in Table 5.1).

For each observation, we extracted the MEG +1 and MEG -3 spectra, and combined spectra of the same order across different observations using the CIAO tool combine_grating_spectra (version 4.15; Fruscione et al. 2006). These two orders (MEG +1 and MEG -3) are the only ones in which the silicon edge (6.74 Å) falls on a back-illuminated chip, thus avoiding the instrumental emission line reported by Rogantini et al. (2020) (see Appendix A).

The MEG +1 spectrum is affected by pile-up, particularly in the harder portion of the spectrum[1]. Therefore, we excluded the MEG +1 data in the ranges 3.4 Å–3.7 Å and 4.2 Å–5.9 Å. Additionally, to retain the superior resolution of the MEG -3 spectrum, we also excluded the MEG +1 data around the silicon edge (6.65 Å–6.77 Å).

5.4 Data analysis and results

We performed the spectral analysis using the code `spex` version 3.08 (Kaastra et al., 1996). All fits in this paper were performed using C-statistics (Cash, 1979; Kaastra, 2017), which can be used regardless of the number of counts per bin. All errors are quoted at the 90% confidence level for one interesting parameter.

[1]The magnesium and silicon edge regions are less susceptible to pile-up because ISM absorption significantly suppresses the spectrum in these areas.

5.4.1 Continuum and absorption

Following Zeegers et al. (2019), we modeled the soft X-ray emission with a disk blackbody component (`dbb`; Shakura and Sunyaev 1973) and the hard X-ray emission with a Comptonization model (`comt`; Titarchuk 1994). In the Comptonization model we fixed the temperature of the seed photons to that of the disk blackbody and left free to vary the plasma temperature ($T_{\rm comt}$). Absorption by cold interstellar gas was accounted for using the `hot` model (de Plaa et al., 2004), with the temperature fixed at 1×10^{-6} keV. We adopted the protosolar abundances from Lodders (2010), which are the default in `spex`. To model the ionized outflowing gas from the source we added a `xabs` model (Steenbrugge et al., 2003), leaving free to vary the average systematic velocity of the absorber (`zv`) and the root mean square velocity (`v`). We simultaneously fit the continuum of the two datasets – one containing MEG+1 and the other MEG-3 data – while linking the absorption parameters between them. We found a photo-ionized gas in outflow with a velocity $\texttt{zv} = (-4.7 \pm 1.8) \times 10^2\,\mathrm{km\,s^{-1}}$, $\texttt{v} = (3.0 \pm 0.5) \times 10^2\,\mathrm{km\,s^{-1}}$, a logarithmic ionization parameter $\log \xi = 4.3^{+0.1}_{-0.3}$, and a hydrogen column density of $N_{\rm H} = (1.3 \pm 0.6) \times 10^{23}$ cm^{-2}. These values are consistent with those found by Zeegers et al. (2019). For the cold absorber, instead, we found a hydrogen column density of $N_{\rm H} = (3.4^{+0.5}_{-0.6}) \times 10^{22}$ cm^{-2}, consistent with the value found in previous works (Zeegers et al., 2019; Pintore et al., 2014; D'Aì et al., 2014). All fitting parameters are reported in Table 5.2.

Table 5.2: Best-fit parameters derived for the continuum in the two different datasets.

	MEG -3	MEG +1
$N_{\rm H}^{\rm cold}$ (10^{22} cm^{-2})	$3.4^{+0.5}_{-0.6}$	
$k_{\rm B}T_{\rm dbb}$ (keV)	0.7 ± 0.1	
$k_{\rm B}T_{\rm comt}$ (keV)	18^{+12}_{-9}	20 ± 15
$\tau_{\rm comt}$ (keV)	$0.9^{+1.0}_{-0.1}$	$0.7^{+1.4}_{-0.1}$
$N_{\rm H}^{\rm xabs}$ (10^{23} cm^{-2})	1.3 ± 0.6	
$\log \xi^{\rm xabs}$	$4.3^{+0.1}_{-0.3}$	
$\texttt{zv}_{\rm out}^{\rm xabs}$ (10^2 km s^{-1})	-4.7 ± 1.8	
$\texttt{v}^{\rm xabs}$ (10^2 km s^{-1})	3.0 ± 0.5	
$F_{2-10\,\rm keV}$ (10^{-9} erg cm^{-2} s^{-1})	8.5 ± 0.4	

5.4.2 The dust model

After modeling the continuum of our source, along with the neutral and ionized absorption components, we included the dust model in the fit to simultaneously account for the magnesium and silicon absorption edges. As noted by Rogantini

et al. (2019), fitting both edges simultaneously helps to better constrain the dust properties, reducing the potential degeneracies. The `spex amol` model calculates the transmission of various molecules considering both absorption and scattering. By default, the extinction models in `spex` are evaluated for grains with a standard MRN size distribution. In this work, we will test the grain size distribution models described in Section 5.2.

The `amol` model supports the simultaneous fitting of mixtures comprising up to four distinct dust components. According to the approach outlined in Costantini et al. (2012), the total number of possible compound combinations is given by:

$$C_{n,k} = \frac{n!}{k!(n-k)!} \tag{5.2}$$

where n represents the total number of available compounds (16 in this case, as listed in Table 5.3) and k is the number of components in each combination (4). To fit the data, $C_{n,k}$ models are employed, with each unique combination representing a distinct extinction model. This process is repeated for each dust size distribution.

Following the approach in Rogantini et al. (2019) and Rogantini et al. (2020), we selected models that are statistically comparable to the best fit using the *Akaike Information Criterion* (AIC, Akaike 1974). According to the criteria outlined by Burnham and Anderson (2002), models with a $\Delta\text{AIC} < 4$ are considered statistically indistinguishable from the best fit, while those with a $\Delta\text{AIC} > 10$ are excluded from further consideration.

In Fig. 5.2, we show the variation in the extinction cross section for different dust size distributions, comparing these with the classical MRN model. The distributions from Hirashita and Murga (2020), characterized by varying dense gas fractions, and those from Weingartner and Draine (2001), defined by differing levels of reddening, both exhibit a larger fraction of bigger grains as these parameters increase. This variation significantly influences the scattering behavior near the Magnesium ($\sim$ 1305 eV = 9.5 Å) and Silicon ($\sim$ 1839 eV = 6.74 Å) absorption edges, since the scattering efficiency increases with grain size.

In the subsequent section, we present the results obtained for each dust size distribution. The dust and gas column densities derived using the best-fit dust compositions for all distributions are summarized in Table 5.4.

MRN distribution

The initial analysis employed the standard MRN size distribution for the extinction cross section, used to model the edge profiles (black curves in Fig. 5.2). The dust composition providing the closest match to the observed data primarily comprised amorphous olivine ($\sim$ 80%), with a smaller contribution from fully amorphous quartz $\sim$ 20% (see the top left panel in Fig.5.4). The model yielding the best statistical fit resulted in a C-statistic of 1677 with 1464 degrees of freedom.

Weingartner & Draine

The application of the dust size distribution from Weingartner and Draine (2001) with $R_V = 3.1$ (red curves in Fig. 5.2) resulted in a best-fit composition predomi-

Table 5.3: Dust samples used in this work, with their chemical formula, form, and references.

Name	Chemical formula	Form	References
Olivine	$MgFeSiO_4$	amorphous	[2],[3]
Olivine	$Mg_{1.56}Fe_{0.4}Si_{0.91}O_4$	crystalline	[1],[2],[3]
Fayalite	Fe_2SiO_4	crystalline	[2],[4]
Forsterite	Mg_2SiO_4	crystalline	[2],[3]
Quartz	SiO_2	crystalline	[3]
Quartz	SiO_2	amorphous	[3]
Quartz	SiO_2	amorphous	[3]
Spinel	$MgAl_2O_4$	crystalline	[3],[5]
Enstatite	$MgSiO_3$	amorphous	[2],[3]
Enstatite	$MgSiO_3$	crystalline	[2],[3]
En75Fe25	$Mg_{0.75}Fe_{0.25}SiO_3$	amorphous	[2],[3]
En60Fe40	$Mg_{0.6}Fe_{0.4}SiO_3$	amorphous	[1],[2],[3]
En60Fe40	$Mg_{0.6}Fe_{0.4}SiO_3$	crystalline	[1],[2],[3]
En90Fe10	$Mg_{0.9}Fe_{0.1}SiO_3$	amorphous	[1],[2],[3]
En90Fe10	$Mg_{0.9}Fe_{0.1}SiO_3$	crystalline	[1],[2],[3]

[1] Rogantini et al. (2018), [2] Zeegers et al. (2019), [3] Rogantini et al. (2020), [4] Lee and Ravel (2005), [5] Costantini et al. (2019).
The amorphous quartz samples are distinguished into intermediate and fully amorphous structures.

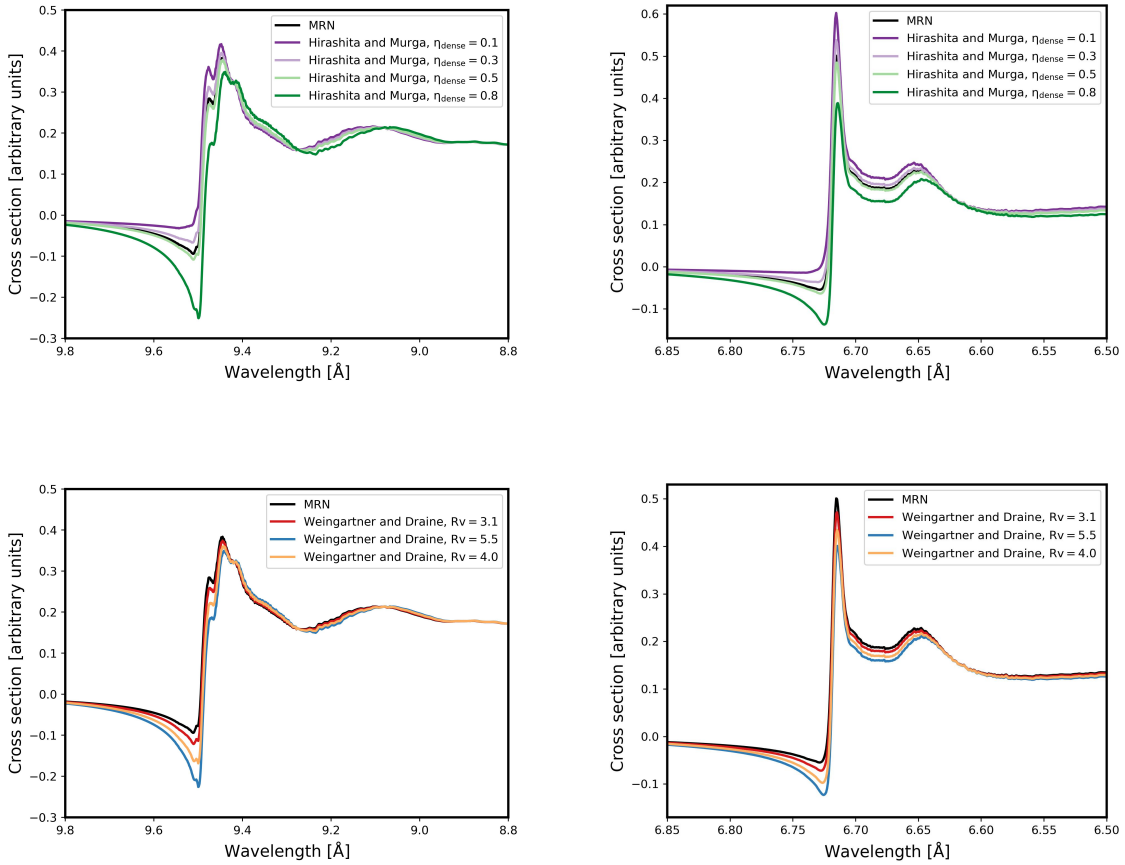

Figure 5.2: Extinction cross sections of amorphous olivine calculated with different dust size distributions, shown around the magnesium edge (left column) and the silicon edge (right column). The top row compares the MRN distribution (black) with that of Hirashita and Murga (2020) for dense gas fractions of 0.1 (purple), 0.5 (light purple and light green), and 0.8 (green). The bottom row compares the MRN distribution (black) with that of Weingartner and Draine (2001) for reddening values of $R_V = 3.1$ (red), $R_V = 4.0$ (orange), and $R_V = 5.5$ (blue).

nantly consisting of amorphous olivine ($\sim 70\%$), with a complementary component of fully amorphous quartz ($\sim 30\%$), as illustrated in the Top right panel in Fig. 5.4. This model achieved a C-statistic of 1681 with 1464 degrees of freedom. Raising the R_V up to 4 the fit yielded – instead – a C-statistic of 1696 for 1464 degrees of freedom. Increasing R_V further to 5.5 (blue line in Fig. 5.2) resulted in an even higher C-statistic of 1708. However, models with such high R_V values are rejected by the Akaike test, described in Section 5.4.2.

Hirashita & Murga

Adopting the dust size distribution of Hirashita and Murga (2020) for a diffuse interstellar medium ($\eta_{\rm dense} = 0.1$; purple curve in Fig. 5.2) the fit yields a C-statistic of 1692, while for a dense medium ($\eta_{\rm dense} = 0.8$; Fig. 5.2, green curve) the value increases to 1719. Both cases are rejected by the Akaike test. Intermediate fractions

	MRN	WD	WD	WD	HM	HM	HM	HM
		$R_V = 3.1$	$R_V = 4.0$	$R_V = 5.5$	$\eta_{\rm d} = 0.1$	$\eta_{\rm d} = 0.3$	$\eta_{\rm d} = 0.5$	$\eta_{\rm d} = 0.8$
$N_{\rm a,olivine}\,(10^{18}\,{\rm cm}^{-2})$	$1.2^{+0.2}_{-0.5}$	0.9 ± 0.2	0.8 ± 0.3	0.5 ± 0.1	$1.1^{+0.1}_{-0.2}$	$1.0^{+0.1}_{-0.2}$	$0.8^{+0.4}_{-0.5}$	0.5 ± 0.1
$N_{\rm a,quartz}\,(10^{18}\,{\rm cm}^{-2})$	$0.3^{+0.3}_{-0.1}$	$0.4^{+0.2}_{-0.1}$	0.5 ± 0.1	0.9 ± 0.1	$0.2^{+0.3}_{-0.1}$	$0.3^{+0.3}_{-0.1}$	0.5 ± 0.2	0.9 ± 0.1
$N_{\rm c,forsterite}\,(10^{18}\,{\rm cm}^{-2})$	–	–	–	–	–	–	$0.1^{+0.2}_{-0.1}$	–
$N_{\rm O}^{\rm gas}\,(10^{19}\,{\rm cm}^{-2})$	$1.2^{+0.6}_{-0.5}$	< 1.8	$1.7^{+0.1}_{-0.7}$	< 1.8	1.3 ± 0.2	< 1.8	$1.2^{+0.6}_{-0.3}$	1.2 ± 0.3
$N_{\rm Mg}^{\rm gas}\,(10^{17}\,{\rm cm}^{-2})$	$1.0^{+1.1}_{-1.0}$	2.2 ± 1.2	3.0 ± 1.8	$2.4^{+2.6}_{-0.1}$	0.024 ± 0.001	1.2 ± 0.1	$1.4^{+2.0}_{-1.4}$	$1.3^{+3.5}_{-0.7}$
$N_{\rm Si}^{\rm gas}\,(10^{17}\,{\rm cm}^{-2})$	0.2 ± 0.1	0.3 ± 0.1	0.4 ± 0.2	0.4 ± 0.2	0.1 ± 0.1	$0.2^{+0.2}_{-0.1}$	0.2 ± 0.1	0.5 ± 0.2
$N_{\rm Fe}^{\rm gas}\,(10^{16}\,{\rm cm}^{-2})$	$0.2^{+1.9}_{-0.1}$	< 2.1	< 2.1	< 2.1	< 2.1	< 2.1	< 2.1	< 2.1
C-stat	1677	1681	1696	1708	1692	1677	1681	1719
dof	1464	1464	1464	1464	1464	1464	1464	1464

Table 5.4: Column densities of dust and gas derived from the best-fit models for various dust size distributions. Notes: In all cases, as outlined in Section 5.4.2, four distinct dust components are fit simultaneously. However, with the exception of the Hirashita and Murga (2020) model (with $\eta_{\rm d} = 0.5$), only amorphous olivine and amorphous quartz contribute significantly to the fit.

provide better fits: for $\eta_{\rm dense} = 0.3$ (Fig. 5.2, light purple curve) the C-statistic is 1677, and for $\eta_{\rm dense} = 0.5$ (Fig. 5.2, light green curve), which closely resembles the MRN distribution, the C-statistic is 1681. In both Akaike-accepted models, the composition is dominated by amorphous olivine, with amorphous quartz contributing approximately 20–30% (Fig. 5.4).

Table 5.5: Abundances and fractional depletions of magnesium and silicon for the good dust size distributions.

	MRN	WD ($R_V = 3.1$)	HM ($\eta_{\rm d} = 0.3$)	HM ($\eta_{\rm d} = 0.5$)
silicon				
$A_Z/A_\odot$	1.4 ± 0.7	0.7 ± 0.4	$0.7^{+0.7}_{-0.3}$	0.7 ± 0.4
δ_Z	0.99 ± 0.01	0.97 ± 0.01	$0.98^{+0.01}_{-0.02}$	0.98 ± 0.01
magnesium				
$A_Z/A_\odot$	0.9 ± 0.7	0.9 ± 0.5	0.8 ± 0.2	0.8 ± 0.6
δ_Z	$0.92^{+0.08}_{-0.09}$	0.82 ± 0.10	0.90 ± 0.01	$0.88^{+0.12}_{-0.17}$

5.5 Discussion

5.5.1 Dust size distribution

From this analysis, we can rule out the following dust size distribution models along the line of sight of GX 13+1, as they yield ΔAIC values greater than 10 compared

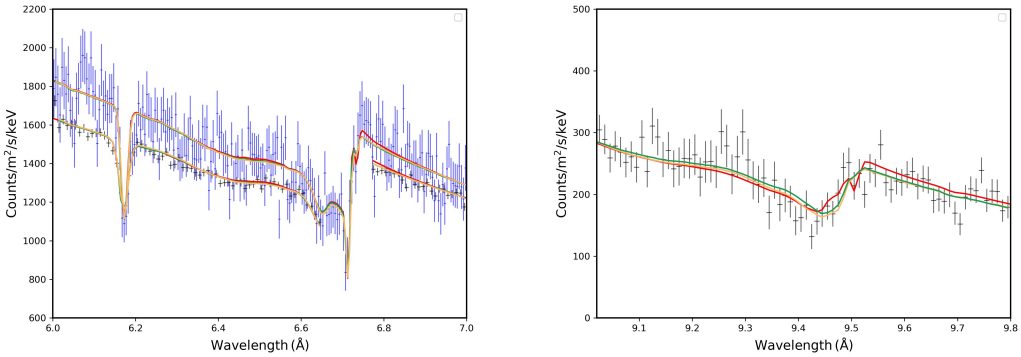

Figure 5.3: Best fits of the Si K edge (left panel) and Mg K edge (right panel) using the dust size distribution from Weingartner and Draine (2001) with $R_V = 3.1$ (in red), MRN (in yellow), and Hirashita and Murga (2020) with $\eta_{\rm dense} = 0.3$ (in green). *Chandra* MEG-3 data are shown in blue, and MEG+1 data in black.

to the best-fit model (see Tab. 5.4): the Weingartner and Draine (2001) models with $R_V = 4.0$ and $R_V = 5.5$, and the Hirashita and Murga (2020) models with $\eta_{\rm dense} = 0.1$ and $\eta_{\rm dense} = 0.8$. These results allow us to exclude, for this sightline, the presence of a denser-than-average ISM – represented by the Weingartner and Draine (2001) models with $R_V = 4.0$ and 5.5, and by the Hirashita and Murga (2020) model with $\eta_{\rm dense} = 0.8$. In the Milky Way, a typical average value is $R_V \simeq 3.1$ (Johnson, 1968), which can be used as a reasonable approximation for most lines of sight. This result is consistent with the findings of Schlafly et al. (2016), who report that fewer than one percent of Galactic sightlines exhibit $R_V > 4.0$.

We can also reject the scenario of an extremely diffuse ISM, represented by the Hirashita and Murga (2020) model with $\eta_{\rm dense} = 0.1$, where grain shattering dominates, leading to a dust size distribution favoring smaller grains.

5.5.2 Dust composition

The dust observed along the LOS to GX 13+1 reveals an ISM primarily composed of amorphous olivine, with a significant fraction (20–30%) of fully amorphous quartz. This finding, based on a different dataset, confirms the results of Zeegers et al. (2019) for this direction. Consistent with observations along other sightlines (Zeegers et al., 2019; Rogantini et al., 2020), we find no significant contribution from pyroxene; instead, olivine remains the dominant silicate component in the ISM. This dominance of olivine is further supported by infrared studies, such as Kemper et al. (2004), who reported that approximately 85% of the silicate dust is in olivine form.

Crystalline or amorphous SiO_2 (silica) is generally not considered a major constituent of the ISM, but amorphous silica has been sporadically detected. For example, Fogerty et al. (2016) reported up to 20% silica by mass in warm regions of the Trapezium LOS, based on analysis of the 9.7 μm feature. Moreover, amorphous silica is also observed in protoplanetary disks (Sargent et al., 2009), suggesting that while it is not a prevalent ISM component, it can appear in specific environments,

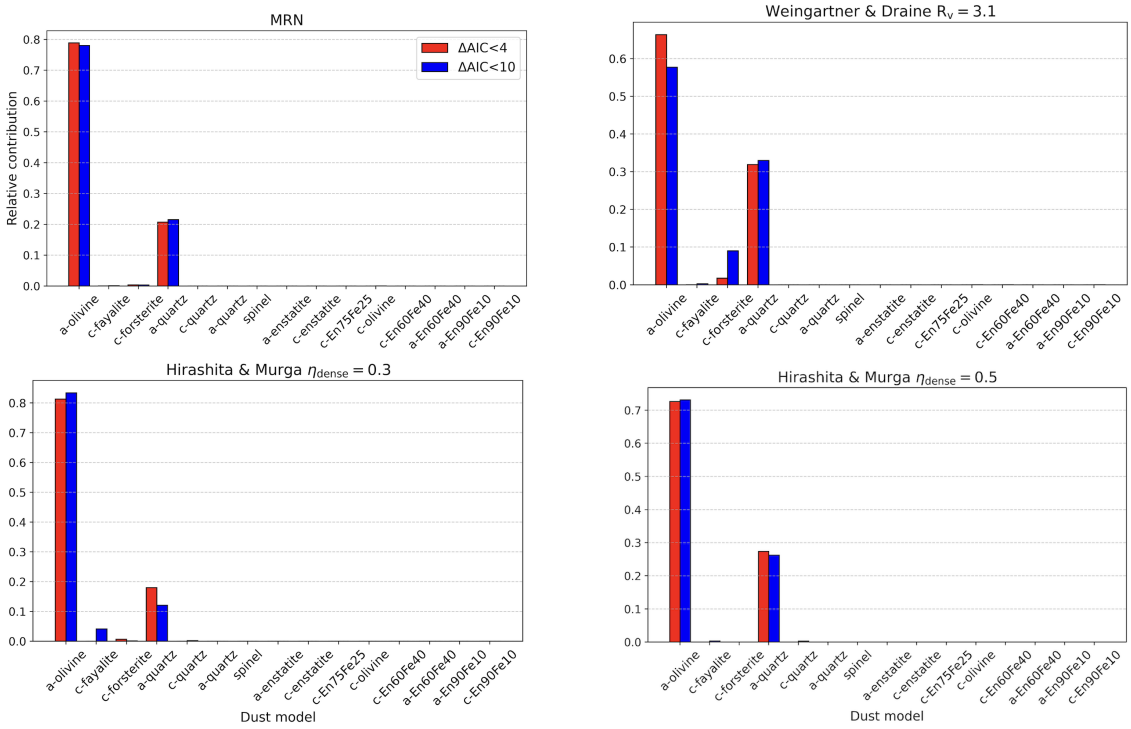

Figure 5.4: Histograms of the relative contribution of each dust species, based on AIC-selected models. Each panel shows results computed using different dust size distributions for the extinction cross section calculations.

possibly linked to local dust processing.

5.5.3 Depletions and abundances

From our spectral fits, we derived the depletion fractions of oxygen, magnesium, silicon, and iron – the constituents of our dust models (see Table 5.3). The fractional depletion is typically expressed as a percentage and is defined as $\delta_{\rm Z} = 1 - 10^{D_{\rm Z}}$, where $D_{\rm Z}$ is determined by comparing the abundance of the gas-phase element Z with its standard solar reference abundance.

For magnesium and silicon, whose absorption edges we explicitly modeled, we found significant depletion into the solid phase. In our best-fit models, 80-90% of magnesium and 97-99% of silicon are locked in dust grains (see Table 5.5).

The depletion fractions of oxygen and iron can only be inferred indirectly from our models and are therefore less tightly constrained. Our results suggest that oxygen is moderately depleted, with less than 30% incorporated into dust, while more than 80% of iron appears to be in the solid phase.

The depletion levels derived in this work are consistent with previous X-ray studies (e.g., Costantini et al. 2012; Pinto et al. 2013; Zeegers et al. 2019; Rogantini et al. 2019; Rogantini et al. 2020) and are also in agreement with the depletions reported by Jenkins (2009) and Dwek (2016). Our derived elemental abundances are consistent with those reported in previous studies (e.g., Zeegers et al. 2019; Rogantini et al. 2020) and do not show significant deviations from solar values (see

Table 5.5).

5.5.4 Dust crystallinity

The best-fit model suggests a crystalline-to-amorphous dust ratio (ζ_1 = crystalline dust / (crystalline dust + amorphous dust)) lower than that reported in previous X-ray studies of several LMXBs (Zeegers et al., 2019; Rogantini et al., 2019; Rogantini et al., 2020), but consistent with values observed in the infrared. In particular, at these wavelengths, the smooth profiles of the features near $\sim 9\,\mu$m and $\sim 18\,\mu$m indicate that less than 2.2% of interstellar dust is crystalline (Kemper et al., 2004, 2005). In this work, we find $\zeta_1 = 0.02$, with an upper bound $\zeta_1 \leq 0.05$.

A key aspect of this work is the significantly improved spectral resolution, made possible by using, for the first time, the third-order spectrum of the *Chandra* HETG. Moreover, such analysis has been performed on data unaffected by known instrumental features near the Si K edge (see Appendix A), ensuring a clearer view of the absorption profile. These improvements enable a more reliable characterization of interstellar dust along this line of sight.

5.6 Conclusions

In this work, we used *Chandra* HETG (MEG+1 and MEG-3) observations of GX 13+1 to study the composition and size distribution of interstellar dust along its line of sight. By modeling the Si K and Mg K edges with a range of laboratory-based dust species and grain size distributions, we constrained both the physical and chemical properties of the ISM. Our analysis shows that:

- The classical MRN, the Weingartner and Draine (2001) ($R_V = 3.1$) distributions, along with the Hirashita and Murga (2020) ($\eta_{\rm dense} = 0.3 - 0.5$) models, best reproduce the observed absorption profiles. Distributions representing very dense or highly diffuse ISM are statistically disfavored.
- The dust in this LOS is predominantly composed of amorphous olivine.
- The crystalline fraction of dust is extremely low ($\leq 5\%$), consistent with infrared measurements.

These findings confirm the presence of typical diffuse ISM conditions along the sightline to GX 13+1 and emphasize the role of X-ray spectroscopy as a powerful tool for probing the solid phase of the interstellar medium. Looking ahead, *New Athena* observations will provide unprecedented improvements thanks to its high effective area. This will enable the detection of Mg and Si absorption features with high signal-to-noise ratios, allowing us to place more stringent constraints on grain composition, crystallinity, and size distributions across different Galactic environments.

Chapter 6

Conclusions and Future Prospects

6.1 Summary of the main results

This thesis investigated how X-ray scattering and absorption can jointly be used as probes to study the properties and the spatial distribution of interstellar dust. In Chapter 3 we presented a detailed analysis of the dust rings around the GRB 221009A, providing a detailed three-dimensional reconstruction of the interstellar medium along this direction. This work also led to an improved estimate of the soft X-ray fluence of GRB 221009A and provided an independent constraint on the absorption within its host galaxy. In Chapter 4, we extended this analysis to additional GRBs (160623A and 031203), focusing on the X-ray rings produced by more distant clouds associated with the Perseus, Outer, and Outer Scutum-Centaurus arms. These results are particularly relevant because, contrary to most commonly used techniques, they were derived without relying on the Milky Way rotation curve, which is still subject to significant uncertainties. In Chapter 5, we took advantage of high resolution spectroscopy to explore the composition and grain size distribution of the dust along the line of sight toward GX 13+1. For the first time, different grain-size distribution models (MRN, WD, and HM) were tested against the data, allowing us to obtain information not only on the composition of the dust, such as the crystalline fraction and the elemental depletions, but also on the grain-size distribution.

As briefly discussed in Chapter 2 and 3 (see, e.g., Table 3.1), valuable information on dust grain-size distribution and composition can also be derived from the study of X-ray dust scattering. Sneppen and Watson (2025) extended the analysis presented in Tiengo et al. (2023) and Vaia et al. (2025) by employing anomalous diffraction theory to model the ring brightness as a function of the scattering angle. This approach enabled for the first time a direct measurement of the complex refractive index of interstellar dust grains together with an accurate determination of their grain-size distribution. They found a maximum grain radius of about 0.24 μm, thus ruling out a significant population of large grains along this line of sight, and constrained the iron mass fraction, obtaining values consistent with the elemental abundances and depletion levels observed in the interstellar medium through high-resolution spectroscopy.

6.2 Work in progress and future projects

The results presented in this thesis help to address several of the open questions outlined in Section 1.4 but a lot of work can still be done taking advantage of the X-ray scattering and absorption process. The ongoing and future works described in the following section show some possible developments in this direction.

6.2.1 Investigating the relationship between optical extinction and X-ray absorption

An open question concerns the relationship between optical extinction and the hydrogen column density derived from X-ray spectral fitting. Although this relation has been explored for various astrophysical classes and instruments (see Section 1.2.6), it has never been studied on a large, homogeneous sample of stars with accurately known distances and high-quality X-ray spectra.

During my PhD, we initiated a pilot study to test the feasibility of this approach creating a preliminary sample of field star observed through both the Gaia and XMM-Newton missions. The aim was to verify the feasibility of a systematic analysis and to provide estimates for various parameters, such as the number of sources in the sample and the estimated ratio of N_H to A_v. Here, we outline the steps taken during the creation of this preliminary sample:

- The 4XMM-DR13 catalog was filtered by selecting only point-like sources with an equivalent detection likelihood greater than 1000, which usually provides a number of photons sufficient to perform a meaningful spectral analysis.

- A cross-match was made between the filtered catalog from the previous step and the full Gaia DR3 catalog. The matching procedure was based upon the angular distance between the XMM X-ray sources and potential Gaia counterparts, the assigned optical counterpart being the brightest within 3 arcsecs from the X source location.

- The new catalog underwent a second selection, in which we preserved only sources with well-determined (>20 sigma; Andrae et al. 2023) parallax and optical extinction (A_0), excluding cool stars ($T < 4000\,K$), for which Gaia extinction is less reliable.

- After the determination of the chance-coincidence probability by counting the number of stars within 3 arcmin, sources with a probability higher than 0.1% were excluded.

The result was a catalog of 355 sufficiently bright XMM-Newton sources with a stellar counterpart in the Gaia catalog with well-determined distance and optical extinction. As a feasibility study, we analysed the X-ray spectrum of a sample of 29 sources by selecting those with distances larger than 800 pc (to minimize the contribution from young stellar objects in nearby molecular clouds, which could introduce a bias due to extinction from protostellar disks), with the addition of a few

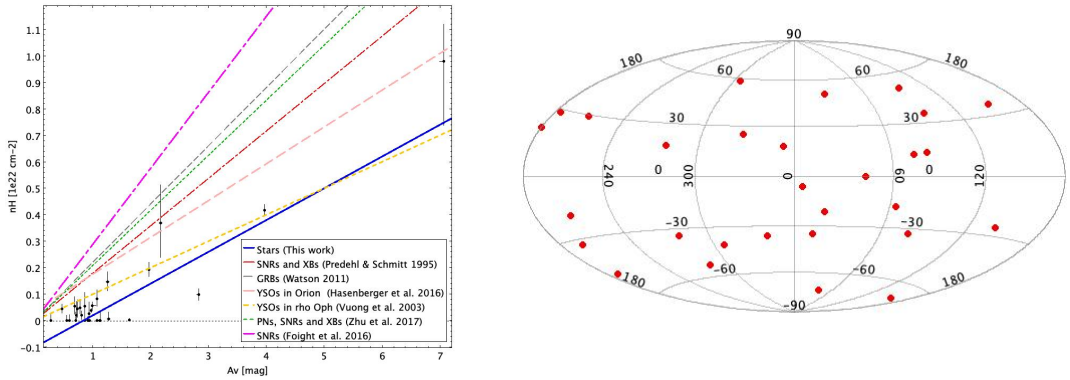

Figure 6.1: Left panel: Hydrogen column density derived from the X-ray spectra (N_H) vs. dust extinction (A_v).The blue line represents the best-fit linear relation determined from our data, while the dashed lines correspond to relationships previously established from different types of objects (XBs = X-ray binaries, SNRs = supernova remnants, GRBs = gamma-ray bursts, PNs = planetary nebulae, YSOs = young stellar objects; see Zhu et al. 2017 for details). Right panel: Spatial distribution, in Galactic coordinates, of the sources in our preliminary sample.

closer object to better sample the large extinction regime. The X-ray spectra were modeled with one or more (up to 3) absorbed collisional-radiative plasma model.

The left panel in Fig. 6.1 shows the correlation between the hydrogen column density derived from the X-ray spectra, and the dust extinction for the sample, with the resulting best-fit linear relation:

$$N_H = (1.2 \pm 0.2) \times 10^{21}\,cm^{-2}\,mag^{-1} A_v - (1.0 \pm 0.3) \times 10^{21}\,cm^{-2}. \quad (6.1)$$

The slope of the relation is compatible with the correlation found for young stellar objects in ρ Oph (Vuong et al., 2003) and in the Orion Nebula (Hasenberger et al., 2016), while our sample is mainly formed by uniformly distributed field stars (see the right panel in Fig. 6.1). The relations derived from other classes of X-ray sources are instead systematically steeper (left panel in Fig. 6.1). However, this discrepancy might be caused by the systematic overestimation of extinction, mainly for highly obscured stars, already noted in the Gaia catalog (Andrae et al., 2023). Conversely, an underestimate of X-ray absorption could result from using an incorrect modeling of the stellar X-ray emission. The presence of an intercept not compatible with 0 is another compelling indication of the need to refine and expand the sample.

6.2.2 Toward a systematic archival survey of X-ray dust scattering halos

Beyond these first results, an important next step is to move from individual case studies to a systematic, archival survey of X-ray dust-scattering phenomena.

To this end, an automated detection pipeline can be developed to search for dust-scattering rings and halos in archival *XMM-Newton*, *Chandra*, and *Swift* observa-

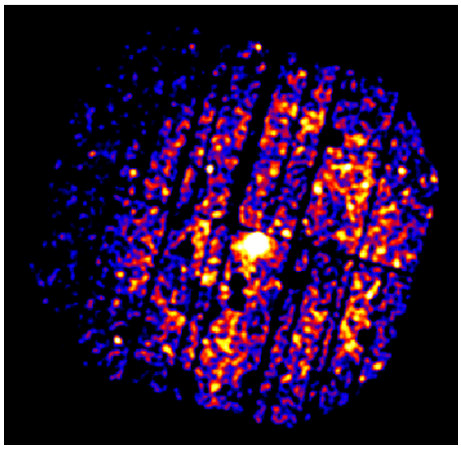

Figure 6.2: Halo surrounding Aql X-1 in the XMM-Newton data of its 2010 outburst

tions. This pipeline can integrate machine-learning techniques, such as convolutional neural networks for pattern recognition and anomaly detection, to efficiently identify ring-like structures. Training can be based on well-studied cases (e.g. GRB 031203, GRB 221009A) and on simulations of similar events. The expected outcome is a robust and reproducible framework that reduces human bias and enables the creation of a preliminary catalog of candidate scattering events.

For each identified candidate, the analysis strategy can differ depending on the nature of the associated source:

- Extragalactic sources: the method described in Chapter 3 can be applied to reconstruct the three-dimensional dust distribution along the line of sight.

- Galactic sources with uncertain distances (e.g., the X-ray binary Aql X-1; see Section 6.2.3): if at least one dust layer is known from independent tracers (e.g. CO or HI surveys, extinction maps, or maser parallax measurements), the halo geometry can be used to estimate the source distance. This approach is particularly effective for X-ray binaries and transients in the Galactic plane, many of which still lack precise distance estimates.

The expected outcomes are refined distance determinations for a sample of Galactic X-ray sources and high-resolution dust maps in several Galactic directions. In particular, this technique can be used to increase the small sample of GRBs with dust-scattering rings (Šiljeg et al., 2023), which would allow us to map additional directions of the Galaxy.

As shown in Chapter 4, we have already identified new scattering rings in archival *XMM-Newton* data. In addition, as briefly reported here below (Section 6.2.3), from a preliminary archival search we discovered a time-variable X-ray halo around Aql X-1 in *XMM-Newton* observations of its 2010 outburst. Since the distance to Aql X-1 remains uncertain, analyzing this halo can provide a more precise and independent distance determination.

6.2.3 Aql X-1

The low-mass X-ray binary Aquila X-1 (or Aql X-1), discovered by Kunte et al. (1973), is one of the most active neutron star X-ray transients known. It has exhibited both coherent millisecond X-ray pulsations at approximately 1.8 ms (Casella et al., 2008) and thermonuclear bursts (e.g., Galloway et al. 2008). The 2010 outburst was among the brightest ever observed, reaching a peak luminosity of about 350 mCrab around September 14, 2010.

XMM-Newton observed Aql X-1 five times during the decay of the 2010 outburst (see Table 6.1). We analyzed only data from the pn camera when the observations were obtained in full window mode and only MOS2 data elsewhere. We do not report the analysis of the MOS1 data due to the permanent damage sustained by two external CCDs during the early stages of the mission. These data were processed using the Science Analysis Software (SAS) 20.0.0 (Gabriel et al., 2004) and the latest calibration files. The EPIC events were cleaned with standard filtering expressions[1]. To maximize the signal-to-noise ratio of the scattering halo, the analysis was confined to the 0.4 – 2 keV energy range.

For each observation, we derived the corresponding radial profile (Fig. 6.3). A clear excess is visible in each of these profiles, which – moreover – expand over time, indicating that they are not background features but rather an evolving halo. The decaying side of the bump corresponds to the earliest photons produced by the burst on September 14, 2010, and, thus, the first to be scattered.

As discussed in Section 2.1, for Galactic sources Equation 2.1 can be used to infer the distance to the source, once the distance to the dust cloud has been provided. To tackle this problem, we used the optical/IR 3D extinction map by Green et al. (2019). Extracting the map in the direction of Aql X-1 (Fig. 6.4), two prominent increases in extinction are apparent: the first at around 200 pc and the second between 3 and 5 kpc. Assuming that the latter structure produced the halo and using the angular size corresponding to the end of the bump together with the start time of the observations, Equation 2.1 yields–for all five halos–a source distance of $D_{\rm s} = 6^{+3}_{-2}$ kpc. This value is compatible with the distance estimated from type I burst photospheric radius expansion (< 6 kpc; Galloway et al. 2008) and from IR spectroscopy (6 ± 2 kpc; Mata Sánchez et al. 2016).

This analysis represents a preliminary step; future work will aim to obtain a more accurate distance estimate by employing other dust maps, which can help to better constrain the dust layer responsible for the observed halo.

6.3 Future Missions

The XMM-Newton and Chandra X-ray observatories have enormously advanced the study of the ISM even thanks to their grating instruments (see for example Chapter 5). The next-generation observatory *New Athena* (Cruise et al., 2025), equipped with a cryogenic X-ray calorimeter, will deliver high-resolution spectroscopy over a broader energy range. This will allow detailed studies of absorption edges at

[1]For pn data: `#XMMEA_EP&&(FLAG==0)&&(PATTERN<=4)` and for MOS: `#XMMEA_EM&&(PATTERN<=12)`.

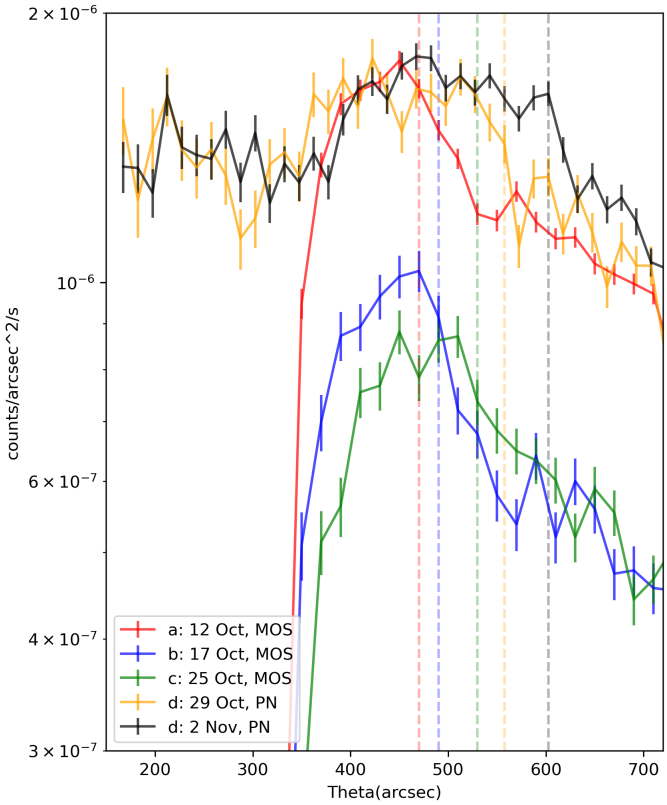

Figure 6.3: Radial profiles of the five *XMM-Newton* observations listed in Table 6.1. The vertical dashed lines mark the end of the bump, clearly showing an expansion over time.

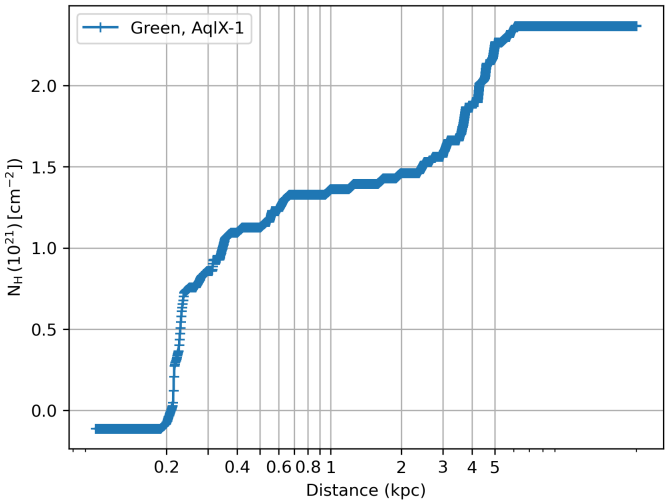

Figure 6.4: Cumulative hydrogen column density derived from Green et al. (2019) in the direction of Aql X-1.

Table 6.1: Log of the *XMM-Newton* observations of Aql X-1 used in this work.

Obs. ID	Start date (UTC)	Instrument	Observing mode
0085180101	2010-10-12	pn	Burst
"	"	MOS1	Timing
"	"	MOS2	Timing
0085180201	2010-10-17	pn	Timing
"	"	MOS1	Large Window
"	"	MOS2	Timing
0085180301	2010-10-25	pn	Timing
"	"	MOS1	Large Window
"	"	MOS2	Timing
0085180401	2010-10-29	pn	Full window
"	"	MOS1	Full window
"	"	MOS2	Full window
0085180501	2010-11-02	pn	Full window
"	"	MOS1	Full window
"	"	MOS2	Full window

higher energies – such as those of aluminum, sulfur, calcium, and iron (Fe K) – in addition to offering enhanced sensitivity and resolution around the magnesium and silicon K edges (Costantini and Corrales, 2022). Such advancements will open new diagnostic windows on the chemical composition, ionization state, and physical conditions of interstellar dust. At lower energies, missions with higher resolving power, such as the proposed concept mission *Arcus* (Smith et al., 2022), would allow detailed studies of the oxygen K edge together with the iron L edges and the carbon K edge. High-resolution spectroscopy of this region would be particularly valuable, as it could distinguish between different carbonaceous dust components, such as graphite, amorphous carbon.

Furthermore, as discussed in Chapter 4, although exceptionally bright, low-latitude gamma-ray bursts (GRBs) like GRB 221009A are expected to be rare, forthcoming missions such as *New Athena* and *AXIS* (Reynolds et al., 2023) will enable systematic X-ray follow–ups of GRB afterglows. The enhanced sensitivity of these future instruments will make it possible to detect a larger number of scattering rings and halos, including those that are significantly fainter than what can currently be observed.

Appendix A

The XMM-Newton, Swift, and Chandra X-ray satellites

A.1 XMM-Newton

The *XMM-Newton* observatory (Jansen et al., 2001), named in honor of the English physicist Isaac Newton, was launched on December 10, 1999, and represents the most significant contribution of the European Space Agency (ESA) to X-ray astrophysics research. The system is 10.8 m long, weighs 3,764 kg, and has a width of 16.16 m when the solar panels are fully deployed. It was placed into an elliptical orbit with an apogee of about 115,000 km and a perigee of roughly 6000 km. However, due to various perturbations and a correction maneuver carried out in 2003, the orbital parameters gradually evolve over time. Along this orbit, several observational constraints must be taken into account, as they can strongly influence target scheduling. For example, scientific observations are impossible when the spacecraft passes through the radiation belts[1], because the high radiation levels could harm the instruments. Moreover, the Sun, Earth, and Moon are too bright, and the telescope can never be pointed close to their directions.

The satellite carries three main instruments: three European Photon Imaging Cameras (EPIC, Turner et al. 2001; Strüder et al. 2001), two high-resolution Reflection Grating Spectrometers (RGS, den Herder et al. 2001), and one Optical Monitor (OM, Mason et al. 2001).

The system is equipped with three X-ray telescopes, each consisting of 58 mirrors. They are designed to operate in the X-ray energy range of 0.1 keV to 12.0 keV, with a focal length of 7.5 m. Table A.1 lists the full width at half maximum (FWHM) and half energy width (HEW) values of the Point Spread Function (PSF), derived from both ground-based and in-orbit measurements. The effective FOV of the EPIC instruments is approximately $30'$ in diameter.

Each telescope is equipped with one EPIC camera, which are of two different types:

- Two MOS-CCD cameras (Turner et al., 2001). Each of these cameras consists

[1]The Earth's magnetosphere captures energetic charged particles, forming two regions of intense radiation known as the Van Allen Belts, which protect the planet from solar storms and the continuous solar wind.

Table A.1: Full Width at Half Maximum (FWHM) and Half Energy Width (HEW) of the PSF for different mirror modules, derived from both in-orbit and ground measurements.

Instrument	pn	MOS-1+RGS-1	MOS-2+RGS-2
Measurement	orbit/ground	orbit/ground	orbit/ground
FWHM [″]	$< 12.5/6.6$	4.3/6.0	4.4/4.5
HEW [″]	16.6/15.1	16.8/13.6	17.0/12.8

of seven silicon chips (one in the center and six surrounding it, see the left panel of Figure A.1), with each chip containing an array of 600 x 600 pixels. The energy resolution at 1 keV is $\simeq$ 70 eV.

- One pn-CCD camera (Strüder et al., 2001). This camera is made up of 12 CCDs, each with dimensions of 64 x 200 pixels (see right panel Figure A.1). The energy resolution at 1 keV is $\simeq$ 80 eV.

The two MOS-CCD cameras detect only ∼50% of the incoming radiation, as the other half is directed to the associated RGS. These instruments are designed to obtain high-resolution spectra in the 0.3-2.5 keV energy band, through the combination of reflection gratings and CCD detectors. Although the RGS intruments cannot provide 2D images, they have a much better energy resolution of 0.025 Å (i.e 2 eV) at 1 keV. The EPIC cameras support multiple data acquisition modes. For the MOS detectors, the six peripheral CCDs always operate in standard imaging mode, while the central CCD can be configured independently. Consequently, all MOS CCDs collect data continuously, regardless the selected operating mode. The available modes–Full Frame, Large Window, and Small Window–differ mainly in FOV (600x600, 300x300, and 100x100) and time resolution (2.6 s, 0.9 s, and 0.3 s, respectively). The use of faster readout modes is essential for very bright sources, as they minimize the effects of photon pile-up–where multiple photons are registered as a single event within one frame–and allow accurate timing and spectral measurements without saturation. In contrast, the slower full-imaging modes are best suited for faint or extended sources, where spatial coverage is prioritized over timing accuracy.

The pn camera CCDs, on the other hand, can be operated either across all chips – in Full Frame, Extended Full Frame, and Large Window modes – or restricted to a single CCD (CCD 4 in Fig. A.1) for Small Window, Timing, and Burst modes. As for the MOS camera, these modes differ mainly in time resolution and FOV: the Full Frame modes offer complete imaging at the expense of longer time resolution (up to 73.4 ms), whereas the Small Window and Timing modes achieve higher time resolution (down to 5.7 ms and 0.03 ms, respectively) by reading out a reduced detector area (63x64 and 64x200, respectively).

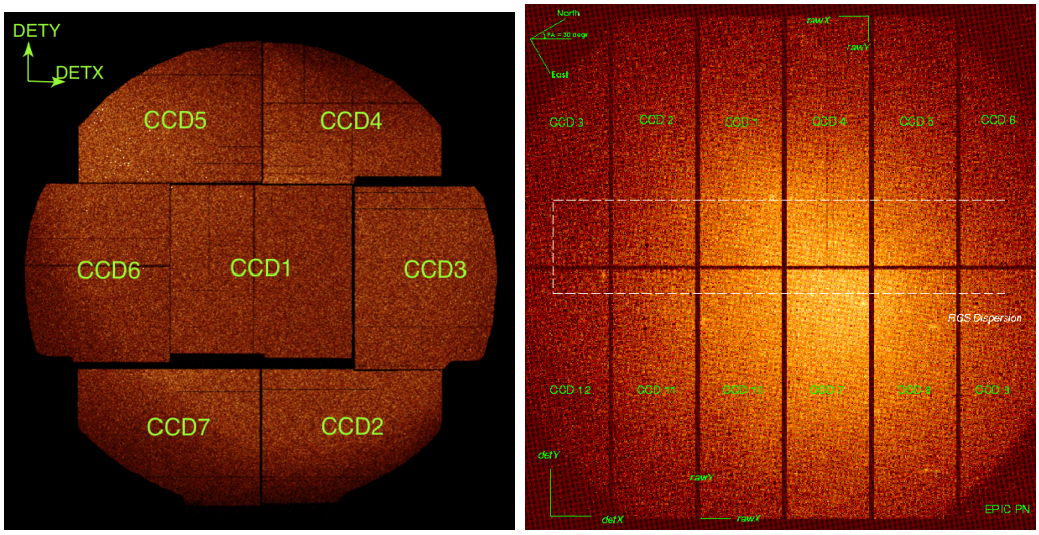

Figure A.1: Layout of the EPIC MOS (left panel) and pn (right panel) camera as displayed in SAS (Gabriel et al., 2004), showing the detector coordinates DETX/DETY and for the pn camera even the orientation of the CCD-specific RAWX/RAWY axes.

A.1.1 EPIC filters and effective area

The most important improvement of *XMM-Newton* with respect of the previous imaging X-ray observatories is the large collecting area (see left panel Fig. A.2). At low energies, the effective area is limited both by the drop in the CCD quantum efficiency and by the presence of filters. At higher energies, the effect of the filters becomes negligible, and the effective area is instead determined by the detector quantum efficiency. For the MOS-CCDs, the quantum efficiency decreases sharply above 10 keV, while the pn detector maintains a higher quantum efficiency up to 12 keV.

The effective area of the mirrors varies even with the off-axis angle. As the off-axis angle increases, a smaller fraction of photons entering the telescope reach the focal plane (this effect is known as vignetting). In the XMM-Newton telescopes, vignetting manifests itself as a decrease in effective area with increasing off-axis angle, as illustrated for several photon energies in the right panel of Fig. A.2. The EPIC CCDs are sensitive not only to X-ray photons, but also to IR, visible, and UV light. To reduce the contamination from this low energy radiation, each EPIC camera is equipped with a set of three filters with different thickness: thick, medium, and thin. These filters, however, partially absorb low energy X-rays as well, and therefore, to minimize the reduction of the effective area, the thicker ones should be applied only in case of bright optical targets.

A.1.2 The EPIC background

The EPIC background consists of three main components: the Cosmic X-ray Background (CXB), a nearly uniform emission produced by the integrated contribution of numerous unresolved extragalactic sources (mainly active galactic nuclei); the instrumental background, which includes detector noise (important below ∼300 eV);

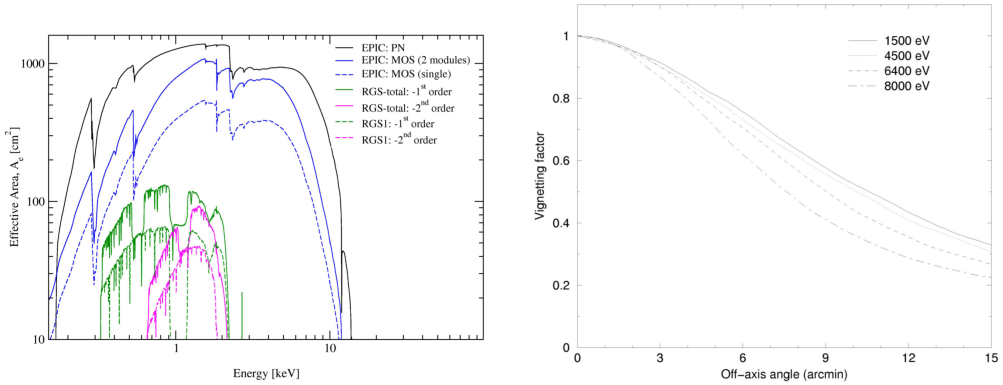

Figure A.2: Left panel: Net effective area of EPIC and RGS, shown on a logarithmic scale. Right panel: Vignetting factor as a function of off-axis angle for the EPIC-pn camera at 1.5, 4.5, 6.4 and 8.0 keV. Figures from XMM-Newton Science Operations Centre (SOC) (2025).

and the particle-induced background. The latter can be further divided into two distinct components: a highly variable flaring component, caused by soft protons of solar origin that are focused by the X-ray mirrors and may sometimes be entirely absent, and a more stable component produced by interactions between high-energy cosmic rays (with energies exceeding several hundred MeV) and the materials of the spacecraft and detectors, generating secondary particles and fluorescence lines.

Understanding the different background contributions is crucial for accurate data analysis, as they affect both the spectral and imaging sensitivity of the EPIC instruments. The flaring soft-proton background is strongly time-variable and is usually filtered out through light-curve screening, at the expense of a significant reduction of the available exposure time. The background component induced by higher energy particles varies on longer timescales, mainly due to the 11-year Solar Cycle, and can therefore be estimated from exposures taken with the filter wheel in closed position or from the external regions of the MOS cameras which are not directly exposed to the sky (out-of-field-of-view events).

A.2 Swift

The *Neil Gehrels Swift Observatory* (Gehrels et al., 2004), launched on November 20, 2004, is a NASA mission developed in collaboration with the Italian Space Agency (ASI) and the United Kingdom Space Agency (UKSA). It was specifically designed for the rapid detection and multi-wavelength follow-up of GRBs, marking a new era in time-domain astrophysics.

The satellite has a total mass of $\sim$ 1500 kg, measures 5.6 m in length with the solar panels deployed, and it operates in a low Earth orbit. *Swift* carries three co-aligned telescopes that provide simultaneous coverage over a wide energy range, from hard X-rays to the optical/UV domain:

- The Burst Alert Telescope (BAT; Krimm et al. 2013) detects GRBs and provides their sky coordinates with arcminute accuracy in the 15–150 keV energy

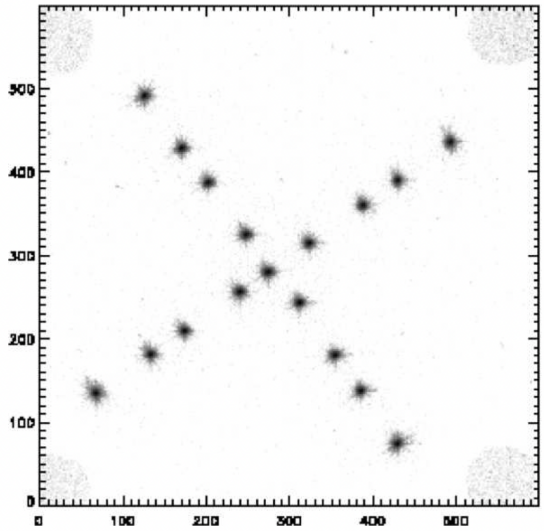

Figure A.3: XRT's PSF at different on-axis and off-axis positions over the full $23.6' \times 23.3'$ FoV.

range. It has a coded aperture imaging instrument that provides a large field of view of about 1.4 sr, enabling the rapid localization of transient events.

- The X-Ray Telescope (XRT; Burrows et al. 2005) performs follow-up observations in the 0.2–10 keV band. It consists of a grazing incidence Wolter I (paraboloid-hyperboloid) mirror assembly coupled with a front-illuminated MOS CCD detector (a single unit of the same chips used in the EPIC MOS cameras on-board the *XMM-Newton* Mission).

- The Ultraviolet–Optical Telescope (UVOT; Roming et al. 2005) observes in the 1700–6500 Å range. It provides photometry and imaging in seven filters (UVW2, UVM2, UVW1, U, B, V, and White) with a typical angular resolution of 2.5″ (FWHM).

The key innovation of *Swift* lies in its rapid slewing capability: once the BAT detects a GRB, the spacecraft autonomously points the narrow-field instruments (XRT and UVOT) toward the burst position. XRT localize GRBs with an accuracy of a few arcseconds within ten seconds of target acquisition for a typical event, and is able to observe their X-ray counterparts starting 60–80 seconds after the burst detection, continuing the monitoring for several days to weeks.

A.2.1 The X-ray telescope

The XRT is a focusing X-ray telescope with a 120 cm^2 effective area, 23.6′ FoV, 15″ resolution (half-power diameter, HPD) at 1.5 keV and – at the launch – an energy resolution of about ∼190 eV at 10 keV and of ∼50 eV at 0.1 keV. The mirror PSF at different positions is shown in Fig. A.3.

The XRT operates in four main modes. In Imaging Mode, the instrument produces an integrated image that measures the total energy deposited per pixel; this

mode does not permit spectroscopy. Photodiode Mode provides very high timing accuracy (timing resolution of 0.14 ms) for rapidly varying flux from a bright source, and permits spectroscopy. Windowed Timing Mode offers a timing resolution of 2.2 ms together with one-dimensional positional information and allows spectroscopy for sources with fluxes below about $1.4 \times 10^{-8}\,\mathrm{erg\,cm^{-2}\,s^{-1}}$. Finally, Photon-Counting Mode enables full spectral and spatial information for sources with fluxes between 8×10^{-14} and $3 \times 10^{-11}\,\mathrm{erg\,cm^{-2}\,s^{-1}}$; however, pile-up becomes significant for sources brighter than 0.5 counts per second.

In XRT, the background is dominated by the cosmic X-ray background and instrumental background which consist of "bad pixels" that produce leakage current, and a minor particle-induced component, as its low-Earth orbit exposes it to a much lower flux of charged particles.

A.3 Chandra

The *Chandra X-ray Observatory* (Weisskopf et al., 2002) is a NASA mission launched on July 23, 1999. It was designed to provide order-of-magnitude advances over previous X-ray astronomy missions with regard to spatial and spectral resolution.

The observatory orbits Earth in an elliptical orbit, in mid-2024, the orbit had an apogee altitude of approximately 145,000 km and a perigee altitude of about 2,350 km. The orbit ensures high observing efficiency, with the satellite spending about 70% of its time well above the Earth's radiation belts. The long orbital period of 63.5 hours enables uninterrupted observations of up to ∼180 ks in a single orbit.

Chandra hosts a single, high-precision X-ray telescope consisting of four pairs of Wolter I mirrors, with the largest mirror having a diameter of 1.2 m and a focal length of 10 m. This optical system, known as the High Resolution Mirror Assembly (HRMA), was designed to deliver images with a spatial resolution of $0.5''$ and to concentrate more than 85% of the energy at 0.277 keV within a $1''$ diameter. The HRMA PSF, however, varies appreciably with the source position within the telescope's field of view. The PSF broadens for off-axis sources, and noticeable image distortion occurs. This distortion arises from the inherent aberrations of the Wolter I design and from the differing focal surfaces of the four mirror pairs. The increase in image size with off-axis angle is most pronounced for the inner mirror shells, and therefore becomes more significant at higher X-ray energies.

The focal plane hosts two main scientific instruments:

- The Advanced CCD Imaging Spectrometer (ACIS; Garmire et al. 2003) provides imaging and moderate-resolution spectroscopy. It consists of ten CCDs arranged in two arrays: ACIS-I (a 4–chips array for imaging and spectrometry, Fig. A.4) and ACIS-S (a 6 chips–array which can be used for imaging spectrometry and also for high-resolution spectroscopy in conjunction with the HETG grating, Fig. A.4). The CCDs operate over the 0.2–10 keV energy band. As for *XMM-Newton*, since the CCDs are sensitive even to optical radiation, blocking filter are placed between the chips and the HRMA. The main parameters of ACIS are summarized in Table A.2. The effective area value reported correspond to the one at the beginning of the mission (Cycle 1);

Table A.2: ACIS main parameters.

CCD format	1024 x 1024 pixels
Pixel size	$0.4920''$
On-axis effective Area (at Cycle 1)	$110\,\mathrm{cm}^2$ @ 0.5 keV
	$600\,\mathrm{cm}^2$ @ 1.5 keV
	$40\,\mathrm{cm}^2$ @ 8.0 keV
Time resolution	2.85 ms – 3.2 s
Sensitivity	$4 \times 10^{-15}\mathrm{erg\,cm^{-2}\,s^{-1}}$ in $10^4\,\mathrm{s}$

however, a gradual decrease in the ACIS effective area at energies below 2 keV has been observed since launch. This decline is attributed to the progressive build-up of out-gassed contaminants on the cold optical blocking filters.

- The High Resolution Camera (HRC; Murray et al. 2000) is a microchannel plate detector optimized for imaging and timing, covering the 0.08–10 keV band. It provides a spectral resolution $\Delta E/E = 1$ at 1 keV and a timing accuracy of 16 μs. The HRC operates in two configurations: HRC-I, optimized for wide-field imaging, and HRC-S, used primarily as the readout detector for grating spectroscopy.

A.3.1 ACIS Background

The ACIS background, as for *XMM-Newton*, is composed of three main components: the Cosmic X-ray Background (CXB), the particle-induced background, and the instrumental background (which includes read-out artifacts, also known as out-of-time events). The particle-induced background originates from the interaction of high-energy charged particles with the spacecraft and the detectors. This component includes a relatively stable quiescent background, produced by cosmic rays and their secondary particles, and a highly variable flaring component caused by soft protons of solar origin that are scattered toward the focal plane by the HRMA mirrors, despite the presence of magnetic deflectors on board *Chandra*.

Between September 2002 and June 2012, a series of observations were performed with ACIS in the stowed position, where the detector was shielded from the sky by the SIM structure[2]. These observations enabled the characterization of the non-celestial component of the X-ray background. In addition, during July–September 2001, Chandra conducted several short observations of the dark Moon, which completely blocks the cosmic X-ray background. The spectra obtained from the dark Moon and the stowed configurations were found to be indistinguishable. Thus, the

[2]The Science Instrument Module (SIM) is a movable structure that positions the focal-plane instruments (ACIS or HRC) into or out of the focal position of the telescope.

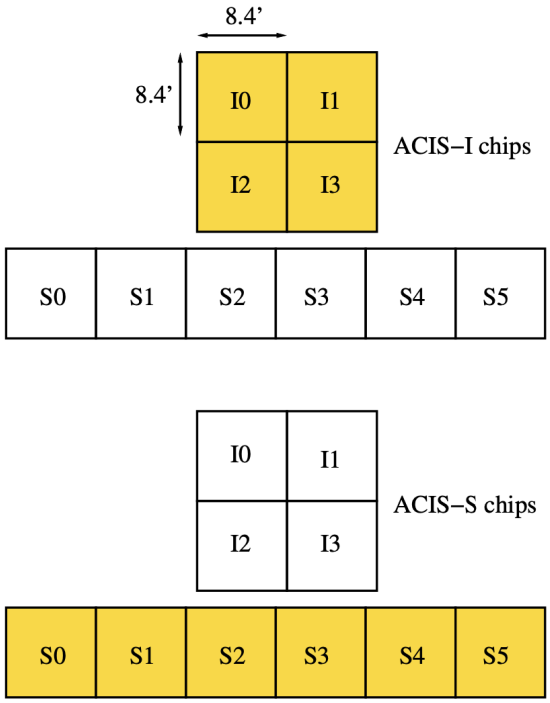

Figure A.4: Schematic view of the ACIS focal plane (not to scale). The ACIS-I array comprises chips I0-I3 (shaded in the upper panel), while the ACIS-S array includes chips S0-S5 (shaded in the lower panel). Figure from the *Chandra* Proposers' Observatory Guide.

ACIS-stowed background is a good representation of the quiescent non-X-ray background in the normal focal position and can be used for science observations.

To support data analysis, the Chandra X-ray Center combined a set of deep, source-free, flare-free exposures (including all components of the background) into background event files corresponding to different time periods (commonly referred to as "blank-sky" dataset).

A.3.2 High-resolution spectroscopy with *Chandra*

High-resolution spectroscopy is achieved through two transmission grating assemblies that can be inserted into the optical path:

- The High Energy Transmission Grating (HETG, Canizares et al. 2005) is used with ACIS-S and covers the 0.4–10 keV energy range.
- The Low Energy Transmission Grating (LETG, Brinkman et al. 2000) is typically used with HRC-S and operates over 0.08–2 keV, achieving a resolving power up to ~ 2000 at 0.5 keV.

High Energy Transmission Grating

The HETG operates in conjunction with the HRMA and a focal-plane imager; together, they form the High-Energy Transmission Grating Spectrometer (HETGS). This instrument provides a resolving power $E/\Delta E$ of up to ~ 1000 at 1 keV. It comprises two types of gratings–the High Energy Grating (HEG) and the Medium Energy Grating (MEG)–that disperse photons into multiple diffraction orders (±1,±2,±3), enabling precise energy calibration and order sorting via the CCD energy resolution. The two grating assemblies are oriented with their rulings at different angles, causing the dispersed spectra from the HEG and MEG to intersect in a shallow "X" pattern (Fig. A.5) centered at the undispersed (zeroth-order) position.

Pile-up can also occur in dispersed spectra, most commonly in the first-order spectra of bright continuum sources. This effect is typically most pronounced in the MEG first-order spectrum near the iridium edge at 2 keV, where the HETGS effective area reaches its maximum. Failure to correct for pile-up may introduce an artificial absorption edge in the data.

The spectral resolution increases approximately linearly with the diffraction order ($R_m \simeq mR_1$), as higher orders produce a greater angular dispersion. However, the diffracted intensity decreases rapidly with increasing m, making first-order spectra the most commonly used for scientific analysis.

Instrumental features near the Si K edge

In previous studies (Zeegers et al., 2019; Rogantini et al., 2019; Rogantini et al., 2020), an instrumental feature near the Si K absorption edge (at 6.742 Å) was consistently observed in all sources analyzed with *Chandra*/HETGS, with the notable exception of the +1 order MEG spectra, which did not display the emission peak. Among the spectral orders used in these studies, the +1 MEG is the only one that

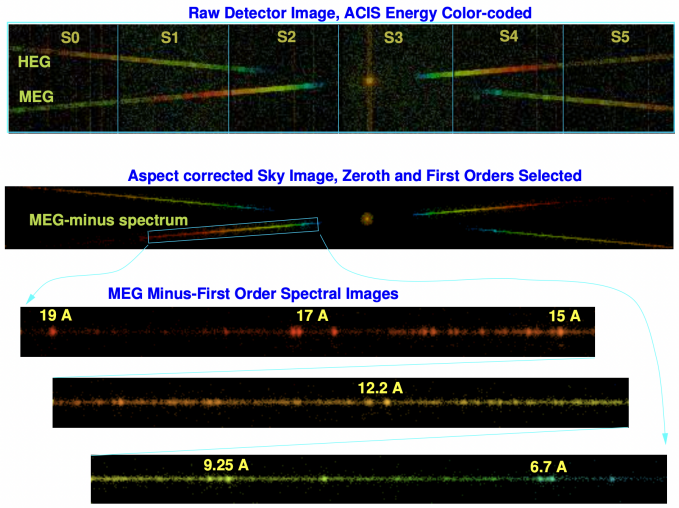

Figure A.5: HETGS observation of Capella (ObsID 1318). Top panel: Image of detected events in the ACIS-S detector. The bright zeroth-order image is visible on CCD S3 and shows a vertical frame-transfer streak. Diffracted photons form a shallow X-shaped pattern corresponding to the HEG and MEG dispersion axes. The apparent broadening of the images is due to spacecraft dither. Middle panel: Aspect-corrected image after applying selections to retain only valid zeroth- and first-order events. Bottom panels: Expanded views of the MEG-1 (minus-first-order) spectrum, showing prominent emission lines, which are clearly resolved. Figure from Canizares et al. (2005).

does not intersect the front-illuminated CCDs in the silicon region. This instrumental feature, detailed in a *Chandra* calibration memorandum[3], actually consists of two narrow emission lines, one at 6.742 Å and another at 6.714 Å. These lines are believed to originate from fluorescence in the SiO_2 gate structure present in the front-illuminated CCDs, likely induced by the interaction of X-rays with the detector material.

We also note here that the only other HETG spectral order falling on a back-illuminated chip near the Si edge is the MEG -3, which falls on the S1 CCD. As expected, this order does not exhibit the spurious emission lines, further supporting the hypothesis that their formation is linked to the front-illuminated architecture of the detector. This issue is discussed in more detail in Chapter 5, where the spectral region around the Si K edge is analyzed in depth.

[3] `https://space.mit.edu/CXC/calib/hetg_user.html`

Acknowledgments

First and foremost, I would like to thank my supervisors.

Andrea Tiengo, thank you for your guidance, patience, and for always believing in my abilities – even when I doubted them myself. Working with you has been an inspiration, and your trust has constantly motivated me to do better. I also had a lot of fun, thank you again.

Paolo Esposito, thank you for your guidance and for always pushing me to improve and refine my work. It has been truly appreciated.

Elisa Costantini and Sacha Zeegers, working with you was both a pleasure and a lot of fun. I learned so much from you.

Alla mia famiglia: mamma, papá, mia sorella e i miei fratelli. Grazie per aver sempre creduto in me, anche nei momenti in cui non ci credevo nemmeno io.

Ad Andrea (Gem), per essere stato il miglior "segretario" esistente. Grazie per avermi sopportato, quando ascoltavo troppo Angelina Mango (grazie anche ad Angelina!), durante la settimana di Sanremo, e soprattutto durante il giorno peggiore di tutti – quando Ciro Immobile ha lasciato la Lazio. Abbiamo riso un sacco.

Ad Alberto ed Eugenia, per aver condiviso con me tutto il percorso.

To the whole CARISMA group, in particular: Marco, Alessandro, Laura (grazie per avermi portata da Crust!), Natalia, Ivana, Milan, Tan, Elisa, Luigi, Teresa, Izabella, Gabriel, Savino, Marta, Priyadarshi, Angela, and Victor (thanks for my first kebab, you had right I will always remember it). Thank you for the laughs, the coffee breaks, and for turning every random day into something worth remembering.

Special thanks to Elisa, for introducing me to the magical world of the FantaForum, and for being my first and only guest in the Netherlands.

Arianna, grazie per avermi fatto "scoprire" la Sardegna e l'uncinetto, e per essere sempre pronta ad ospitarmi – significa davvero tanto per me.

To Riccardo, Leonardo, Carlotta, Marta, Letizia, Maria, Andrea, Giada, Elisabetta, Irene, and Anna – for the laughs in the PhD room and the endless supply of Asian food and good vibes.

Sara (Bor), per avermi ospitato a Pavia le prime settimane quando non conoscevo nessuno, e per le chiacchiere davanti alle crepes al cioccolato.

Thanks to all the people I met in the Netherlands. A Giulia, grazie per esserci come se ci conoscessimo da sempre, anche se non è così.

Ho letto da qualche parte che le amicizie che durano più di sette anni sono destinate a rimanere per sempre. Se è vero, allora siamo a posto.
A Lu, grazie per le chiacchiere e le serie TV a distanza, presenza costante qualsiasi cosa accada.
A Miki, la mia amica e compagna di laboratorio dal primissimo giorno di università, con cui ho condiviso molto più di esperimenti e appunti, e che è diventata una di quelle persone senza cui questo percorso non sarebbe stato lo stesso.

"You never think that the last time is the last time. You think there will be more. You think you have forever, but you don't." – Meredith Grey

This thesis was produced while attending the PhD Program in Space Science and Technology at the University of Trento, Cycle XXXVIII, with the support of a scholarship financed by Ministerial Decree No. 351 of 9 April 2022, based on the NRRP – funded by the European Union – NextGenerationEU – Mission 4 "Education and Research", Component 1 "Enhancement of the offer of educational services: from nurseries to universities", Investment 4.1 "Extension of the number of research doctorates and innovative doctorates for public administration and cultural heritage."

Bibliography

Adams, F. C. (2010). The Birth Environment of the Solar System. *Annual Review of Astronomy and Astrophysics*, 48:47–85.

Akaike, H. (1974). A new look at the statistical model identification. *IEEE Transactions on Automatic Control*, 19:716–723.

Akeson, R., Armus, L., Bachelet, E., Bailey, V., Bartusek, L., Bellini, A., Benford, D., Bennett, D., Bhattacharya, A., Bohlin, R., Boyer, M., Bozza, V., Bryden, G., Calchi Novati, S., Carpenter, K., Casertano, S., Choi, A., Content, D., Dayal, P., Dressler, A., Doré, O., Fall, S. M., Fan, X., Fang, X., Filippenko, A., Finkelstein, S., Foley, R., Furlanetto, S., Kalirai, J., Gaudi, B. S., Gilbert, K., Girard, J., Grady, K., Greene, J., Guhathakurta, P., Heinrich, C., Hemmati, S., Hendel, D., Henderson, C., Henning, T., Hirata, C., Ho, S., Huff, E., Hutter, A., Jansen, R., Jha, S., Johnson, S., Jones, D., Kasdin, J., Kelly, P., Kirshner, R., Koekemoer, A., Kruk, J., Lewis, N., Macintosh, B., Madau, P., Malhotra, S., Mandel, K., Massara, E., Masters, D., McEnery, J., McQuinn, K., Melchior, P., Melton, M., Mennesson, B., Peeples, M., Penny, M., Perlmutter, S., Pisani, A., Plazas, A., Poleski, R., Postman, M., Ranc, C., Rauscher, B., Rest, A., Roberge, A., Robertson, B., Rodney, S., Rhoads, J., Rhodes, J., Ryan, Jr., R., Sahu, K., Sand, D., Scolnic, D., Seth, A., Shvartzvald, Y., Siellez, K., Smith, A., Spergel, D., Stassun, K., Street, R., Strolger, L.-G., Szalay, A., Trauger, J., Troxel, M. A., Turnbull, M., van der Marel, R., von der Linden, A., Wang, Y., Weinberg, D., Williams, B., Windhorst, R., Wollack, E., Wu, H.-Y., Yee, J., and Zimmerman, N. (2019). The Wide Field Infrared Survey Telescope: 100 Hubbles for the 2020s. *arXiv e-prints*, page arXiv:1902.05569.

Allamandola, L. J., Tielens, A. G. G. M., and Barker, J. R. (1985). Polycyclic aromatic hydrocarbons and the unidentified infrared emission bands: auto exhaust along the milky way. *The Astrophysical Journal Letter*, 290:L25–L28.

An, Z.-H., Antier, S., Bi, X.-Z., Bu, Q.-C., Cai, C., Cao, X.-L., Camisasca, A.-E., Chang, Z., Chen, G., Chen, L., Chen, T.-X., Chen, W., Chen, Y.-B., Chen, Y., Chen, Y.-P., Coughlin, M. W., Cui, W.-W., Dai, Z.-G., Hussenot-Desenonges, T., Du, Y.-Q., Du, Y.-Y., Du, Y.-F., Fan, C.-C., Frontera, F., Gao, H., Gao, M., Ge, M.-Y., Gong, K., Gu, Y.-D., Guan, J., Guo, D.-Y., Guo, Z.-W., Guidorzi, C., Han, D.-W., He, J.-J., He, J.-W., Hou, D.-J., Huang, Y., Huo, J., Ji, Z., Jia, S.-M., Jiang, W.-C., Kann, D. A., Klotz, A., Kong, L.-D., Lan, L., Li, A., Li, B., Li, C.-Y., Li, C.-K., Li, G., Li, M.-S., Li, T.-P., Li, W., Li, X.-B., Li, X.-Q., Li,

X.-F., Li, Y.-G., Li, Z.-W., Liang, J., Liang, X.-H., Liao, J.-Y., Lin, L., Liu, C.-Z., Liu, H.-X., Liu, H.-W., Liu, J.-C., Liu, X.-J., Liu, Y.-Q., Liu, Y.-R., Lu, F.-J., Lu, H., Lu, X.-F., Luo, Q., Luo, T., Ma, B.-Y., Ma, F.-L., Ma, R.-C., Ma, X., Maccary, R., Mao, J.-R., Meng, B., Nie, J.-Y., Orlandini, M., Ou, G., Peng, J.-Q., Peng, W.-X., Qiao, R., Qu, J.-L., Ren, X.-Q., Shi, J.-Y., Shi, Q., Song, L.-M., Song, X.-Y., Su, J., Sun, G.-X., Sun, L., Sun, X.-L., Tan, W.-J., Tan, Y., Tao, L., Tuo, Y.-L., Turpin, D., Wang, J.-Z., Wang, C., Wang, C.-W., Wang, H.-J., Wang, H., Wang, J., Wang, L.-J., Wang, P.-J., Wang, P., Wang, W.-S., Wang, X.-Y., Wang, X.-L., Wang, Y.-S., Wang, Y., Wen, X.-Y., Wu, B.-B., Wu, B.-Y., Wu, H., Xiao, S.-H., Xiao, S., Xiao, Y.-X., Xie, S.-L., Xiong, S.-L., Xiong, S.-L., Xu, D., Xu, H., Xu, Y.-J., Xu, Y.-B., Xu, Y.-C., Xu, Y.-P., Xue, W.-C., Yang, S., Yang, Y.-J., Yang, Z.-X., Ye, W.-T., Yi, Q.-B., Yi, S.-X., Yin, Q.-Q., You, Y., Yu, Y.-W., Yu, W., Yu, W.-H., Zeng, M., Zhang, B., Zhang, B.-B., Zhang, D.-L., Zhang, F., Zhang, H.-M., Zhang, J., Zhang, L., Zhang, P., Zhang, P., Zhang, S., Zhang, S.-N., Zhang, W.-C., Zhang, X.-F., Zhang, X.-L., Zhang, Y.-Q., Zhang, Y.-T., Zhang, Y.-F., Zhang, Y.-H., Zhang, Z., Zhao, G.-Y., Zhao, H.-S., Zhao, H.-Y., Zhao, Q.-X., Zhao, S.-J., Zhao, X.-Y., Zhao, X.-F., Zhao, Y., Zheng, C., Zheng, S.-J., Zhou, D.-K., Zhou, X., and Zhu, X.-C. (2023). Insight-hxmt and gecam-c observations of the brightest-of-all-time grb 221009a.

Andrae, R., Fouesneau, M., Sordo, R., Bailer-Jones, C. A. L., Dharmawardena, T. E., Rybizki, J., De Angeli, F., Lindstrøm, H. E. P., Marshall, D. J., Drimmel, R., Korn, A. J., Soubiran, C., Brouillet, N., Casamiquela, L., Rix, H.-W., Abreu Aramburu, A., Álvarez, M. A., Bakker, J., Bellas-Velidis, I., Bijaoui, A., Brugaletta, E., Burlacu, A., Carballo, R., Chaoul, L., Chiavassa, A., Contursi, G., Cooper, W. J., Creevey, O. L., Dafonte, C., Dapergolas, A., de Laverny, P., Delchambre, L., Demouchy, C., Edvardsson, B., Frémat, Y., Garabato, D., García-Lario, P., García-Torres, M., Gavel, A., Gomez, A., González-Santamaría, I., Hatzidimitriou, D., Heiter, U., Jean-Antoine Piccolo, A., Kontizas, M., Kordopatis, G., Lanzafame, A. C., Lebreton, Y., Licata, E. L., Livanou, E., Lobel, A., Lorca, A., Magdaleno Romeo, A., Manteiga, M., Marocco, F., Mary, N., Nicolas, C., Ordenovic, C., Pailler, F., Palicio, P. A., Pallas-Quintela, L., Panem, C., Pichon, B., Poggio, E., Recio-Blanco, A., Riclet, F., Robin, C., Santoveña, R., Sarro, L. M., Schultheis, M. S., Segol, M., Silvelo, A., Slezak, I., Smart, R. L., Süveges, M., Thévenin, F., Torralba Elipe, G., Ulla, A., Utrilla, E., Vallenari, A., van Dillen, E., Zhao, H., and Zorec, J. (2023). Gaia Data Release 3. Analysis of the Gaia BP/RP spectra using the General Stellar Parameterizer from Photometry. *Astronomy and Astrophysics*, 674:A27.

Arendt, R. G., Odegard, N., Weiland, J. L., Sodroski, T. J., Hauser, M. G., Dwek, E., Kelsall, T., Moseley, S. H., Silverberg, R. F., Leisawitz, D., Mitchell, K., Reach, W. T., and Wright, E. L. (1998). The COBE Diffuse Infrared Background Experiment Search for the Cosmic Infrared Background. III. Separation of Galactic Emission from the Infrared Sky Brightness. *The Astrophysical Journal*, 508(1):74–105.

Arnaud, K. A. (1996). XSPEC: The First Ten Years. In Jacoby, G. H. and Barnes,

J., editors, *Astronomical Data Analysis Software and Systems V*, volume 101 of *Astronomical Society of the Pacific Conference Series*, page 17.

Bandyopadhyay, R. M., Shahbaz, T., Charles, P. A., and Naylor, T. (1999). Infrared spectroscopy of low-mass x-ray binaries – ii. *Monthly Notices of the Royal Astronomical Society*, 306:417–426.

Barnes, D. G., Staveley-Smith, L., de Blok, W. J. G., Oosterloo, T., Stewart, I. M., Wright, A. E., Banks, G. D., Bhathal, R., Boyce, P. J., Calabretta, M. R., Disney, M. J., Drinkwater, M. J., Ekers, R. D., Freeman, K. C., Gibson, B. K., Green, A. J., Haynes, R. F., te Lintel Hekkert, P., Henning, P. A., Jerjen, H., Juraszek, S., Kesteven, M. J., Kilborn, V. A., Knezek, P. M., Koribalski, B., Kraan-Korteweg, R. C., Malin, D. F., Marquarding, M., Minchin, R. F., Mould, J. R., Price, R. M., Putman, M. E., Ryder, S. D., Sadler, E. M., Schröder, A., Stootman, F., Webster, R. L., Wilson, W. E., and Ye, T. (2001). The HI Parkes All Sky Survey: southern observations, calibration and robust imaging. *Monthly Notices of the Royal Astronomical Society*, 322(3):486–498.

Bland-Hawthorn, J. and Gerhard, O. (2016). The Galaxy in Context: Structural, Kinematic, and Integrated Properties. *Annual Review of Astronomy and Astrophysics*, 54:529–596.

Bohlin, R. C., Savage, B. D., and Drake, J. F. (1978). A survey of interstellar H I from Lalpha absorption measurements. II. *The Astrophysical Journal*, 224:132–142.

Bohren, C. F. (2010). What did Kramers and Kronig do and how did they do it? *European Journal of Physics*, 31(3):573–577.

Bradt, H. (2004). *Astronomy Methods: A Physical Approach to Astronomical Observations*.

Brinkman, B. C., Gunsing, T., Kaastra, J. S., van der Meer, R., Mewe, R., Paerels, F. B., Raassen, T., van Rooijen, J., Braeuninger, H. W., Burwitz, V., Hartner, G. D., Kettenring, G., Predehl, P., Drake, J. J., Johnson, C. O., Kenter, A. T., Kraft, R. P., Murray, S. S., Ratzlaff, P. W., and Wargelin, B. J. (2000). Description and performance of the low-energy transmission grating spectrometer on board Chandra. In Truemper, J. E. and Aschenbach, B., editors, *X-Ray Optics, Instruments, and Missions III*, volume 4012 of *Society of Photo-Optical Instrumentation Engineers (SPIE) Conference Series*, pages 81–90.

Burnham, K. and Anderson, D. (2002). *Model selection and Multimodel Inference: a Pratical Information-theoretic Approach, 2ed.* Springer, Berlin.

Burns, E., Svinkin, D., Fenimore, E., Kann, D. A., FernÃąndez, J. F. A., Frederiks, D., Hamburg, R., Lesage, S., Temiraev, Y., Tsvetkova, A., Bissaldi, E., Briggs, M. S., Dalessi, S., Dunwoody, R., Fletcher, C., Goldstein, A., Hui, C. M., Hristov, B. A., Kocevski, D., Lysenko, A. L., Mailyan, B., Mangan, J., McBreen, S., Racusin, J., Ridnaia, A., Roberts, O. J., Ulanov, M., Veres, P., Wilson-Hodge,

C. A., and Wood, J. (2023). Grb 221009a: The boat. *The Astrophysical Journal Letters*, 946(1):L31.

Burrows, D. N., Hill, J. E., Nousek, J. A., Kennea, J. A., Wells, A., Osborne, J. P., Abbey, A. F., Beardmore, A., Mukerjee, K., Short, A. D. T., Chincarini, G., Campana, S., Citterio, O., Moretti, A., Pagani, C., Tagliaferri, G., Giommi, P., Capalbi, M., Tamburelli, F., Angelini, L., Cusumano, G., Bräuninger, H. W., Burkert, W., and Hartner, G. D. (2005). The Swift X-Ray Telescope. *Space Science Reviews*, 120(3-4):165–195.

Campana, S., Lazzati, D., Perna, R., Grazia Bernardini, M., and Nava, L. (2021). The variable absorption in the X-ray spectrum of GRB 190114C. *Astronomy & Astrophysics*, 649:A135.

Canizares, C. R., Davis, J. E., Dewey, D., Flanagan, K. A., Galton, E. B., Huenemoerder, D. P., Ishibashi, K., Markert, T. H., Marshall, H. L., McGuirk, M., Schattenburg, M. L., Schulz, N. S., Smith, H. I., and Wise, M. (2005). The chandra high-energy transmission grating: Design, fabrication, ground calibration, and 5 years in flight. *Publications of the Astronomical Society of the Pacific*, 117:1144–1171.

Cardelli, J. A., Clayton, G. C., and Mathis, J. S. (1989). The Relationship between Infrared, Optical, and Ultraviolet Extinction. *ApJ*, 345:245.

Casella, P., Altamirano, D., Patruno, A., Wijnands, R., and van der Klis, M. (2008). Discovery of Coherent Millisecond X-Ray Pulsations in Aquila X-1. *apjl*, 674(1):L41.

Cash, W. (1979). Parameter estimation in astronomy through application of the likelihood ratio. *The Astrophysical Journal*, 228:939–947.

Clemens, D. P. (1985). Massachusetts-Stony Brook Galactic plane CO survey: the galactic disk rotation curve. *The Astrophysical Journal*, 295:422–436.

Costantini, E. and Corrales, L. (2022). Interstellar Absorption and Dust Scattering. In Bambi, C. and Sangangelo, A., editors, *Handbook of X-ray and Gamma-ray Astrophysics*, page 40.

Costantini, E. and de Vries, C. P. (2013). Characterizing the chemistry of interstellar dust: the X-ray view . *memsai*, 84:592.

Costantini, E., Pinto, C., Kaastra, J. S., in't Zand, J. J. M., Freyberg, M. J., Kuiper, L., MÃĺndez, M., de Vries, C. P., and Waters, L. B. F. M. (2012). Xmm-newton observation of 4u 1820-30: Broad band spectrum and the contribution of the cold interstellar medium. *Astronomy and Astrophysics*, 539:A32.

Costantini, E., Zeegers, S. T., Rogantini, D., de Vries, C. P., Tielens, A. G. G. M., and Waters, L. B. F. M. (2019). X-ray extinction from interstellar dust. Prospects of observing carbon, sulfur, and other trace elements. *A&A*, 629:A78.

Cruise, M., Guainazzi, M., Aird, J., Carrera, F. J., Costantini, E., Corrales, L., Dauser, T., Eckert, D., Gastaldello, F., Matsumoto, H., Osten, R., Petrucci, P.-O., Porquet, D., Pratt, G. W., Rea, N., Reiprich, T. H., Simionescu, A., Spiga, D., and Troja, E. (2025). The NewAthena mission concept in the context of the next decade of X-ray astronomy. *Nature Astronomy*, 9:36–44.

D'Aì, A., Iaria, R., Di Salvo, T., Riggio, A., Burderi, L., and Robba, N. R. (2014). Chandra x-ray spectroscopy of a clear dip in gx 13+1. *Astronomy and Astrophysics*, 564:A62.

Dame, T. M., Hartmann, D., and Thaddeus, P. (2001). The Milky Way in Molecular Clouds: A New Complete CO Survey. *The Astrophysical Journal*, 547(2):792–813.

Dame, T. M. and Thaddeus, P. (2011). A Molecular Spiral Arm in the Far Outer Galaxy. *The Astrophysical Journal Letters*, 734(1):L24.

Dame, T. M. and Thaddeus, P. (2022). A CO Survey of the Entire Northern Sky. *The Astrophysical Journal Supplement Series*, 262(1):5.

de Plaa, J., Kaastra, J. S., Tamura, T., Pointecouteau, E., Mendez, M., and Peterson, J. R. (2004). X-ray spectroscopy on abell 478 with xmm-newton. *Astronomy and Astrophysics*, 423:49–56.

de Ugarte Postigo, A., Izzo, L., Pugliese, G., Xu, D., Schneider, B., Fynbo, J. P. U., Tanvir, N. R., Malesani, D. B., Saccardi, A., Kann, D. A., Wiersema, K., Gompertz, B. P., Thoene, C. C., Levan, A. J., and Stargate Collaboration (2022). GRB 221009A: Redshift from X-shooter/VLT. *GRB Coordinates Network*, 32648:1.

den Herder, J. W., Brinkman, A. C., Kahn, S. M., Branduardi-Raymont, G., Thomsen, K., Aarts, H., Audard, M., Bixler, J. V., den Boggende, A. J., Cottam, J., Decker, T., Dubbeldam, L., Erd, C., Goulooze, H., Güdel, M., Guttridge, P., Hailey, C. J., Janabi, K. A., Kaastra, J. S., de Korte, P. A. J., van Leeuwen, B. J., Mauche, C., McCalden, A. J., Mewe, R., Naber, A., Paerels, F. B., Peterson, J. R., Rasmussen, A. P., Rees, K., Sakelliou, I., Sako, M., Spodek, J., Stern, M., Tamura, T., Tandy, J., de Vries, C. P., Welch, S., and Zehnder, A. (2001). The Reflection Grating Spectrometer on board XMM-Newton. *Astronomy & Astrophysics*, 365:L7–L17.

Dichiara, S., Gropp, J. D., Kennea, J. A., Kuin, N. P. M., Lien, A. Y., Marshall, F. E., Tohuvavohu, A., Williams, M. A., and Neil Gehrels Swift Observatory Team (2022). Swift J1913.1+1946 a new bright hard X-ray and optical transient. *GRB Coordinates Network*, 32632:1.

Do-Duy, T., Wright, C. M., Fujiyoshi, T., Glasse, A., Siebenmorgen, R., Smith, R., Stecklum, B., and Sterzik, M. (2020). Crystalline silicate absorption at 11.1 μm: ubiquitous and abundant in embedded YSOs and the interstellar medium. *Monthly Notices of the Royal Astronomical Society*, 493(3):4463–4517.

Draine, B. T. (2003). Scattering by Interstellar Dust Grains. II. X-Rays. *The Astrophysical Journal*, 598:1026–1037.

Draine, B. T. (2009). Interstellar Dust Models and Evolutionary Implications. In Henning, T., Grün, E., and Steinacker, J., editors, *Cosmic Dust - Near and Far*, volume 414 of *Astronomical Society of the Pacific Conference Series*, page 453.

Draine, B. T. (2011). *Physics of the Interstellar and Intergalactic Medium*. Princeton Series in Astrophysics. Princeton University Press.

Draine, B. T. and Allaf-Akbari, K. (2006). X-ray scattering by nonspherical grains. i. oblate spheroids. *The Astrophysical Journal*, 652(2):1318–1330.

Dwek, E. (2016). Iron: A Key Element for Understanding the Origin and Evolution of Interstellar Dust. *ApJ*, 825:136.

Dwek, E., Arendt, R. G., Fixsen, D. J., Sodroski, T. J., Odegard, N., Weiland, J. L., Reach, W. T., Hauser, M. G., Kelsall, T., Moseley, S. H., Silverberg, R. F., Shafer, R. A., Ballester, J., Bazell, D., and Isaacman, R. (1997). Detection and Characterization of Cold Interstellar Dust and Polycyclic Aromatic Hydrocarbon Emission, from COBE Observations. *The Astrophysical Journal*, 475(2):565–579.

Edenhofer, G., Zucker, C., Frank, P., Saydjari, A. K., Speagle, J. S., Finkbeiner, D., and Enblin, T. A. (2024). A parsec-scale galactic 3d dust map out to 1.25 kpc from the sun. *Astronomy & Astrophysics*, 685:A82.

Evans, A. (1986). EXAFS studies of interstellar dust. *Monthly Notices of the Royal Astronomical Society*, 223:219–224.

Feng, L. and Fox, D. B. (2010). Could the GRB-supernovae GRB031203 and XRF060218 be cosmic twins? *Monthly Notices of the Royal Astronomical Society*, 404(2):1018–1028.

Flank, A. M., Cauchon, G., Lagarde, P., Bac, S., Janousch, M., Wetter, R., Dubuisson, J. M., Idir, M., Langlois, F., Moreno, T., and Vantelon, D. (2006). LUCIA, a microfocus soft XAS beamline. *Nuclear Instruments and Methods in Physics Research B*, 246(1):269–274.

Fogerty, S., Forrest, W., Watson, D. M., Sargent, B. A., and Koch, I. (2016). Silicate Composition of the Interstellar Medium. *The Astrophysical Journal*, 830(2):71.

Frederiks, D., Golenetskii, S., Aptekar, R., Oleynik, P., Ulanov, M., Svinkin, D., Tsvetkova, A., Lysenko, A., Kozlova, A., and Cline, T. (2016). Konus-Wind observation of GRB 160623A. *GRB Coordinates Network*, 19554:1.

Frederiks, D., Svinkin, D., Lysenko, A. L., Molkov, S., Tsvetkova, A., Ulanov, M., Ridnaia, A., Lutovinov, A. A., Lapshov, I., Tkachenko, A., and Levin, V. (2023). Properties of the extremely energetic grb 221009a from konus-wind and srg/art-xc observations. *The Astrophysical Journal Letters*, 949(1):L7.

Fridriksson, J. K., Homan, J., and Remillard, R. A. (2015). Common patterns in the evolution between the luminous neutron star low-mass x-ray binary subclasses. *The Astrophysical Journal*, 809:52.

Fruscione, A., McDowell, J. C., Allen, G. E., Brickhouse, N. S., Burke, D. J., Davis, J. E., Durham, N., Elvis, M., Galle, E. C., Harris, D. E., Huenemoerder, D. P., Houck, J. C., Ishibashi, B., Karovska, M., Nicastro, F., Noble, M. S., Nowak, M. A., Primini, F. A., Siemiginowska, A., Smith, R. K., and Wise, M. (2006). CIAO: Chandra's data analysis system. In Silva, D. R. and Doxsey, R. E., editors, *Society of Photo-Optical Instrumentation Engineers (SPIE) Conference Series*, volume 6270 of *Society of Photo-Optical Instrumentation Engineers (SPIE) Conference Series*, page 62701V.

Fulton, M. D., Smartt, S. J., Rhodes, L., Huber, M. E., Villar, V. A., Moore, T., Srivastav, S., Schultz, A. S. B., Chambers, K. C., Izzo, L., Hjorth, J., Chen, T. W., Nicholl, M., Foley, R. J., Rest, A., Smith, K. W., Young, D. R., Sim, S. A., Bright, J., Zenati, Y., de Boer, T., Bulger, J., Fairlamb, J., Gao, H., Lin, C. C., Lowe, T., Magnier, E. A., Smith, I. A., Wainscoat, R., Coulter, D. A., Jones, D. O., Kilpatrick, C. D., McGill, P., Ramirez-Ruiz, E., Lee, K. S., Narayan, G., Ramakrishnan, V., Ridden-Harper, R., Singh, A., Wang, Q., Kong, A. K. H., Ngeow, C. C., Pan, Y. C., Yang, S., Davis, K. W., Piro, A. L., Rojas-Bravo, C., Sommer, J., and Yadavalli, S. K. (2023). The Optical Light Curve of GRB 221009A: The Afterglow and the Emerging Supernova. *The Astrophysical Journal Letters*, 946(1):L22.

Gabriel, C., Denby, M., Fyfe, D. J., Hoar, J., Ibarra, A., Ojero, E., Osborne, J., Saxton, R. D., Lammers, U., and Vacanti, G. (2004). The XMM-Newton SAS - Distributed Development and Maintenance of a Large Science Analysis System: A Critical Analysis. In Ochsenbein, F., Allen, M. G., and Egret, D., editors, *Astronomical Data Analysis Software and Systems (ADASS) XIII*, volume 314 of *Astronomical Society of the Pacific Conference Series*, page 759.

Gaia Collaboration, Prusti, T., de Bruijne, J. H. J., Brown, A. G. A., Vallenari, A., Babusiaux, C., Bailer-Jones, C. A. L., Bastian, U., Biermann, M., Evans, D. W., Eyer, L., Jansen, F., Jordi, C., Klioner, S. A., Lammers, U., Lindegren, L., Luri, X., Mignard, F., Milligan, D. J., Panem, C., Poinsignon, V., Pourbaix, D., Randich, S., Sarri, G., Sartoretti, P., Siddiqui, H. I., Soubiran, C., Valette, V., van Leeuwen, F., Walton, N. A., Aerts, C., Arenou, F., Cropper, M., Drimmel, R., Høg, E., Katz, D., Lattanzi, M. G., O'Mullane, W., Grebel, E. K., Holland, A. D., Huc, C., Passot, X., Bramante, L., Cacciari, C., Castañeda, J., Chaoul, L., Cheek, N., De Angeli, F., Fabricius, C., Guerra, R., Hernández, J., Jean-Antoine-Piccolo, A., Masana, E., Messineo, R., Mowlavi, N., Nienartowicz, K., Ordóñez-Blanco, D., Panuzzo, P., Portell, J., Richards, P. J., Riello, M., Seabroke, G. M., Tanga, P., Thévenin, F., Torra, J., Els, S. G., Gracia-Abril, G., Comoretto, G., Garcia-Reinaldos, M., Lock, T., Mercier, E., Altmann, M., Andrae, R., Astraatmadja, T. L., Bellas-Velidis, I., Benson, K., Berthier, J., Blomme, R., Busso, G., Carry, B., Cellino, A., Clementini, G., Cowell, S., Creevey, O., Cuypers, J., Davidson, M., De Ridder, J., de Torres, A., Delchambre, L., Dell'Oro, A., Ducourant, C., Frémat, Y., García-Torres, M., Gosset, E., Halbwachs, J. L., Hambly, N. C., Harrison, D. L., Hauser, M., Hestroffer, D., Hodgkin, S. T., Huckle, H. E., Hutton, A., Jasniewicz, G., Jordan, S., Kontizas, M., Korn, A. J., Lanzafame, A. C.,

Manteiga, M., Moitinho, A., Muinonen, K., Osinde, J., Pancino, E., Pauwels, T., Petit, J. M., Recio-Blanco, A., Robin, A. C., Sarro, L. M., Siopis, C., Smith, M., Smith, K. W., Sozzetti, A., Thuillot, W., van Reeven, W., Viala, Y., Abbas, U., Abreu Aramburu, A., Accart, S., Aguado, J. J., Allan, P. M., Allasia, W., Altavilla, G., Álvarez, M. A., Alves, J., Anderson, R. I., Andrei, A. H., Anglada Varela, E., Antiche, E., Antoja, T., Antón, S., Arcay, B., Atzei, A., Ayache, L., Bach, N., Baker, S. G., Balaguer-Núñez, L., Barache, C., Barata, C., Barbier, A., Barblan, F., Baroni, M., Barrado y Navascués, D., Barros, M., Barstow, M. A., Becciani, U., Bellazzini, M., Bellei, G., Bello García, A., Belokurov, V., Bendjoya, P., Berihuete, A., Bianchi, L., Bienaymé, O., Billebaud, F., Blagorodnova, N., Blanco-Cuaresma, S., Boch, T., Bombrun, A., Borrachero, R., Bouquillon, S., Bourda, G., Bouy, H., Bragaglia, A., Breddels, M. A., Brouillet, N., Brüsemeister, T., Bucciarelli, B., Budnik, F., Burgess, P., Burgon, R., Burlacu, A., Busonero, D., Buzzi, R., Caffau, E., Cambras, J., Campbell, H., Cancelliere, R., Cantat-Gaudin, T., Carlucci, T., Carrasco, J. M., Castellani, M., Charlot, P., Charnas, J., Charvet, P., Chassat, F., Chiavassa, A., Clotet, M., Cocozza, G., Collins, R. S., Collins, P., and Costigan, G. (2016). The Gaia mission. *Astronomy & Astrophysics*, 595:A1.

Galloway, D. K., Muno, M. P., Hartman, J. M., Psaltis, D., and Chakrabarty, D. (2008). Thermonuclear (Type I) X-Ray Bursts Observed by the Rossi X-Ray Timing Explorer. *apjs*, 179(2):360–422.

Garmire, G. P., Bautz, M. W., Ford, P. G., Nousek, J. A., and Ricker, Jr., G. R. (2003). Advanced CCD imaging spectrometer (ACIS) instrument on the Chandra X-ray Observatory. In Truemper, J. E. and Tananbaum, H. D., editors, *X-Ray and Gamma-Ray Telescopes and Instruments for Astronomy.*, volume 4851 of *Society of Photo-Optical Instrumentation Engineers (SPIE) Conference Series*, pages 28–44.

Gastaldello, F., Marelli, M., Molendi, S., Bartalucci, I., Kühl, P., Grant, C. E., Ghizzardi, S., Rossetti, M., De Luca, A., and Tiengo, A. (2022). The Origin of the Unfocused XMM-Newton Background, Its Variability, and Lessons Learned for ATHENA. *The Astrophysical Journal*, 928(2):168.

Gatuzz, E., Gorczyca, T. W., Hasoglu, M. F., Costantini, E., GarcÃŋa, J. A., and Kallman, T. R. (2024). Sulphur x-ray absorption in the local ism. *Monthly Notices of the Royal Astronomical Society*, 527:1648–1655.

Gehrels, N., Chincarini, G., Giommi, P., Mason, K. O., Nousek, J. A., Wells, A. A., White, N. E., Barthelmy, S. D., Burrows, D. N., Cominsky, L. R., Hurley, K. C., Marshall, F. E., Mészáros, P., Roming, P. W. A., Angelini, L., Barbier, L. M., Belloni, T., Campana, S., Caraveo, P. A., Chester, M. M., Citterio, O., Cline, T. L., Cropper, M. S., Cummings, J. R., Dean, A. J., Feigelson, E. D., Fenimore, E. E., Frail, D. A., Fruchter, A. S., Garmire, G. P., Gendreau, K., Ghisellini, G., Greiner, J., Hill, J. E., Hunsberger, S. D., Krimm, H. A., Kulkarni, S. R., Kumar, P., Lebrun, F., Lloyd-Ronning, N. M., Markwardt, C. B., Mattson, B. J., Mushotzky, R. F., Norris, J. P., Osborne, J., Paczynski, B., Palmer, D. M., Park,

H. S., Parsons, A. M., Paul, J., Rees, M. J., Reynolds, C. S., Rhoads, J. E., Sasseen, T. P., Schaefer, B. E., Short, A. T., Smale, A. P., Smith, I. A., Stella, L., Tagliaferri, G., Takahashi, T., Tashiro, M., Townsley, L. K., Tueller, J., Turner, M. J. L., Vietri, M., Voges, W., Ward, M. J., Willingale, R., Zerbi, F. M., and Zhang, W. W. (2004). The Swift Gamma-Ray Burst Mission. *The Astrophysical Journal*, 611(2):1005–1020.

Giacconi, R., Gursky, H., Paolini, F. R., and Rossi, B. B. (1962). Evidence for x Rays From Sources Outside the Solar System. *Physical Review Letters*, 9(11):439–443.

Gibb, E. L., Whittet, D. C. B., Boogert, A. C. A., and Tielens, A. G. G. M. (2004). Interstellar Ice: The Infrared Space Observatory Legacy. *The Astrophysical Journal Supplement Series*, 151(1):35–73.

Gotz, D., Mereghetti, S., Beck, M., Borkowski, J., and Mowlavi, N. (2003). GRB 031203: a long GRB detected with INTEGRAL. *GRB Coordinates Network*, 2459:1.

Green, G. (2018). dustmaps: A Python interface for maps of interstellar dust. *The Journal of Open Source Software*, 3(26):695.

Green, G. M., Schlafly, E., Zucker, C., Speagle, J. S., and Finkbeiner, D. (2019). A 3D Dust Map Based on Gaia, Pan-STARRS 1, and 2MASS. *The Astrophysical Journal*, 887(1):93.

Hasenberger, B., Forbrich, J., Alves, J., Wolk, S. J., Meingast, S., Getman, K. V., and Pillitteri, I. (2016). Gas absorption and dust extinction towards the Orion Nebula Cluster. *Astronomy and Astrophysics*, 593:A7.

Hasinger, G. and van der Klis, M. (1989). Two patterns of correlated x-ray timing and spectral behaviour in low-mass x-ray binaries. *Astronomy and Astrophysics*, 225:79–96.

Heinz, S., Corrales, L., Smith, R., Brandt, W. N., Jonker, P. G., Plotkin, R. M., and Neilsen, J. (2016). A Joint Chandra and Swift View of the 2015 X-ray Dust-scattering Echo of V404 Cygni. *The Astrophysical Journal*, 825(1):15.

Hensley, B. S. and Draine, B. T. (2021). Observational Constraints on the Physical Properties of Interstellar Dust in the Post-Planck Era. *The Astrophysical Journal*, 906(2):73.

Heyer, M. H., Carpenter, J. M., and Snell, R. L. (2001). The Equilibrium State of Molecular Regions in the Outer Galaxy. *The Astrophysical Journal*, 551(2):852–866.

HI4PI Collaboration:, Ben Bekhti, N., FlÃűer, L., Keller, R., Kerp, J. Lenz, D., Winkel, B., Bailin, J., Calabretta, M. R., Dedes, L., añd Gibson, B. K., F., Haud, U., Janowiecki, S., Kalberla, P. M. W., Lockman, F. J., McC lure-Griffiths, N. M., Murphy, T., Nakanishi, H., Pisano, D. J., and Staveley-Smith, L. (2016). Hi4pi: a full-sky hâĂĽi survey based on ebhis and gassâŃĘ. *Astronomy & Astrophysics*, 594:A116.

Hiltner, W. A. (1949). Polarization of Light from Distant Stars by Interstellar Medium. *Science*, 109(2825):165.

Hirashita, H. and Murga, M. S. (2020). Self-consistent modelling of aromatic dust species and extinction curves in galaxy evolution. *Monthly Notices of the Royal Astronomical Society*, 492(3):3779–3793.

Honma, M., Nagayama, T., and Sakai, N. (2015). Determining dynamical parameters of the milky way galaxy based on high-accuracy radio astrometry. *Publications of the Astronomical Society of Japan*, 67(4):70.

Hou, L. G. and Han, J. L. (2014). The observed spiral structure of the milky way. *Astronomy & Astrophysics*, 569:A125.

Huss, G. and Draine, B. (2007). What can pre-solar grains tell us about the solar nebula? *Highlights of Astronomy*, 14:353–356.

Iaria, R., Di Salvo, T., Burderi, L., Riggio, A., D'A
i, A., and Robba, N. R. (2014). Discovery of periodic dips in the light curve of GX 13+1: the X-ray orbital ephemeris of the source. *A&A*, 561:A99.

Jansen, F., Lumb, D., Altieri, B., Clavel, J., Ehle, M., Erd, C., Gabriel, C., Guainazzi, M., Gondoin, P., Much, R., Munoz, R., Santos, M., Schartel, N., Texier, D., and Vacanti, G. (2001). XMM-Newton observatory. I. The spacecraft and operations. *Astronomy & Astrophysics*, 365:L1–L6.

Jenkins, E. B. (2009). A Unified Representation of Gas-Phase Element Depletions in the Interstellar Medium. *ApJ*, 700:1299–1348.

Johnson, H. L. (1968). Interstellar Extinction. In Middlehurst, B. M. and Aller, L. H., editors, *Nebulae and Interstellar Matter*, page 167.

Jones, A. P. (1997). The Lifecycle of Interstellar Dust. In Pendleton, Y. J., editor, *From Stardust to Planetesimals*, volume 122 of *Astronomical Society of the Pacific Conference Series*, page 97.

Jones, A. P. and Nuth, J. A. (2011). Dust destruction in the ISM: a re-evaluation of dust lifetimes. *Astronomy & Astrophysics*, 530:A44.

Kaastra, J. S. (2017). On the use of c-stat in testing models for x-ray spectra. *Astronomy and Astrophysics*, 605:A51.

Kaastra, J. S., Mewe, R., and Nieuwenhuijzen, H. (1996). Spex: A new code for spectral analysis of x and uv spectra. In Yamashita, K. and Watanabe, T., editors, *UV and X-ray Spectroscopy of Astrophysical and Laboratory Plasmas*, pages 411–414.

Kaastra, J. S., Raassen, A. J. J., de Plaa, J., and Gu, L. (2018). SPEX X-ray spectral fitting package.

Kalberla, P. M. W. and Haud, U. (2015). GASS: The Parkes Galactic All-Sky Survey. Update: improved correction for instrumental effects and new data release. *Astronomy & Astrophysics*, 578:A78.

Kalberla, P. M. W., McClure-Griffiths, N. M., Pisano, D. J., Calabretta, M. R., Ford, H. A., Lockman, F. J., Staveley-Smith, L., Kerp, J., Winkel, B., Murphy, T., and Newton-McGee, K. (2010). GASS: the Parkes Galactic all-sky survey. II. Stray-radiation correction and second data release. *Astronomy & Astrophysics*, 521:A17.

Kann, D. A., Agayeva, S., Aivazyan, V., Alishov, S., Andrade, C. M., Antier, S., Baransky, A., Bendjoya, P., Benkhaldoun, Z., Beradze, S., Berezin, D., Boër, M., Broens, E., Brunier, S., Bulla, M., Burkhonov, O., Burns, E., Chen, Y., Chen, Y. P., Conti, M., Coughlin, M. W., Cui, W. W., Daigne, F., Delaveau, B., Devillepoix, H. A. R., Dietrich, T., Dornic, D., Dubois, F., Ducoin, J. G., Durand, E., Duverne, P. A., Eggenstein, H. B., Ehgamberdiev, S., Fouad, A., Freeberg, M., Froebrich, D., Ge, M. Y., Gervasoni, S., Godunova, V., Gokuldass, P., Gurbanov, E., Han, D. W., Hasanov, E., Hello, P., Hussenot-Desenonges, T., Inasaridze, R., Iskandar, A., Ismailov, N., Janati, A., du Laz, T. J., Jia, S. M., Karpov, S., Kaeouach, A., Kiendrebeogo, R. W., Klotz, A., Kneip, R., Kochiashvili, N., Kunert, N., Lekic, A., Leonini, S., Li, C. K., Li, W., Li, X. B., Liao, J. Y., Logie, L., Lu, F. J., Mao, J., Marchais, D., Ménard, R., Morris, D., Natsvlishvili, R., Nedora, V., Noonan, K., Noysena, K., Orange, N. B., Pang, P. T. H., Peng, H. W., Pellouin, C., Peloton, J., Pradier, T., Pyshna, O., Rajabov, Y., Rau, S., Rinner, C., Rivet, J. P., Romanov, F. D., Rosi, P., Rupchandani, V. A., Serrau, M., Shokry, A., Simon, A., Smith, K., Sokoliuk, O., Soliman, M., Song, L. M., Takey, A., Tillayev, Y., Ramirez, L. M. T., e Melo, I. T., Turpin, D., de Ugarte Postigo, A., Vanaverbeke, S., Vasylenko, V., Vernet, D., Vidadi, Z., Wang, C., Wang, J., Wang, L. T., Wang, X. F., Xiong, S. L., Xu, Y. P., Xue, W. C., Zeng, X., Zhang, S. N., Zhao, H. S., and Zhao, X. F. (2023). GRANDMA and HXMT Observations of GRB 221009A: The Standard Luminosity Afterglow of a Hyperluminous Gamma-Ray Burst-In Gedenken an David Alexander Kann. *The Astrophysical Journal Letters*, 948(2):L12.

Kemper, F., Vriend, W. J., and Tielens, A. G. G. M. (2004). The Absence of Crystalline Silicates in the Diffuse Interstellar Medium. *The Astrophysical Journal*, 609(2):826–837.

Kemper, F., Vriend, W. J., and Tielens, A. G. G. M. (2005). Erratum: "The Absence of Crystalline Silicates in the Diffuse Interstellar Medium" (<A href="/abs/2004ApJ...609..826K">ApJ, 609, 826 [2004]</A>). *The Astrophysical Journal*, 633(1):534–534.

Kennea, J. A., Williams, M., and Swift Team (2022). GRB 221009A: Swift detected transient may be GRB. *GRB Coordinates Network*, 32635:1.

Knacke, R. F. and Thomson, R. K. (1973). Infrared Extinction Cross Sections of Silicate Grains. *Publications of the Astronomical Society of the Pacific*, 85(505):341.

Krimm, H. A., Holland, S. T., Corbet, R. H. D., Pearlman, A. B., Romano, P., Kennea, J. A., Bloom, J. S., Barthelmy, S. D., Baumgartner, W. H., Cummings, J. R., Gehrels, N., Lien, A. Y., Markwardt, C. B., Palmer, D. M., Sakamoto, T., Stamatikos, M., and Ukwatta, T. N. (2013). The Swift/BAT Hard X-Ray Transient Monitor. *The Astrophysical Journal Supplement Series*, 209(1):14.

Kunte, P. K., Durgaprasad, N., Gokhale, G. S., Iyengar, V. S., Manchanda, R. K., and Sreekantan, B. V. (1973). Hard X Rays from the Region of Aquila XR-1. *Nature Physical Science*, 245(142):37–38.

Lallement, R., Vergely, J. L., Babusiaux, C., and Cox, N. L. J. (2022). Updated Gaia-2MASS 3D maps of Galactic interstellar dust. *Astronomy & Astrophysics*, 661:A147.

Lamer, G., Schwope, A. D., Predehl, P., Traulsen, I., Wilms, J., and Freyberg, M. (2021). A giant X-ray dust scattering ring discovered with SRG/eROSITA around the black hole transient MAXI J1348-630. *Astronomy & Astrophysics*, 647:A7.

Lee, J. C. and Ravel, B. (2005). Determining the Grain Composition of the Interstellar Medium with High-Resolution X-Ray Spectroscopy. *The Astrophysical Journal*, 622(2):970–976.

Lee, J. C., Reynolds, C. S., Remillard, R., Schulz, N. S., Blackman, E. G., and Fabian, A. C. (2002). High-Resolution Chandra HETGS and Rossi X-Ray Timing Explorer Observations of GRS 1915+105: A Hot Disk Atmosphere and Cold Gas Enriched in Iron and Silicon. *The Astrophysical Journal*, 567(2):1102–1111.

Lee, J. C., Smith, R. K., Canizares, C. R., Costantini, E., de Vries, C., Drake, J., Dwek, E., Edgar, R., Juett, A. M., Li, A., Lisse, C., Paerels, F., Patnaude, D., Ravel, B., Schulz, N. S., Snow, T. P., Valencic, L. A., Wilms, J., and Xiang, J. (2009). Solid State Astrophysics: Probing Interstellar Dust and Gas Properties with X-rays. In *astro2010: The Astronomy and Astrophysics Decadal Survey*, volume 2010, page 178.

Lesage, S., Veres, P., Briggs, M. S., Goldstein, A., Kocevski, D., Burns, E., Wilson-Hodge, C. A., Bhat, P. N., Huppenkothen, D., Fryer, C. L., Hamburg, R., Racusin, J., Bissaldi, E., Cleveland, W. H., Dalessi, S., Fletcher, C., Giles, M. M., Hristov, B. A., Hui, C. M., Mailyan, B., Malacaria, C., Poolakkil, S., Roberts, O. J., von Kienlin, A., Wood, J., Ajello, M., Arimoto, M., Baldini, L., Ballet, J., Baring, M. G., Bastieri, D., Gonzalez, J. B., Bellazzini, R., Bissaldi, E., Blandford, R. D., Bonino, R., Bruel, P., Buson, S., Cameron, R. A., Caputo, R., Caraveo, P. A., Cavazzuti, E., Chiaro, G., Cibrario, N., Ciprini, S., Orestano, P. C., Crnogorcevic, M., Cuoco, A., Cutini, S., DâĂŹAmmando, F., De Gaetano, S., Di Lalla, N., Di Venere, L., DomÃŋnguez, A., Fegan, S. J., Ferrara, E. C., Fleischhack, H., Fukazawa, Y., Funk, S., Fusco, P., Galanti, G., Gammaldi, V., Gargano, F., Gasbarra, C., Gasparrini, D., Germani, S., Giacchino, F., Giglietto, N., Gill, R., Giroletti, M., Granot, J., Green, D., Grenier, I. A., Guiriec, S., Gustafsson, M., Hays, E., Hewitt, J. W., Horan, D., Hou, X., Kuss, M., Latronico, L., Laviron, A., Lemoine-Goumard, M., Li, J., Liodakis, I., Longo, F., Loparco, F., Lorusso,

L., Lovellette, M. N., Lubrano, P., Maldera, S., Manfreda, A., MartÃŋ-Devesa, G., Mazziotta, M. N., McEnery, J. E., Mereu, I., Meyer, M., Michelson, P. F., Mizuno, T., Monzani, M. E., Morselli, A., Moskalenko, I. V., Negro, M., Nuss, E., Omodei, N., Orlando, E., Ormes, J. F., Paneque, D., Panzarini, G., Persic, M., Pesce-Rollins, M., Pillera, R., Piron, F., Poon, H., Porter, T. A., Principe, G., RainÃš, S., Rando, R., Rani, B., Razzano, M., Razzaque, S., Reimer, A., Reimer, O., Ryde, F., SÃąnchez-Conde, M., Parkinson, P. M. S., Scotton, L., Serini, D., SgrÃš, C., Sharma, V., Siskind, E. J., Spandre, G., Spinelli, P., Tajima, H., Torres, D. F., Valverde, J., Venters, T., Wadiasingh, Z., Wood, K., and Zaharijas, G. (2023). Fermi-gbm discovery of grb 221009a: An extraordinarily bright grb from onset to afterglow. *The Astrophysical Journal Letters*, 952(2):L42.

Li, A. and Draine, B. T. (2001). Infrared Emission from Interstellar Dust. II. The Diffuse Interstellar Medium. *The Astrophysical Journal*, 554(2):778–802.

Lodders, K. (2010). Solar system abundances of the elements. In Goswami, A. and Reddy, B. E., editors, *Principles and Perspectives in Cosmochemistry*, volume 16 of *Astrophysics and Space Science Proceedings*, page 379.

Lombardi, M., Alves, J., and Lada, C. J. (2006). 2MASS wide field extinction maps. I. The Pipe nebula. *Astronomy & Astrophysics*, 454(3):781–796.

Madej, O. K., Jonker, P. G., DÃŋaz Trigo, M., and MiÅąkoviÄĐovÃą, I. (2014). Variable doppler shifts of the thermal wind absorption lines in low-mass x-ray binaries. *Monthly Notices of the Royal Astronomical Society*, 438:145–155.

Malesani, D. B., Levan, A. J., Izzo, L., de Ugarte Postigo, A., Ghirlanda, G., Heintz, K. E., Kann, D. A., Lamb, G. P., Palmerio, J., Salafia, O. S., Salvaterra, R., Tanvir, N. R., Agüí Fernández, J. F., Campana, S., Chrimes, A. A., D'Avanzo, P., D'Elia, V., Della Valle, M., De Pasquale, M., Fynbo, J. P. U., Gaspari, N., Gompertz, B. P., Hartmann, D. H., Hjorth, J., Jakobsson, P., Palazzi, E., Pian, E., Pugliese, G., Ravasio, M. E., Rossi, A., Saccardi, A., Schady, P., Schneider, B., Sollerman, J., Starling, R. L. C., Thöne, C. C., van der Horst, A. J., Vergani, S. D., Watson, D., Wiersema, K., Xu, D., and Zafar, T. (2023). The brightest GRB ever detected: GRB 221009A as a highly luminous event at z = 0.151. *arXiv e-prints*, page arXiv:2302.07891.

Martin, P. G. (1970). On the interaction of cosmic X-rays with interstellar grains. *Monthly Notices of the Royal Astronomical Society*, 149:221.

Mason, K. O., Breeveld, A., Much, R., Carter, M., Cordova, F. A., Cropper, M. S., Fordham, J., Huckle, H., Ho, C., Kawakami, H., Kennea, J., Kennedy, T., Mittaz, J., Pandel, D., Priedhorsky, W. C., Sasseen, T., Shirey, R., Smith, P., and Vreux, J. M. (2001). The XMM-Newton optical/UV monitor telescope. *Astronomy & Astrophysics*, 365:L36–L44.

Mata Sánchez, D., Muñoz-Darias, T., Casares, J., and Jiménez-Ibarra, F. (2016). The donor of aquila x-1 revealed by high-angular resolution near-infrared spectroscopy. *Monthly Notices of the Royal Astronomical Society: Letters*, 464(1):L41–L45.

Mathis, J. S., Rumpl, W., and Nordsieck, K. H. (1977). The size distribution of interstellar grains. *The Astrophysical Journal*, 217:425–433.

Matsuba, E., Dotani, T., Mitsuda, K., Asai, K., Lewin, W. H. G., van Paradijs, J., and van der Klis, M. (1995). Discovery of x-ray bursts from gx 13+1 (4u 1811-17). *Publications of the Astronomical Society of Japan*, 47:575–580.

Mauche, C. W. and Gorenstein, P. (1986). Measurements of X-Ray Scattering from Interstellar Grains. *The Astrophysical Journal*, 302:371.

McClure-Griffiths, N. M., Pisano, D. J., Calabretta, M. R., Ford, H. A., Lockman, F. J., Staveley-Smith, L., Kalberla, P. M. W., Bailin, J., Dedes, L., Janowiecki, S., Gibson, B. K., Murphy, T., Nakanishi, H., and Newton-McGee, K. (2009). Gass: The Parkes Galactic All-Sky Survey. I. Survey Description, Goals, and Initial Data Release. *The Astrophysical Journal Supplement Series*, 181(2):398–412.

Mie, G. (1908). Beiträge zur optik trüber medien, speziell kolloidaler metallösungen. *Annalen der Physik*, 330(3):377–445.

Min, M., Waters, L. B. F. M., de Koter, A., Hovenier, J. W., Keller, L. P., and Markwick-Kemper, F. (2007). The shape and composition of interstellar silicate grains. *The Astrophysical Journal*, 462(2):667–676.

Miralda-Escudé, J. (1999). Small-Angle Scattering of X-Rays from Extragalactic Sources by Dust in Intervening Galaxies. *The Astrophysical Journal*, 512(1):21–24.

Murray, S. S., Austin, G. K., Chappell, J. H., Gomes, J. J., Kenter, A. T., Kraft, R. P., Meehan, G. R., Zombeck, M. V., Fraser, G. W., and Serio, S. (2000). In-flight performance of the Chandra high-resolution camera. In Truemper, J. E. and Aschenbach, B., editors, *X-Ray Optics, Instruments, and Missions III*, volume 4012 of *Society of Photo-Optical Instrumentation Engineers (SPIE) Conference Series*, pages 68–80.

Negro, M., Di Lalla, N., Omodei, N., Veres, P., Silvestri, S., Manfreda, A., Burns, E., Baldini, L., Costa, E., Ehlert, S. R., Kennea, J. A., Liodakis, I., Marshall, H. L., Mereghetti, S., Middei, R., Muleri, F., O'Dell, S. L., Roberts, O. J., Romani, R. W., Sgró, C., Terashima, M., Tiengo, A., Viscolo, D., Di Marco, A., La Monaca, F., Latronico, L., Matt, G., Perri, M., Puccetti, S., Poutanen, J., Ratheesh, A., Rogantini, D., Slane, P., Soffitta, P., Lindfors, E., Nilsson, K., Kasikov, A., Marscher, A. P., Tavecchio, F., Cibrario, N., Gunji, S., Malacaria, C., Paggi, A., Yang, Y.-J., Zane, S., Weisskopf, M. C., Agudo, I., Antonelli, L. A., Bachetti, M., Baumgartner, W. H., Bellazzini, R., Bianchi, S., Bongiorno, S. D., Bonino, R., Brez, A., Bucciantini, N., Capitanio, F., Castellano, S., Cavazzuti, E., Chen, C.-T., Ciprini, S., De Rosa, A., Del Monte, E., Di Gesu, L., Donnarumma, I., Doroshenko, V., DovcÌĘiak, M., Enoto, T., Evangelista, Y., Fabiani, S., Ferrazzoli, R., Garcia, J. A., Hayashida, K., Heyl, J., Iwakiri, W., Jorstad, S. G., Kaaret, P., Karas, V., Kislat, F., Kitaguchi, T., Kolodziejczak, J. J., Krawczynski, H., Maldera, S., Marin, F., Marinucci, A., Mitsuishi, I., Mizuno, T., Ng, C. Y.,

Oppedisano, C., Papitto, A., Pavlov, G. G., Peirson, A. L., Pesce-Rollins, M., Petrucci, P.-O., Pilia, M., Possenti, A., Ramsey, B. D., Rankin, J., Spandre, G., Swartz, D. A., Tamagawa, T., Taverna, R., Tawara, Y., Tennant, A. F., Thomas, N. E., Tombesi, F., Trois, A., Tsygankov, S. S., Turolla, R., Vink, J., Wu, K., and Xie, F. (2023). The IXPE View of GRB 221009A. *The Astrophysical Journal Letters*, 946(1):L21.

Newville, M. (2004). Fundamentals of xafs. *Consortium for Advanced Radiation Sources, University of Chicago (USA)[http://xafs. org]*, 78.

Oort, J. H., Kerr, F. J., and Westerhout, G. (1958). The galactic system as a spiral nebula (Council Note). *Monthly Notices of the Royal Astronomical Society*, 118:379.

Overbeck, J. W. (1965). Small-Angle Scattering of Celestial X-Rays by Interstellar Grains. *The Astrophysical Journal*, 141:864.

Peek, J. E. G., Heiles, C., Douglas, K. A., Lee, M.-Y., Grcevich, J., Stanimirović, S., Putman, M. E., Korpela, E. J., Gibson, S. J., Begum, A., Saul, D., Robishaw, T., and Krčo, M. (2011). The GALFA-HI Survey: Data Release 1. *The Astrophysical Journal Supplement Series*, 194(2):20.

Pinto, C., Kaastra, J. S., Costantini, E., and de Vries, C. (2013). Interstellar medium composition through x-ray spectroscopy of low-mass x-ray binaries. *Astronomy and Astrophysics*, 551:A25.

Pintore, F., Sanna, A., Di Salvo, T., Guainazzi, M., D'AÃň, A., Riggio, A., Burderi, L., Iaria, R., and Robba, N. R. (2014). Testing rate-dependent corrections on timing mode epic-pn spectra of the accreting neutron star gx 13+1. *Monthly Notices of the Royal Astronomical Society*, 445:3745–3754.

Pintore, F., Tiengo, A., Mereghetti, S., Vianello, G., Salvaterra, R., Esposito, P., Costantini, E., Giuliani, A., and Bosnjak, Z. (2017). Behind the dust curtain: the spectacular case of GRB 160623A. *Monthly Notices of the Royal Astronomical Society*, 472(2):1465–1472.

Planck Collaboration, Abergel, A., Ade, P. A. R., Aghanim, N., Alves, M. I. R., Aniano, G., Armitage-Caplan, C., Arnaud, M., Ashdown, M., Atrio-Barandela, F., Aumont, J., Baccigalupi, C., Banday, A. J., Barreiro, R. B., Bartlett, J. G., Battaner, E., Benabed, K., Benoît, A., Benoit-Lévy, A., Bernard, J.-P., Bersanelli, M., Bielewicz, P., Bobin, J., Bock, J. J., Bonaldi, A., Bond, J. R., Borrill, J., Bouchet, F. R., Boulanger, F., Bridges, M., Bucher, M., Burigana, C., Butler, R. C., Cardoso, J.-F., Catalano, A., Chamballu, A., Chary, R.-R., Chiang, H. C., Chiang, L.-Y, Christensen, P. R., Church, S., Clemens, M., Clements, D. L., Colombi, S., Colombo, L. P. L., Combet, C., Couchot, F., Coulais, A., Crill, B. P., Curto, A., Cuttaia, F., Danese, L., Davies, R. D., Davis, R. J., de Bernardis, P., de Rosa, A., de Zotti, G., Delabrouille, J., Delouis, J.-M., Désert, F.-X., Dickinson, C., Diego, J. M., Dole, H., Donzelli, S., Doré, O., Douspis, M., Draine, B. T., Dupac, X., Efstathiou, G., Enßlin, T. A., Eriksen, H. K., Falgarone, E., Finelli,

F., Forni, O., Frailis, M., Fraisse, A. A., Franceschi, E., Galeotta, S., Ganga, K., Ghosh, T., Giard, M., Giardino, G., Giraud-Héraud, Y., González-Nuevo, J., Górski, K. M., Gratton, S., Gregorio, A., Grenier, I. A., Gruppuso, A., Guillet, V., Hansen, F. K., Hanson, D., Harrison, D. L., Helou, G., Henrot-Versillé, S., Hernández-Monteagudo, C., Herranz, D., Hildebrandt, S. R., Hivon, E., Hobson, M., Holmes, W. A., Hornstrup, A., Hovest, W., Huffenberger, K. M., Jaffe, A. H., Jaffe, T. R., Jewell, J., Joncas, G., Jones, W. C., Juvela, M., KeihÃď nen, E., Keskitalo, R., Kisner, T. S., Knoche, J., Knox, L., Kunz, M., Kurki-Suonio, H., Lagache, G., Lähteenmäki, A., Lamarre, J.-M., Lasenby, A., Laureijs, R. J., Lawrence, C. R., Leonardi, R., León-Tavares, J., Lesgourgues, J., Levrier, F., Liguori, M., Lilje, P. B., Linden-Vørnle, M., López-Caniego, M., Lubin, P. M., Macías-Pérez, J. F., Maffei, B., Maino, D., Mandolesi, N., Maris, M., Marshall, D. J., Martin, P. G., Martínez-González, E., Masi, S., Massardi, M., Matarrese, S., Matthai, F., Mazzotta, P., McGehee, P., Melchiorri, A., Mendes, L., Mennella, A., Migliaccio, M., Mitra, S., Miville-Deschênes, M.-A., Moneti, A., Montier, L., Morgante, G., Mortlock, D., Munshi, D., Murphy, J. A., Naselsky, P., Nati, F., Natoli, P., Netterfield, C. B., Nørgaard-Nielsen, H. U., Noviello, F., Novikov, D., Novikov, I., Osborne, S., Oxborrow, C. A., Paci, F., Pagano, L., Pajot, F., Paladini, R., Paoletti, D., Pasian, F., Patanchon, G., Perdereau, O., Perotto, L., Perrotta, F., Piacentini, F., Piat, M., Pierpaoli, E., Pietrobon, D., Plaszczynski, S., Pointecouteau, E., Polenta, G., Ponthieu, N., Popa, L., Poutanen, T., Pratt, G. W., Prézeau, G., Prunet, S., Puget, J.-L., Rachen, J. P., Reach, W. T., Rebolo, R., Reinecke, M., Remazeilles, M., Renault, C., Ricciardi, S., Riller, T., Ristorcelli, I., Rocha, G., Rosset, C., Roudier, G., Rowan-Robinson, M., Rubiño-Martín, J. A., Rusholme, B., Sandri, M., Santos, D., Savini, G., Scott, D., Seiffert, M. D., Shellard, E. P. S., Spencer, L. D., Starck, J.-L., Stolyarov, V., Stompor, R., Sudiwala, R., Sunyaev, R., Sureau, F., Sutton, D., Suur-Uski, A.-S., Sygnet, J.-F., Tauber, J. A., Tavagnacco, D., Terenzi, L., Toffolatti, L., Tomasi, M., Tristram, M., Tucci, M., Tuovinen, J., TÃijrler, M., Umana, G., Valenziano, L., Valiviita, J., Van Tent, B., Verstraete, L., Vielva, P., Villa, F., Vittorio, N., Wade, L. A., Wandelt, B. D., Welikala, N., Ysard, N., Yvon, D., Zacchei, A., and Zonca, A. (2014). Planck 2013 results. xi. all-sky model of thermal dust emission. *Astronomy & Astrophysics*, 571:A11.

Reid, M. J., Menten, K. M., Brunthaler, A., Zheng, X. W., Dame, T. M., Xu, Y., Li, J., Sakai, N., Wu, Y., Immer, K., Zhang, B., Sanna, A., Moscadelli, L., Rygl, K. L. J., Bartkiewicz, A., Hu, B., Quiroga-Nuñez, L. H., and van Langevelde, H. J. (2019). Trigonometric Parallaxes of High-mass Star-forming Regions: Our View of the Milky Way. *The Astrophysical Journal*, 885(2):131.

Reynolds, C. S., Kara, E. A., Mushotzky, R. F., Ptak, A., Koss, M. J., Williams, B. J., Allen, S. W., Bauer, F. E., Bautz, M., Bogadhee, A., Burdge, K. B., Cappelluti, N., Cenko, B., Chartas, G., Chan, K.-W., Corrales, L., Daylan, T., Falcone, A. D., Foord, A., Grant, C. E., Habouzit, M., Haggard, D., Herrmann, S., Hodges-Kluck, E., Kargaltsev, O., King, G. W., Kounkel, M., Lopez, L. A., Marchesi, S., McDonald, M., Meyer, E., Miller, E. D., Nynka, M., Okajima, T., Pacucci, F., Russell, H. R., Safi-Harb, S., Strassun, K. G., Trindade Falcão, A., Walker, S. A.,

Wilms, J., Yukita, M., and Zhang, W. W. (2023). Overview of the advanced x-ray imaging satellite (AXIS). In Siegmund, O. H. and Hoadley, K., editors, *UV, X-Ray, and Gamma-Ray Space Instrumentation for Astronomy XXIII*, volume 12678 of *Society of Photo-Optical Instrumentation Engineers (SPIE) Conference Series*, page 126781E.

Rezaei, S. K., Beuther, H., Benjamin, R. A., Eilers, A.-C., Henning, T., Jiménez-Donaire, M. J., and Miville-Deschênes, M.-A. (2024). 3D structure of the Milky Way out to 10 kpc from the Sun: Catalogue of large molecular clouds in the Galactic Plane. *Astronomy & Astrophysics*, 692:A255.

Rogantini, D., Costantini, E., Zeegers, S. T., de Vries, C. P., Bras, W., de Groot, F., Mutschke, H., and Waters, L. B. F. M. (2018). Investigating the interstellar dust through the Fe K-edge. *A&A*, 609:A22.

Rogantini, D., Costantini, E., Zeegers, S. T., de Vries, C. P., Mehdipour, M., de Groot, F., Mutschke, H., Psaradaki, I., and Waters, L. B. F. M. (2019). Interstellar dust along the line of sight of GX 3+1. *Astronomy & Astrophysics*, 630:A143.

Rogantini, D., Costantini, E., Zeegers, S. T., Mehdipour, M., Psaradaki, I., Raassen, A. J. J., de Vries, C. P., and Waters, L. B. F. M. (2020). Magnesium and silicon in interstellar dust: X-ray overview. *Astronomy and Astrophysics*, 641:A149.

Rogantini, D., Homan, J., Plotkin, R. M., van den Berg, M., Miller-Jones, J., Neilsen, J., Chakrabarty, D., Fender, R. P., and Schulz, N. (2025). A persistent disk wind and variable jet outflow in the neutron-star low-mass x-ray binary gx 13+1. *The Astrophysical Journal*, 986:41.

Rolf, D. P. (1983). Evidence for the detection of X-ray scattering from interstellar dust grains. *Nature*, 302(5903):46–48.

Roman-Duval, J., Jackson, J. M., Heyer, M., Rathborne, J., and Simon, R. (2010). Physical Properties and Galactic Distribution of Molecular Clouds Identified in the Galactic Ring Survey. *The Astrophysical Journal*, 723(1):492–507.

Roming, P. W. A., Kennedy, T. E., Mason, K. O., Nousek, J. A., Ahr, L., Bingham, R. E., Broos, P. S., Carter, M. J., Hancock, B. K., Huckle, H. E., Hunsberger, S. D., Kawakami, H., Killough, R., Koch, T. S., McLelland, M. K., Smith, K., Smith, P. J., Soto, J. C., Boyd, P. T., Breeveld, A. A., Holland, S. T., Ivanushkina, M., Pryzby, M. S., Still, M. D., and Stock, J. (2005). The Swift Ultra-Violet/Optical Telescope. *Space Science Reviews*, 120(3-4):95–142.

Sakai, N., Nakanishi, H., Kurahara, K., Sakai, D., Hachisuka, K., Kim, J.-S., and Kameya, O. (2022). VERA astrometry toward the Perseus arm gap. *Publications of the Astronomical Society of Japan*, 74(1):209–223.

Sanna, A., Reid, M. J., Dame, T. M., Menten, K. M., and Brunthaler, A. (2017). Mapping spiral structure on the far side of the Milky Way. *Science*, 358(6360):227–230.

Sargent, B. A., Forrest, W. J., Tayrien, C., McClure, M. K., Li, A., Basu, A. R., Manoj, P., Watson, D. M., Bohac, C. J., Furlan, E., Kim, K. H., Green, J. D., and Sloan, G. C. (2009). Silica in Protoplanetary Disks. *ApJ*, 690:1193–1207.

Savage, B. D. and Sembach, K. R. (1996). Interstellar Abundances from Absorption-Line Observations with the Hubble Space Telescope. *Annual Review of Astronomy and Astrophysics*, 34:279–330.

Schlafly, E. F. and Finkbeiner, D. P. (2011). Measuring Reddening with Sloan Digital Sky Survey Stellar Spectra and Recalibrating SFD. *The Astrophysical Journal*, 737(2):103.

Schlafly, E. F., Finkbeiner, D. P., Schlegel, D. J., Jurić, M., Ivezić, Ž., Gibson, R. R., Knapp, G. R., and Weaver, B. A. (2010). The Blue Tip of the Stellar Locus: Measuring Reddening with the Sloan Digital Sky Survey. *The Astrophysical Journal*, 725(1):1175–1191.

Schlafly, E. F., Meisner, A. M., Stutz, A. M., Kainulainen, J., Peek, J. E. G., Tchernyshyov, K., Rix, H. W., Finkbeiner, D. P., Covey, K. R., Green, G. M., Bell, E. F., Burgett, W. S., Chambers, K. C., Draper, P. W., Flewelling, H., Hodapp, K. W., Kaiser, N., Magnier, E. A., Martin, N. F., Metcalfe, N., Wainscoat, R. J., and Waters, C. (2016). The Optical-infrared Extinction Curve and Its Variation in the Milky Way. *ApJ*, 821:78.

Schlegel, D. J., Finkbeiner, D. P., and Davis, M. (1998). Maps of Dust Infrared Emission for Use in Estimation of Reddening and Cosmic Microwave Background Radiation Foregrounds. *The Astrophysical Journal*, 500(2):525–553.

Schuller, F., Urquhart, J. S., Csengeri, T., Colombo, D., Duarte-Cabral, A., Mattern, M., Ginsburg, A., Pettitt, A. R., Wyrowski, F., Anderson, L., Azagra, F., Barnes, P., Beltran, M., Beuther, H., Billington, S., Bronfman, L., Cesaroni, R., Dobbs, C., Eden, D., Lee, M. Y., Medina, S. N. X., Menten, K. M., Moore, T., Montenegro-Montes, F. M., Ragan, S., Rigby, A., Riener, M., Russeil, D., Schisano, E., Sanchez-Monge, A., Traficante, A., Zavagno, A., Agurto, C., Bontemps, S., Finger, R., Giannetti, A., Gonzalez, E., Hernandez, A. K., Henning, T., Kainulainen, J., Kauffmann, J., Leurini, S., Lopez, S., Mac-Auliffe, F., Mazumdar, P., Molinari, S., Motte, F., Muller, E., Nguyen-Luong, Q., Parra, R., Perez-Beaupuits, J. P., Schilke, P., Schneider, N., Suri, S., Testi, L., Torstensson, K., Veena, V. S., Venegas, P., Wang, K., and Wienen, M. (2021). The SEDIGISM survey: First Data Release and overview of the Galactic structure. *Monthly Notices of the Royal Astronomical Society*, 500(3):3064–3082.

Shakura, N. I. and Sunyaev, R. A. (1973). Black holes in binary systems. observational appearance. *Astronomy and Astrophysics*, 24:337–355.

Shrestha, M., Sand, D. J., Alexander, K. D., Bostroem, K. A., Hosseinzadeh, G., Pearson, J., Aghakhanloo, M., Vinkó, J., Andrews, J. E., Jencson, J. E., Lundquist, M. J., Wyatt, S., Howell, D. A., McCully, C., Gonzalez, E. P., Pellegrino, C., Terreran, G., Hiramatsu, D., Newsome, M., Farah, J., Jha, S. W.,

Smith, N., Wheeler, J. C., Martínez-Vázquez, C., Carballo-Bello, J. A., Drlica-Wagner, A., James, D. J., Mutlu-Pakdil, B., Stringfellow, G. S., Sakowska, J. D., Noël, N. E. D., Bom, C. R., and Kuehn, K. (2023). Limit on Supernova Emission in the Brightest Gamma-Ray Burst, GRB 221009A. *The Astrophysical Journal Letters*, 946(1):L25.

Slavin, J. D., Dwek, E., Mac Low, M.-M., and Hill, A. S. (2020). The Dynamics, Destruction, and Survival of Supernova-formed Dust Grains. *The Astrophysical Journal*, 902(2):135.

Smith, R. K., Bautz, M., Bregman, J., Brenneman, L., Brickhouse, N., Bulbul, E., Burwitz, V., Bushman, J., Canizares, C., Chakrabarty, D., Cheimets, P., Costantini, E., DeRoo, C., Falcone, A., Foster, A., Gallo, L., Grant, C., Guenther, H. M., Heilmann, R. K., Heine, S., Hine, B., Huenemoerder, D., Jara, S., Kaastra, J., Kara, E., Kreykenbohm, I., Madsen, K., Marshall, H., McDonald, M., McEntaffer, R., Miller, J., Miller, E., Mushotzky, R., Nandra, K., Nowak, M., Paerels, F., Petre, R., Poppenhaeger, K., Ptak, A., Reid, P., Ronzano, K., Rozanska, A., Samra, J., Sanders, J., Schattenburg, M., Schonfeld, J., Schulz, N., Smale, A., Temi, P., Valencic, L., Walker, S., Wilms, J., and Wolk, S. (2022). Arcus: exploring the formation and evolution of clusters, galaxies, and stars. In den Herder, J.-W. A., Nikzad, S., and Nakazawa, K., editors, *Space Telescopes and Instrumentation 2022: Ultraviolet to Gamma Ray*, volume 12181 of *Society of Photo-Optical Instrumentation Engineers (SPIE) Conference Series*, page 1218121.

Smith, R. K. and Dwek, E. (1998). Soft x-ray scattering and halos from dust. *The Astrophysical Journal*, 503(2):831.

Sneppen, A. and Watson, D. (2025). The optical constants and grain sizes of interstellar dust measured directly using the dust-scattered X-ray halo of GRB221009A. *Astronomy and Astrophysics*, 701:A65.

Sofia, U. J. and Meyer, D. M. (2001). Interstellar Abundance Standards Revisited. *The Astrophysical Journal Letters*, 554(2):L221–L224.

Steenbrugge, K. C., Kaastra, J. S., de Vries, C. P., and Edelson, R. (2003). Xmm-newton high resolution spectroscopy of ngc 5548. *Astronomy and Astrophysics*, 402:477–486.

Strüder, L., Briel, U., Dennerl, K., Hartmann, R., Kendziorra, E., Meidinger, N., Pfeffermann, E., Reppin, C., Aschenbach, B., Bornemann, W., Bräuninger, H., Burkert, W., Elender, M., Freyberg, M., Haberl, F., Hartner, G., Heuschmann, F., Hippmann, H., Kastelic, E., Kemmer, S., Kettenring, G., Kink, W., Krause, N., Müller, S., Oppitz, A., Pietsch, W., Popp, M., Predehl, P., Read, A., Stephan, K. H., Stötter, D., Trümper, J., Holl, P., Kemmer, J., Soltau, H., Stötter, R., Weber, U., Weichert, U., von Zanthier, C., Carathanassis, D., Lutz, G., Richter, R. H., Solc, P., Böttcher, H., Kuster, M., Staubert, R., Abbey, A., Holland, A., Turner, M., Balasini, M., Bignami, G. F., La Palombara, N., Villa, G., Buttler, W., Gianini, F., Lainé, R., Lumb, D., and Dhez, P. (2001). The European Photon

Imaging Camera on XMM-Newton: The pn-CCD camera. *Astronomy & Astrophysics*, 365:L18–L26.

Sun, Y., Yang, J., Zhang, S., Yan, Q.-Z., Su, Y., Chen, X., Zhou, X., Xu, Y., Wang, H., Wang, M., Jiang, Z., Sun, J.-X., Lu, D.-R., Ju, B.-G., Zhang, X.-G., and Wang, M. (2024). A New View of the Spiral Structure of the Northern Outer Milky Way in Carbon Monoxide. *The Astrophysical Journal Letters*, 977(2):L35.

Tielens, A. G. G. M. (2001). The Composition of Circumstellar and Interstellar Dust. In Woodward, C. E., Bicay, M. D., and Shull, J. M., editors, *Tetons 4: Galactic Structure, Stars and the Interstellar Medium*, volume 231 of *Astronomical Society of the Pacific Conference Series*, page 92.

Tielens, A. G. G. M. (2008). Interstellar polycyclic aromatic hydrocarbon molecules. *Annual Review of Astronomy and Astrophysics*, 46:289–337.

Tiengo, A. and Mereghetti, S. (2006). Dust-scattered X-ray halos around gamma-ray bursts: GRB 031203 revisited and the new case of GRB 050713A. *Astronomy & Astrophysics*, 449(1):203–209.

Tiengo, A., Pintore, F., Vaia, B., Filippi, S., Sacchi, A., Esposito, P., Rigoselli, M., Mereghetti, S., Salvaterra, R., Šiljeg, B., Bracco, A., Bošnjak, Ž., Jelić, V., and Campana, S. (2023). The Power of the Rings: The GRB 221009A Soft X-Ray Emission from Its Dust-scattering Halo. *The Astrophysical Journal Letter*, 946(1):L30.

Tiengo, A., Vianello, G., Esposito, P., Mereghetti, S., Giuliani, A., Costantini, E., Israel, G. L., Stella, L., Turolla, R., Zane, S., Rea, N., Götz, D., Bernardini, F., Moretti, A., Romano, P., Ehle, M., and Gehrels, N. (2010). The Dust-scattering X-ray Rings of the Anomalous X-ray Pulsar 1E 1547.0-5408. *The Astrophysical Journal*, 710(1):227–235.

Tiengo, A., Vianello, G., Esposito, P., and Salvaterra, R. (2016). Swift detection of a dust-scattered halo around GRB 160623A. *GRB Coordinates Network*, 19559:1.

Titarchuk, L. (1994). Generalized comptonization models and application to the recent high-energy observations. *The Astrophysical Journal*, 434:570.

Truemper, J. (1982). The ROSAT mission. *Advances in Space Research*, 2(4):241–249.

Turner, M. J. L., Abbey, A., Arnaud, M., Balasini, M., Barbera, M., Belsole, E., Bennie, P. J., Bernard, J. P., Bignami, G. F., Boer, M., Briel, U., Butler, I., Cara, C., Chabaud, C., Cole, R., Collura, A., Conte, M., Cros, A., Denby, M., Dhez, P., Di Coco, G., Dowson, J., Ferrando, P., Ghizzardi, S., Gianotti, F., Goodall, C. V., Gretton, L., Griffiths, R. G., Hainaut, O., Hochedez, J. F., Holland, A. D., Jourdain, E., Kendziorra, E., Lagostina, A., Laine, R., La Palombara, N., Lortholary, M., Lumb, D., Marty, P., Molendi, S., Pigot, C., Poindron, E., Pounds, K. A., Reeves, J. N., Reppin, C., Rothenflug, R., Salvetat, P., Sauvageot, J. L., Schmitt, D., Sembay, S., Short, A. D. T., Spragg, J., Stephen, J., Strüder, L., Tiengo, A.,

Trifoglio, M., Trümper, J., Vercellone, S., Vigroux, L., Villa, G., Ward, M. J., Whitehead, S., and Zonca, E. (2001). The European Photon Imaging Camera on XMM-Newton: The MOS cameras. *Astronomy & Astrophysics*, 365:L27–L35.

Ueda, Y., Murakami, H., Yamaoka, K., Dotani, T., and Ebisawa, K. (2004). Chandra high-resolution spectroscopy of the absorption-line features in the low-mass x-ray binary gx 13+1. *The Astrophysical Journal*, 609:325.

Vaia, B., Bošnjak, Ž., Bracco, A., Campana, S., Esposito, P., Jelić, V., Sacchi, A., and Tiengo, A. (2025). Probing the interstellar medium toward GRB 221009A through X-ray dust scattering. *Astronomy & Astrophysics*, 696:A9.

Vallée, J. P. (2008). New Velocimetry and Revised Cartography of the Spiral Arms in the Milky Way—A Consistent Symbiosis. *The Astronomical Journal*, 135(4):1301–1310.

van de Hulst, H. C. (1946). The solid particles in interstellar space. *Recherches Astronomiques de l'Observatoire d'Utrecht*, 11:2.i–2.

Vasilopoulos, G., Karavola, D., Stathopoulos, S. I., and Petropoulou, M. (2023). Dust-scattering rings of GRB 221009A as seen by the Neil Gehrels Swift X-ray Observatory: can we count them all? *Monthly Notices of the Royal Astronomical Society*, 521(1):1590–1600.

Vaughan, S., Willingale, R., O'Brien, P. T., Osborne, J. P., Reeves, J. N., Levan, A. J., Watson, M. G., Tedds, J. A., Watson, D., Santos-Lleó, M., Rodríguez-Pascual, P. M., and Schartel, N. (2004). The Discovery of an Evolving Dust-scattered X-Ray Halo around GRB 031203. *The Astrophysical Journal Letters*, 603(1):L5–L8.

Veres, P., Burns, E., Bissaldi, E., Lesage, S., Roberts, O., and Fermi GBM Team (2022). GRB 221009A: Fermi GBM detection of an extraordinarily bright GRB. *GRB Coordinates Network*, 32636:1.

Vianello, G. and Longo, F. (2016). GRB 161202A: Fermi-LAT detection. *GRB Coordinates Network*, 20229:1.

Šiljeg, B., Bošnjak, Ž., Jelić, V., Tiengo, A., Pintore, F., and Bracco, A. (2023). Comparison of distance measurements to dust clouds using GRB X-ray haloes and 3D dust extinction. *Monthly Notices of the Royal Astronomical Society*, 526(2):2605–2619.

Vuong, M. H., Montmerle, T., Grosso, N., Feigelson, E. D., Verstraete, L., and Ozawa, H. (2003). Determination of the gas-to-dust ratio in nearby dense clouds using X-ray absorption measurements. *Astronomy & Astrophysics*, 408:581–599.

Watson, D. (2011). The Galactic dust-to-metals ratio and metallicity using gamma-ray bursts. *Astronomy & Astrophysics*, 533:A16.

Weingartner, J. C. and Draine, B. T. (2001). Dust Grain-Size Distributions and Extinction in the Milky Way, Large Magellanic Cloud, and Small Magellanic Cloud. *The Astrophysical Journal*, 548(1):296–309.

Weisskopf, M. C., Brinkman, B., Canizares, C., Garmire, G., Murray, S., and Van Speybroeck, L. P. (2002). An Overview of the Performance and Scientific Results from the Chandra X-Ray Observatory. *Publications of the Astronomical Society of the Pacific*, 114(791):1–24.

Weisskopf, M. C., Tananbaum, H. D., Van Speybroeck, L. P., and O'Dell, S. L. (2000). Chandra X-ray Observatory (CXO): overview. In Truemper, J. E. and Aschenbach, B., editors, *X-Ray Optics, Instruments, and Missions III*, volume 4012 of *Society of Photo-Optical Instrumentation Engineers (SPIE) Conference Series*, pages 2–16.

Westphal, A. J., Stroud, R. M., Bechtel, H. A., Brenker, F. E., Butterworth, A. L., Flynn, G. J., Frank, D. R., Gainsforth, Z., Hillier, J. K., Postberg, F., Simionovici, A. S., Sterken, V. J., Nittler, L. R., Allen, C., Anderson, D., Ansari, A., Bajt, S., Bastien, R. K., Bassim, N., Bridges, J., Brownlee, D. E., Burchell, M., Burghammer, M., Changela, H., Cloetens, P., Davis, A. M., Doll, R., Floss, C., Grün, E., Heck, P. R., Hoppe, P., Hudson, B., Huth, J., Kearsley, A., King, A. J., Lai, B., Leitner, J., Lemelle, L., Leonard, A., Leroux, H., Lettieri, R., Marchant, W., Ogliore, R., Ong, W. J., Price, M. C., Sandford, S. A., Tresseras, J.-A. S., Schmitz, S., Schoonjans, T., Schreiber, K., Silversmit, G., Solé, V. A., Srama, R., Stadermann, F., Stephan, T., Stodolna, J., Sutton, S., Trieloff, M., Tsou, P., Tyliszczak, T., Vekemans, B., Vincze, L., Von Korff, J., Wordsworth, N., Zevin, D., Zolensky, M. E., and aff14 (2014). Evidence for interstellar origin of seven dust particles collected by the Stardust spacecraft. *Science*, 345(6198):786–791.

Whittet, D. C. B. (2022). *Dust in the Galactic Environment (Third Edition)*. 2514-3433. IOP Publishing.

Williams, M. A., Kennea, J. A., Dichiara, S., Kobayashi, K., Iwakiri, W. B., Beardmore, A. P., Evans, P. A., Heinz, S., Lien, A., Oates, S. R., Negoro, H., Cenko, S. B., Buisson, D. J. K., Hartmann, D. H., Jaisawal, G. K., Kuin, N. P. M., Lesage, S., Page, K. L., Parsotan, T., Pasham, D. R., Sbarufatti, B., Siegel, M. H., Sugita, S., Younes, G., Ambrosi, E., Arzoumanian, Z., Bernardini, M. G., Campana, S., Capalbi, M., Caputo, R., D'Aí, A., D'Avanzo, P., D'Elia, V., Pasquale, M. D., Eyles-Ferris, R. A. J., Ferrara, E., Gendreau, K. C., Gropp, J. D., Kawai, N., Klingler, N., Laha, S., Melandri, A., Mihara, T., Moss, M., O'Brien, P., Osborne, J. P., Palmer, D. M., Perri, M., Serino, M., Sonbas, E., Stamatikos, M., Starling, R., Tagliaferri, G., Tohuvavohu, A., Zane, S., and Ziaeepour, H. (2023). Grb 221009a: Discovery of an exceptionally rare nearby and energetic gamma-ray burst. *The Astrophysical Journal Letters*, 946(1):L24.

Willingale, R., Starling, R. L. C., Beardmore, A. P., Tanvir, N. R., and O'Brien, P. T. (2013). Calibration of X-ray absorption in our Galaxy. *Monthly Notices of the Royal Astronomical Society*, 431(1):394–404.

Wilms, J., Allen, A., and McCray, R. (2000). On the Absorption of X-Rays in the Interstellar Medium. *The Astrophysical Journal*, 542(2):914–924.

Winkel, B., Kerp, J., Flöer, L., Kalberla, P. M. W., Ben Bekhti, N., Keller, R., and Lenz, D. (2016). The effelsberg-bonn hi survey: Milky way gasâŃĘ - first data release. *Astronomy & Astrophysics*, 585:A41.

XMM-Newton Science Operations Centre (SOC) (2025). *XMM-Newton Users Handbook*. ESA. Issue 2.23.

Yang, J., Schulz, N. S., Rogantini, D., Canizares, C. R., Corrales, L., and Psaradaki, I. (2022). The si k edge gas and dust optical depths toward the galactic bulge. *The Astronomical Journal*, 164:182.

Zeegers, S. T., Costantini, E., de Vries, C. P., Tielens, A. G. G. M., Chihara, H., de Groot, F., Mutschke, H., Waters, L. B. F. M., and Zeidler, S. (2017). Absorption and scattering by interstellar dust in the silicon k-edge of gx 5-1. *Astronomy and Astrophysics*, 599:A117.

Zeegers, S. T., Costantini, E., Rogantini, D., de Vries, C. P., Mutschke, H., Mohr, P., de Groot, F., and Tielens, A. G. G. M. (2019). Dust absorption and scattering in the silicon K-edge. *Astronomy & Astrophysics*, 627:A16.

Zhang, B., Reid, M. J., Menten, K. M., Zheng, X. W., Brunthaler, A., Dame, T. M., and Xu, Y. (2013). Parallaxes for W49N and G048.60+0.02: Distant Star Forming Regions in the Perseus Spiral Arm. *The Astrophysical Journal*, 775(1):79.

Zhang, X., Green, G. M., and Rix, H.-W. (2023). Parameters of 220 million stars from Gaia BP/RP spectra. *Monthly Notices of the Royal Astronomical Society*, 524(2):1855–1884.

Zhao, G. and Shen, R.-F. (2024). Expansion and Spectral Softening of the Dust-scattering Rings of GRB 221009A. *The Astrophysical Journal*, 970(2):124.

Zhu, H., Tian, W., Li, A., and Zhang, M. (2017). The gas-to-extinction ratio and the gas distribution in the Galaxy. *Monthly Notices of the Royal Astronomical Society*, 471(3):3494–3528.

Zubko, V., Dwek, E., and Arendt, R. G. (2004). Interstellar Dust Models Consistent with Extinction, Emission, and Abundance Constraints. *The Astrophysical Journal Supplement Series*, 152(2):211–249.